SYNTHESIS, CHARACTERIZATION AND PHOTORESPONSE PROPERTIES OF RUTHENIUM-BASED DYE SENSITIZERS FOR SOLAR CELLS: COMPUTATIONAL AND EXPERIMENTAL STUDIES

A MINI THESIS SUBMITTED IN PARTIAL FULFILMENT

OF THE REQUIREMENTS FOR THE DEGREE OF

MASTER OF SCIENCE (CHEMISTRY)

OF

THE UNIVERSITY OF NAMIBIA

BY

Paulina Tuulikefo Endjala

201137798

November 2019

Supervisor: Dr. V. Uahengo (Department of Chemistry and Biochemistry, University of Namibia)

Co-Supervisor: Prof. Edet F. Archibong (Department of Pharmaceutical Chemistry, University of Namibia)

ABSTRACT

Dye-Sensitized Solar Cells (DSSCs) are promising third-generation photovoltaic devices that offer the conversion of light energy into electricity at a lower cost. At the heart of this device is a sensitizer (dye) adsorbed on TiO_2-photoanode, which is responsible for the harvesting of visible light energy. However, the currently used sensitizers offer little improvement to the overall cell efficiency and this constitutes the main challenge to this technology. This work reports a combined experimental and computational study for the synthesis and characterization of the designed ruthenium-based dye complex (S2*) as a potential sensitizer for use in DSSCs. Initially, a series of ligands (S1, S2, S3 and S4) and their corresponding ruthenium-based dye complexes (S1*, S2*, S3* and S4*) were designed. Then, selection criteria based on the photoresponse properties, HOMO-LUMO energy gaps and redox properties of these dye complexes were considered to select the potential sensitizer.

The structures of the ligands and corresponding ruthenium complexes were fully optimized using B3LYP variant of the density functional theory (DFT) in conjunction with the 6-31G(d,p) basis set. The Stuttgart-Dresden (SDD) effective core potential was used to represent the inner orbitals of ruthenium (Ru). Subsequently, excitation energies were computed at the optimized geometries of the ligands and complexes using time-dependent DFT.

Aided by computed results, the potential dye (S2*) was synthesized and characterized using spectroscopic methods of Fourier Transform Infrared (FTIR), UV-Vis and fluorescence. Detailed theoretical study of S2* was performed using computational approaches such as DFT and TD-DFT at the B3LYP/6-31G(d,p) level. Full geometry optimization followed by frequency calculations suggested the structure of S2* as a genuine minimum characterized with Hessian index of zero (0). The optimized geometry of S2* was used to compute excitation energies as well as to investigate solvation effects using the Polarizable Continuum Model (PCM).

Both theoretical and experimental absorption spectra indicate that S2* displays a well-enhanced metal-to-ligand charge transfer band (MLCT) in the visible region. This character is defined by an absorption maximum of 452 nm experimentally, which is in good agreement with 483 nm obtained computationally. Solvatochromic studies of S2* shows that acetonitrile is the best choice of solvent in terms of photocatalytic enhancement and tetrahydrofuran is the best solvent in terms of bathochromic effect, with a broad low intense red-shifted band. S2* shows excellent photoresponse properties which makes it to be a potential candidate for DSSCs.

LIST OF CONFERENCE PROCEEDINGS

Conference:

1. 6th Annual Faculty of Science Research Conference (14th – 15th November 2018), University of Namibia, Namibia.

Workshops:

1. Royal Society-Department for International Development (RS-DFID) Africa Capacity Building Initiative (1st – 5th August 2017), University of Namibia, Namibia.
2. Workshop on thesis writing and publishing (28th – 31st July 2018), Kwame Nkrumah University of Science and Technology (KNUST), Kumasi, Ghana.
3. Summer School/Workshop on Computational Chemistry “Knowledge for Tomorrow – Cooperative Research Projects in Sub-Saharan Africa” (29 September 2019 - 12 October 2019), University of Mauritius, Mauritius.
4. 2020 African School of Catalysis (20 – 24 January 2020), ICTP-EAIFR, University of Rwanda, Kigali, Rwanda.

TABLE OF CONTENTS

LIST OF TABLES

LIST OF FIGURES

LIST OF SCHEMES

LIST OF ABBREVIATIONS AND/OR ACRONYMS

Nomenclatures

ΔH_{vib}	Vibrational enthalpy change
3-21G(d)	Pople split valence basis set with each core orbital represented with one function consisting of three primitives and each valence orbital represented with two functions consisting of three primitives and (d) polarization functions on non-hydrogen atoms.
6-31G(d,p)	Pople split valence basis set with each core orbital represented with one function consisting of six primitives and each valence orbital represented with two functions consisting of 4 primitives and (d) polarization functions on non-hydrogen atoms and (p) polarization functions on hydrogen atoms.
B3LYP	Becke 3 parameter exchange functional with correlation functional of Lee, Yang and Parr
B3PW91	Becke 3 parameter exchange functional with Perdew and Wang's 1991 gradient-corrected correlation functional
BLYP	Becke exchange functional with correlation functional of Lee, Yang, Parr
cc-pVXZ	Dunning correlation-consistent, polarized. valence, X-zeta basis; X=D,T,Q,5,6,7
$\boldsymbol{\varepsilon}$	Molar extinction coefficient
ε_0	Zero-point correction
f	Oscillator strength

h	Planck’s constant
Hay-Wadt VDZ	Hay-Wadt valence double zeta
J_{SC}	Short-circuit photocurrent density
k_B	Boltzmann constant
l	Path length
LanL2DZ	Los Alamos National Laboratory 2-double-zeta
MPW	Modified Perdew and Wang’s 1991 gradient-corrected correlation functional
T	Temperature
v_i	Vibrational mode
δ	Delta (Chemical Shift)
η	Overall conversion efficiency
λ, λ_{max}, $\Delta\lambda$	Wavelength, maximum wavelength, change in wavelength
π/ π^*	pi bonding/ pi antibonding

Abbreviations/Acronyms

$(NH_4)_2Ce(NO_3)_6$	Ammonium Cerium(IV) Nitrate
$[Ru(bpy)_2(NO_3)_2]$	Bis(bipyridine)dinitratoruthenium(II)
$[Ru(bpy)_2Cl_2].2H_2O$	Bis(bipyridine)dichlororuthenium(II) dihydrate
$[Ru(bpy)_2S2](ClO_4)_2$	Bis(bipyridine)2-(4-((di(pyridin-2-yl)methylene)amino)phenyl)-1H-benzo[de]isoquinoline-1,3(2H)-dioneruthenium(II) perchlorate
$[Ru(bpy)_3]^{2+}$	Tris(bipyridine)ruthenium(II) ion
^{1}H-NMR	Proton Nuclear Magnetic Resonance

A	Absorbance
acn	Acetonitrile
AgCl	Silver Chloride
$AgNO_3$	Silver Nitrate
AM	Air Mass
bpy	2,2'-bipyridyl
c	Concentration
C, N, O, H	Carbon, Nitrogen, Oxygen, Hydrogen
$C1^-$, Br^-, CN^-, SCN^-	Chloride, Bromide, Cyanide, Thiocyanate
Calc.	Calculated
CAN	Ceric Ammonium Nitrate
CB	Conduction Band
CC	Coupled cluster
$CDCl_3$	Deuterated chloroform
Ce	Cerium
CI	Configuration interaction
Corr.	Corrected
d, dd, m	Doublet, Doublet of Doublets, Multiplets
DFT	Density Functional Theory
DMF	Dimethylformamide
DMSO	Dimethyl sulfoxide
DSSCs	Dye Sensitized Solar Cells
ECP	Effective Core Potential
E_{H-L}	HOMO-LUMO Energy gap
eq	Equivalents

EtOH	Ethanol
FF	Fill Factor
FTIR	Fourier Transformer Infrared
H	HOMO
h	Hour
hex	n-Hexane
HOMO	Highest Occupied Molecular Orbital
I^-/I_3^-	Iodide/triiodide
ICT	Intraligand Charge Transfer or Intramolecular Charge Transfer
ILCT	Intraligand Charge Transfer
IPCE	Incident-Photon-To-Electron Conversion Efficiency
IR, NIR	Infrared, Near- Infrared
L	LUMO
LSDA	Local Spin Density Approximation
LUMO	Lowest Unoccupied Molecular Orbital
meoh	Methanol
MLCT	Metal-Ligand Charge Transfer
MO	Molecular Orbital
MW	Molecular Weight
$NaClO_4.H_2O$	Sodium perchlorate monohydrate
NUST	Namibia University of Science and Technology
PCM	Polarizable Continuum Model
P_{max}, P_{in}	Maximum Power, Power of Incident radiation
Pt, PtI_4	Platinum, Platinum Iodide

PV	Photovoltaic
r.t.p	Room Temperature and Pressure
Ru	Ruthenium
S_0, S_2	Singlet ground state, Singlet first excited state
SDD	Stuttgart-Dresden
SnO_2	Tin Dioxide
STO	Slater Type Orbitals
Sym., Asym.	Symmetric, Asymmetric
TBA	Tetrabutylammonium
TD-DFT	Time-Dependent Density Functional Theory
thf	Tetrahydrofuran
TiO_2	Titanium Dioxide
UV-Vis	Ultraviolet-Visible
vac	Vacuum
V_{OC}	Open-Circuit Voltage
ZnO	Zinc Oxide

Units and Mathematical Symbols

%	Percentage
<, >, ≤, ≥ , =	Less than, greater than, less than or equal, greater than or equal, equal
±	Plus-minus
°, **°C**	Degree, degree Celsius
Å	Angstrom
a.u.	Atomic Units

cm, cm^{-1}	Centimetre, per centimetre (wavenumber)
eV	Electron Volt
g	Grams
L, L^{-1}	Litre, Per Litre
M, M^{-1}	Molar, Per molar
MHz	Megahertz
mL	Millilitre
mol	Mole
nm	Nanometre
ppm	Parts per million

ACKNOWLEDGEMENTS

First, I would love to thank the Superior Almighty God for being the source of my strength, courage and determination throughout my research work and thesis write-up. Thank you for giving me wisdom so that I may have knowledge and understanding of everything I did.

With great pleasure, I would love to give millions of thanks to my research supervisor, Dr. V. Uahengo and co-supervisor, Prof. Edet. F. Archibong. Thank you for an interesting research topic and for the knowledge acquired from it. Thank you for your reliability, attentiveness and support throughout my research work. It is of greatest honour to have been working with you.

To the department of Chemistry and Biochemistry (UNAM), I am grateful for all the laboratory facilities and provision of a good working environment. I, therefore, extend my gratitude to NUST for the IR analysis and Cardiff University for the ^{1}H-NMR analysis.

Generous thanks go to the Supercomputing machine in South Africa for making my computational part a success. Additionally, I gratefully acknowledge NCRST and NSFAF for financial assistance.

To my family, especially my parents, I give you special thanks for your emotional and physical support throughout my study. Thank you for believing in me and for pushing me through.

I further extend my gratitude to my research team: Ms Elizeth Humba, Ms Loini Kalipi, Ms Patemasella Gawanas, Ms Ingrid Shikangala and Mr Rocha Kaffer. Thank you for being friends and an A-Team to work with. Additionally, I would like to thank Mr Johannes Naimhwaka for helping me with the code names of my dye structures. Special thanks also go to Mrs Theopolina Thomas, Ms Selma Kambunga and Mr Sackey Nghipundjwa. Your contribution to my thesis is sincerely and greatly appreciated.

I dedicate this thesis to my beloved parents (Tate Samuel Endjala and Meme Rauha Endjala) and all my siblings. Because of you, I made it through!

DECLARATIONS

I, Paulina Tuulikefo Endjala, hereby declare that this study is my own work and is a true reflection of my research, and that this work, or any part thereof has not been submitted for a degree at any other institution.

No part of this thesis may be reproduced, stored in any retrieval system, or transmitted in any form, or by means (e.g. electronic, mechanical, photocopying, recording or otherwise) without the prior permission of the author, or The University of Namibia in that behalf.

I, Paulina Tuulikefo Endjala, grant The University of Namibia the right to reproduce this thesis in whole or in part, in any manner or format, which The University of Namibia may deem fit.

Paulina Tuulikefo Endjala	……………………	………………
Name of Student	**Signature**	**Date**

CHAPTER ONE: INTRODUCTION

1.1 Background of the study

Fossil fuels are the main primary source of energy worldwide, with noticeable impacts on the environment and economic landscape. Recently, the ever-increasing global energy consumption and the depletion of fossil fuels have been a subject of intense debate, based on the concern that such depletion may compromise the living standard and the well-being of future generations. In fact, the rate at which the demand of electricity rises due to human consumption is as a result of daily applications at which 40% contributions comes from the use of motors, 19% lighting, 13% household appliances, 12% resistance heating, 8% electronics and the remaining 8% due to daily applications of vehicle (trains), electrochemical and miscellaneous [1]. Therefore, on the basis of these statistics, the demand for electrification will continue to rise as long as the population growth rate increases and this will remain a major challenge for this generation [1].

Accordingly, one of the greatest challenges of this era is to find an alternative energy source that is more efficient, and durable to gradually replace the readily accessible, but depleting fossil fuels. In addition, this alternative energy source should be favourable to the global market, environment and human health [2,3]. One approach towards solving the current energy problem lies in the development of energy sources such as solar energy that does not generate harmful by-products [4].

Solar energy is free, clean, renewable, and it has been accepted as a major alternative source in producing electricity over fossil fuels worldwide. Further, solar energy allows countries to become independent from fuel imports and it also contributes to the goal of ensuring an efficient and sustainable form of energy. However, under working conditions, the traditional and most commercialized crystalline silicon solar cells show limitations and disadvantages. In cloudy weathers, or under low-light intensities such as indoor applications, crystalline silicon solar cells show low power conversion output with a decreased cell efficiency [5–9]. Consequently, a new and innovative approach has been sought via the design and production of Dye-Sensitized Solar Cells (DSSCs) which are potential alternatives to preceding generations of solar devices.

Dye-sensitized solar cells are third-generation solar devices which are under extensive studies due to their attractive properties which include, the performance of cell device in diffuse light conditions, low-carbon emission, low manufacturing cost, easy fabrication and high tolerance to impurities [10,11]. Dye-Sensitized Solar Cells (DSSCs) are photovoltaic devices that make use of molecular systems as sensitizers. The latter (sensitizers) capture visible light energy which is converted into electrical energy in the cell. Up to date, the most efficient sensitizers reported in the literature for solar cells are ruthenium-based complexes [12]. The design, synthesis and accurate characterization of molecular dyes and the determination of properties such as excitation energies and solvatochromism are often achieved by complementing “wet” experimental work with computational studies [13].

1.2 Statement of the problem

At present, DSSCs have an efficiency of 10-12% which is significantly lower than the efficiency of 20-25%, associated with traditional polycrystalline silicon cells [12,14,15]. The rather low efficiency of DSSCs is partly attributed to low molar absorption coefficient of the molecular sensitizers currently in use. Hence, there is a need to design and synthesize molecular compounds with better absorption properties which enhance the efficiency for the conversion of light to electricity within the solar cells.

1.3 Objectives of the study

a) To design ligands and their corresponding ruthenium-based complexes (sensitizers) for use in DSSCs.

b) To compute the excitation energies of the potential dye sensitizers and study solvatochromic effects in solvents of different polarities using computational techniques.

c) Selected sensitizers (based on objectives a and b) are synthesized, characterized and their photoresponse properties investigated in the visible region.

d) To investigate solvatochromism and compare the experimental results with computational data.

1.4 Significance of the study

The molecular dye sensitizer that has been synthesized in this project exhibits good absorption in the visible region. Consequently, the dye sensitizer is a potential candidate for use in DSSCs and should increase their efficiency and hence find an application. In addition, the dye sensitizer is cheap and expected not to contribute to the pollution of the environment.

1.5 Limitation of the study

This research was limited to the design of dye sensitizers, their characterization, and investigation of their photoresponse properties in the visible region, as well as solvatochromic effects in solvents of different polarities. Due to the scope of this study, the adsorption of these dye sensitizers on TiO_2 and the construction of the solar cell device to test their efficiency have not been carried out.

1.6 Delimitation of the study

This study focused on the design and characterization of four ruthenium-based dye complexes. In addition, B3LYP/6-31G(d,p) theoretical model was used to optimize the structures and compute the properties of the ligands and molecular dye complexes. This 6-31G(d,p) one-particle basis set was selected in order to reduce computational time and costs.

CHAPTER TWO: LITERATURE REVIEW

2.1 Photovoltaic Cells

The sun is the original and most powerful source of energy received on earth. Energy from the sun is harnessed in the form of radiation and is used in various applications on earth, ranging from daily applications (as a drying agent) to industrial applications (generating electricity). The term “solar energy” refers to radiant energy from the sun and is mainly harvested by solar devices such as solar cells. These devices are commonly known in their physical states as solar panels and are often referred to as photovoltaic (PV) solar devices.

Photovoltaic solar devices are designed in such a way that when exposed to sunlight, they capture the visible light energy and convert it into useful energy such as electricity. The word photovoltaic is simply broken down into “photo” which means light and “voltaic” which refers to the production of electricity [16]. These devices gained popularity worldwide as an alternative source of energy that slowly replaces the currently used fossil fuels by harnessing sunlight as the readily available, cleaner and most renewable source of energy on earth.

PV solar devices were first established in 1839 by a physicist called Alexandre-Edmund Becquerel who observed that “electrical currents arose from certain light-induced chemical reactions” [17–20]. Later in the 1940s, there was a breakthrough with the solid-state device, paving way in the industry for the first commercialized generation of silicon solar cell at a record efficiency of 6% [17–21]. As a result, the field of PV solar devices gained special attention by many researchers. Since then, various technologies of PV have been established which are now categorized in three generations depending on their materials, production techniques, working principles, durability, reliability, efficiency and price variation of different era [17,18,21].

The first generation of PV devices consist mainly of the traditional and most commonly used crystalline silicon cells, generally the mono- and poly-crystalline silicon act as the active materials [17,18,20–24]. This is currently the foremost technology in the market due to its high efficiency of 25% [14,18,21]. However, this generation involves the use of high purity silicon single crystals that are relatively expensive and hence high production cost for these PV devices [20–23]. With these shortcomings, the second generation was introduced with the aim to reduce the production cost of PV solar devices. Although relatively cheaper to produce when compared to the first generation PV cells, their efficiency of 18.4% is very low to make it competitive in the market industry [18]. This generation is based on the thin films PV technology, typically the amorphous and crystalline thin-film silicon solar cells [17,18,20–24]. Despite all, the strive to develop efficient and low-cost PV devices continued and intensive studies have been carried out in this field. As a result, new PV technologies emerged and became a contemporary topic of interest, representing a promising future of low-cost and efficient third generations PV technologies. Most technologies in this generation are not yet commercialized and tend to include the following PV cells and their respective efficiency: perovskite cells (22%), dye-sensitized solar cells (12%), quantum dots (21%) and organic solar cells (11%) [14,18,21]. Below, Table 1 lists different types of PV solar technologies and their reported efficiencies.

Table 1. Different types of PV solar technologies and their reported efficiencies measured under the global AM1.5 spectra (1000 W/m2) at 25°C [14].

Solar Cell Type	**Efficiency, %**
Si (crystalline cell)	26.7 ± 0.5
Si (multicrystalline cell)	22.3 ± 0.4
CdTe (cell)	21.0 ± 0.4
Si (amorphous cell)	10.2 ± 0.3
Si (microcrystalline cell)	11.9 ± 0.3
Perovskite (cell)	20.9 ± 0.7
Dye sensitized (cell)	11.9 ± 0.4
Organic (cell)	11.2 ± 0.3

2.2 Efficiency Calculations of Photovoltaic Devices

Efficiency is a criterion commonly used in characterizing an individual cell performance, based on the operational functions of a complete PV device. The efficiency calculation of a solar cell device involves several parameters, including short-circuit photocurrent density (J_{SC}), open-circuit voltage (V_{OC}), maximum power (P_{max}), fill factor (FF), incident-photon-to-electron conversion efficiency (IPCE), and overall conversion efficiency (η) [4,7]. J_{SC} is a measure of photocurrent density generated by a cell during illumination with zero applied voltage [4,25]. The short-circuit photocurrent density depends linearly on the intensity of light [26]. In DSSCs, dyes with higher molar extinction coefficient, ε, strongly influence the J_{SC} [7,27]. Additionally, V_{OC} is the potential difference experienced by the circuit in the absence of current [4,25]. V_{OC} is strongly influenced by the charge recombination process and charge injection efficiency in a DSSCs. The former should be reduced in order to ensure that there is little or no charge recombination between the oxidized dye and the conduction band (CB) of titanium dioxide (TiO_2) as well as the electrolyte and the CB of TiO_2 [7]. The latter, however, should be elevated within the cell device to ensure efficient charge injection into the CB of TiO_2.

FF is a key parameter that defines the quality of the cell based on the ratio of the theoretical P_{max} to the product of J_{SC} and V_{OC} [27,28].

$FF = P_{max} / (J_{SC}V_{OC})$ …..................... (1)

Furthermore, IPCE is the efficiency measure of the incident light as a function of wavelength (λ) [25]. IPCE describes the spectral response of a solar cell in which the number of electron pairs collected at each incident solar photon to flow through the external circuit is defined [4,25]. Finally, the overall solar-to-electrical energy conversion efficiency, η, is a fundamental parameter of the solar cell that quantifies the overall cell performance based on the efficiency [4,28]. η is defined by a ratio of P_{max} to P_{in}, where P_{in} is the power of incident radiation upon the cell [4,28]. The equations that define the two parameters of a solar cell (IPCE and η) are given below [4]:

$IPCE(\lambda) = 124 \cdot J_{SC}(\lambda) / \lambda \cdot P_{in}(\lambda)$ ……………… (2)

$\eta = J_{SC}V_{OC}FF / P_{in}$ ……………… (3)

2.3 Dye-Sensitized Solar Cells

Motivated by the principles of photosynthesis in plants, dye-sensitized solar cells became a significant research topic of the third generation PV solar cells as an alternative energy conversion technology over the crystalline silicon cells. The fundamentals of a DSSC is based on a sensitizer (a dye) coated on titanium dioxide nanoparticles, which mimic the actions of chlorophyll in plants to harvest visible light energy. DSSCs are innovative technologies with noticeable advantages over the first and second-generation technology because they offer optimized features that allow the ease of fabrication of a PV cell with low-cost materials, colour, mechanical flexibility, transparency, and efficient electricity produced even in low light conditions [21,29].

Dye-sensitized solar cells technology was pioneered by Michael Grätzel [30] around 1990 in Switzerland. The first publication on DSSCs appeared in the year 1991, with a breakthrough efficiency of 7.1% [12,20,31,32]. Subsequently, hundreds of papers have been published with the primary aim of commercializing the DSSCs technology at a much cheaper price with greater efficiency (Figure 1) [32]. The efficiency of DSSCs currently stands at a record of 12% [14,20], a level which is rigid, thus challenging the competitiveness of the technology [12].

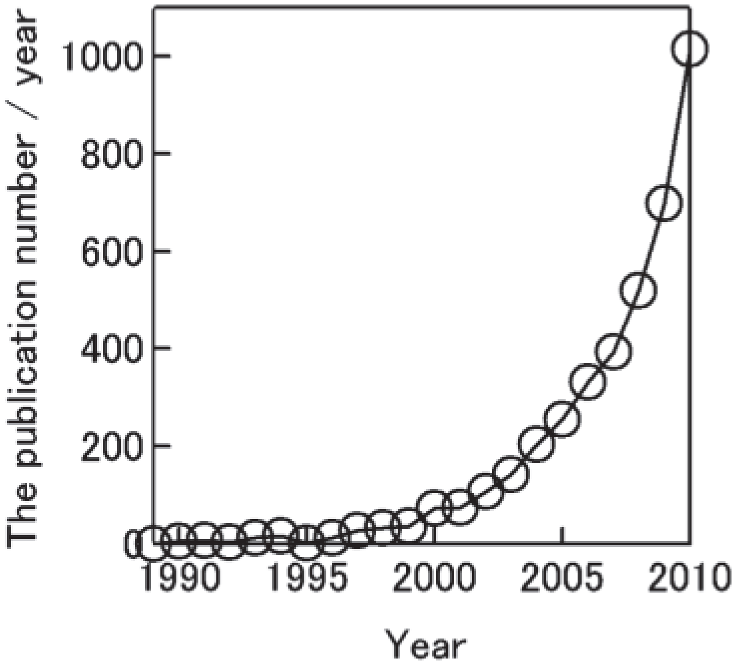

Figure 1. A number of publications on DSCs in each year from 1989 to 2010 [32].

2.3.1 Components of a Dye Sensitized Solar Cell

The performance of a DSSCs is attributed to four major components in the cell: a sensitizer, semiconductor, electrolyte and a counter electrode. The sensitizer is the heart of the cell, normally a molecular dye with a vital function of harvesting radiant energy. The semiconductor is generally an oxide nanoparticle serving as an adhesive of the dye and as a charge transfer path to the conduction band. Among the semiconductor investigated thus far are zinc oxide (ZnO), tin oxide (SnO_2), titanium dioxide (TiO_2) and chalcogenides [22,31]. The material of choice is anatase-TiO_2 [22] because of its larger surface area thereby enabling more light harvesting by the sensitizer. Another key component of a DSSCs is an electrolyte, which functions as a redox mediator by collecting electrons from the cathode towards the oxidized dye [31]. Typical electrolytes in DSSCs are the liquid-state electrolytes and solid-state electrolytes, with the most widely used electrolyte being the liquid-state iodide/triiodide (I^-/I_3^-) redox couple because of its cell efficiency [31]. The final cell component is the platinum counter electrode which collects electrons from the external circuit and injects them into the iodine redox couple electrolyte [22].

2.3.2 Working Principle of a DSSC

Based on the fundamentals of natural photosynthesis where energy from sunlight is used, Figure 2 illustrates the operating principles in artificial photosynthesis based on DSSC device. The initial step (step 1) is the photoexcitation of the dye. When illuminated, the adsorbed dye on the mesoporous TiO_2 semiconductor absorbs visible light energy thereby transiting to an excited state. The excited dye injects an electron into the conduction band (working electrode) through the mesoporous of TiO_2 nanoparticles (step 2). Consequently, the excited dye becomes oxidized and receives an electron from the electrolyte to regain its original state, leaving the electrolyte in an oxidized state (step 5). The transferred electrons in the conduction band electrode travel through the external circuit, performing some work and producing electricity (step 3). The electrons from the external circuit are collected at the counter electrode and then injected into the oxidized electrolyte marking the closing of the internal circuit (step 4).

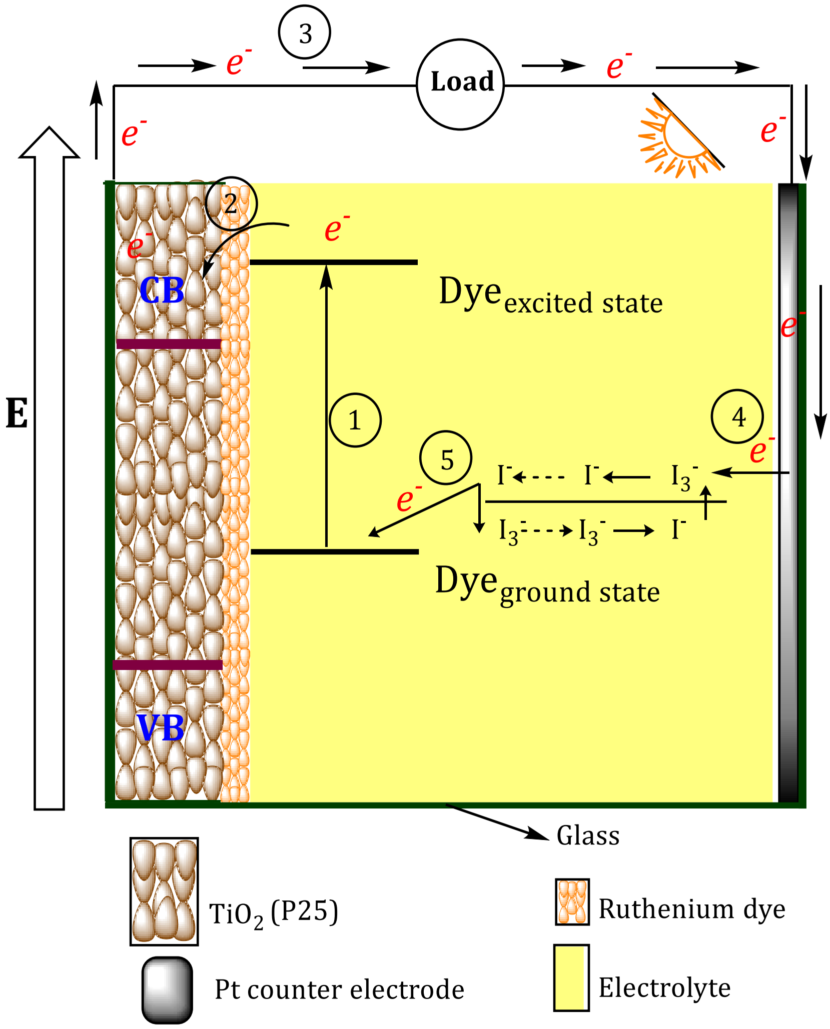

Figure 2. Working principles of a dye-sensitized solar cell.

2.3.3 Absorption spectra

The function of the dye is strongly dependent on the solar radiation spectrum. The first requirement in the process of converting radiant energy to electrical energy is the harvesting of a significant fraction of the solar spectrum [25]. According to the review of Walter et al. [25], approximately half the total energy of sunlight appears at wavelengths below 700 nm, a region typically covered well by solar absorbers (Figure 3). Preferably, an ideal dye should strongly absorb radiation over a wide range of wavelength in the visible region and extend its properties towards the near-infrared [4,25].

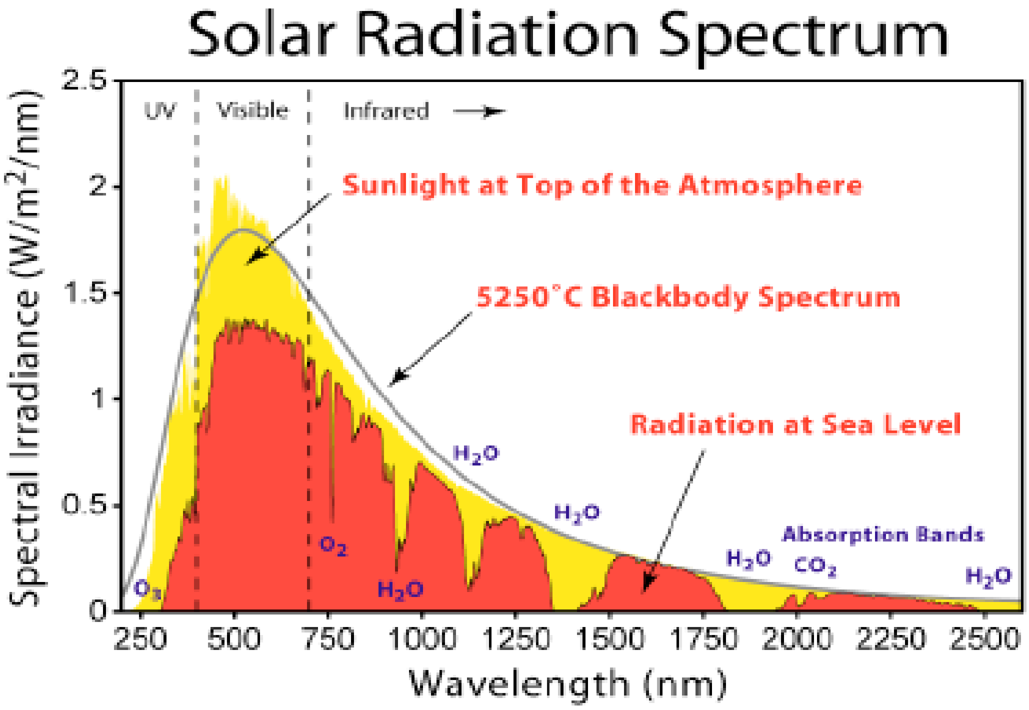

Figure 3. Solar radiation spectrum indicating irradiance at sea level (red fill), at the top of the atmosphere (yellow fill), and a blackbody spectrum (solid line) [4].

UV-Vis spectroscopy is a practical method used to study the electronic absorption spectra of the dye molecules [33]. Based on this approach, experimentalists are able to characterize the optical properties of the dye molecules by investigating their photoresponse behaviours (electronic transitions), solvent effects, adsorption properties on the surface of the TiO_2 layer and redox properties (for metal dyes). An ideal dye should, therefore, possess these properties by displaying a well-enhanced peak signal in the wavelength range of 400-750 nm (visible region).

Depending on the nature of the dye, the transition band occurring in the visible region is mostly attributed to intramolecular charge transfer (ICT) transition in metal-free dyes [34] and by a metal-ligand charge transfer (MLCT) transition by a mononuclear metal dye complexes [12]. For a dinuclear system (i.e. ruthenium dinuclear sensitizers) both MLCT and metal-metal charge transfer (MMCT) transition bands are observed in the visible region [35]. Veikko et al. [35] further discussed the oxidative properties of a ruthenium-based dye complex obtained by carrying out UV-Vis titration of a known concentration of the dye solution with a strong oxidizing agent, ceric ammonium nitrate ($(NH_4)_2Ce(NO_3)_6$). The spectra obtained was defined by an isosbestic point (an isosbestic point, in this case, represent ruthenium in the mixed-valence state, i.e. Ru^{2+}/Ru^{3+}) of the MLCT transition band in the visible region, showing the ground and excited states of ruthenium metal in the dye complex. Generally, the ground state of a ruthenium-based dye sensitizer has the metal in an oxidation state of +2 and the excited state has the metal in the +3 oxidation state [36,37].

Additionally, the UV-Vis spectra of an aryl-substituted β-diketonato-ruthenium(II)-polypyridyl sensitizer (complex 2) before and after its adsorption onto the surface of TiO_2 has been compared and reported [38]. Results obtained by comparisons showed that the maximum absorption wavelength for complex 2, when adsorbed on TiO_2, has been redshifted. Furthermore, in one reported study [39], a UV-Vis spectrum of a novel thiazole based azo dye, denoted as compound 4, prepared in different solvents of polarities has been presented. The study was done in order to investigate the effect of solvents on the structure of compound 4 and the observed results showed red-shifting of absorption bands towards longer wavelength in DMSO, DMF and all proton accepting solvents.

2.3.4 Challenges resulting from DSSCs components

The current efficiency of DSSCs recorded is of 10-12% [12,14] which is significantly lower than the commonly used polycrystalline silicon solar cells. With such efficiency, DSSCs appear inferior towards the traditional silicon cells, hence in low demand on the global market. The rather low efficiency is attributed to stability and nature at which each cell component operates, affecting the overall cell performance efficiency [3]. As a result, the current strategy is to optimize the efficiency of each component in order to have substantial or greater overall efficiency for the cell.

According to Ye et al. [3], among all publications based on the DSSC components, the photoanode which is the semiconductor outweighs all with a publication percentage of 40.78%. Another area of interest was the sensitizer with a percentage contribution of 24.53%. The remaining percentage of 34.69% was shared among other investigated components such as the electrolyte and the counter electrode [3].

An ideal photoanode should ensure a high loading of dye, thus a large surface area is required and should guarantee a fast charge transport rate [3]. The latter enables high electron collection efficiency [3] and the former enables high harvesting of sunlight by the sensitizer. The standard TiO_2 nanoparticle semiconductor has shortcomings that affect the overall cell efficiency. Besides its large surface area that enables a high dye loading capacity, the material tends to deteriorate the mobility of electrons thereby slowing down transportation and leading to recombination of photoexcited electrons [3]. To rectify these problems, potential applications of materials such as ZnO and SnO_2 have been considered as promising alternatives to TiO_2 [3,31]. Another potential candidate for the photoanode was found to be graphene, a carbon material that paved its way into the DSSCs device, due to its enhancement of the cell efficiency [3,23]. All these candidates exhibit unique characteristics in the performance operation of the

DSSCs. However, until recently, none of these regimes has outperformed the leading role of TiO_2 in the cell device [31].

The dye sensitizer is one of the leading factors that restrict the overall efficiency and affect the cost-effectiveness of the DSSC device. An ideal sensitizer should strongly absorb light in the visible region to near-infrared (NIR) regions [3,4]. This is one of the foremost issues that influence the overall performance of the cell. According to Grätzel [12], this challenge can be overcome by manipulating the dyes molecular structure either by increasing the degree of photons absorption in the functional wavelength range (as measured by the molar extinction coefficient, ε) or by extending the functional range to within the NIR region. So far, the most efficient dyes reported to date are ruthenium-based dye sensitizers with superior light-harvesting properties and durability [12]. Other alternatives to ruthenium dyes are the organic dyes which are the metal-free-loading dyes and natural dyes which are extracted from plants. Both organic and natural dyes show promising overall cell performance efficiency and a reduction in manufacturing cost relative to metal dye complexes. Additional benefits are offered via a simple extraction process of natural dyes from plants when compared to the more expensive synthetic procedures used in metal and organic dyes [23].

Finally, the stability of the DSSC is largely influenced by the currently used electrolyte and a counter electrode which are likely to undergo degradation under certain thermal conditions [21]. The liquid iodide/ triiodide redox electrolyte which is currently used is coupled in an organic solvent. This shows limitations in the performance enhancement of the DSSC device as the electrolyte freezes at low temperature and expands at higher temperatures causing serious damage to the cell [23]. This necessitated the search for a more effective solid electrolyte which, however, could not substitute the liquid electrolyte due to its low efficiency in the overall performance of the cell.

In addition, the standard platinum counter electrode reacts with the triiodide containing electrolyte to form a corrosive Pt in the form of PtI_4 [22]. The presence of platinum in the form of PtI_4 shows the danger in maintaining the overall performance of the cell efficiency [22]. Besides the degradation problems, platinum is an expensive metal. As a result, cheaper materials such as activated carbon and graphite are being investigated as inexpensive and alternative counter electrodes to the platinum electrode [22]. To date, all these alternatives provide “low overall cell performance efficiency”, and the carbon materials have not been able to adequately substitute platinum as the counter electrode.

Overall, while the current efficiency of the DSSCs is largely based on a cell composed of a ruthenium-based dye sensitizer, TiO_2 semiconductor, iodine/ triiodide redox couple electrolyte and a platinum counter electrode as standard cell components, improvement in one or two of these components could boost the cell efficiency and produce a cost-effective DSSC device.

2.3.5 Anchoring groups

A dye sensitizer must contain one or more functional groups to serve as an anchor to the titanium dioxide layer and form a charge transfer path for the electrons to travel from the excited dye to the conduction band of the TiO_2 semiconductor [7]. The adsorption of the anchoring groups is very important in cell performance, and their incorporation into a dye depends strongly on their physical and chemical behaviours at the interface of the semiconductor. A common anchoring group that has been employed in DSSC is a carboxylic acid group [7]. The latter readily reacts with TiO_2

to form an ester bond [8]. This group has been acknowledged for its stability and its strong binding ability on the surface of TiO_2, leading to fast electron injection to the conduction band of the semiconductor [35]. However, the carboxylate group barely detach itself from the surface of the semiconductor immediately after transferring an electron and as a result, back electron transfer occurs and the oxidized dye recombines with the electron [35]. The recombination of the oxidized dye and the electron hinders the efficiency of DSSC. Numerous studies have been conducted to find novel anchoring groups, among which are pyridine, phosphonic acid, tetracyanate, perylene dicarboxylic acid anhydride, 2-hydroxyl benzonitrile, 8-hydroxyquinoline, pyridine-N-oxide, hydroxylpyridium, catechol, hydroxamate, sulfonic acid, acetylacetonate, boronic acid, nitro, tetrazole, rhodanine, and salicylic acid substituents [7]. All these candidates are still under investigation and they are expected to yield high cell performance efficiency. Further, Veikko et al. [35] reported a dye-TiO_2 which was anchored through weak oxygen bridges of the ligand and hydrogen bonds from the titanol groups of TiO_2. The dye was efficient in transferring electrons to the conduction band without backward transfer of electrons as it detached itself from the surface of the semiconductor prior to the onset of recombination. The design of the anchoring groups in the current study was based on the work of Veikko et al [35].

2.3.6 Dye or Sensitizer

At the heart of the DSSC device is a sensitizer or dye. This is the most crucial part of the cell since it is responsible for the absorption of light, the latter being the initial step in the operation of DSSC. A dye or sensitizer can be defined as a molecular system that captures the visible light energy and converts it into electrical energy by means of other cell components. A sensitizer should possess the following characteristics [4,8]: strong absorbance of light in the visible range of the solar spectrum, high stability in the oxidized, ground and excited states, suitable redox potential, good efficiency in the charge injection and regeneration processes and must contain a functional group that will allow spontaneous assembly by chelating to TiO_2.

Dye sensitizers used in DSSCs are now classified as either inorganic, organic, or natural dyes. Further classification is based on whether the dyes are synthetic (inorganic- and organic-based dyes) or non-synthetic (natural dyes). The use of natural dyes as sensitizers has been considered promising for use in DSSCs because they are cheaper relative to synthetic dyes derived from metal-complexes [20].

On the other hand, metal-free organic dyes are promising candidates as sensitizers in DSSCs because they offer a high molar extinction coefficient which allows the use of thinner TiO_2 layer. Additionally, the absence of transition metals in their molecular structure reduces the cost of DSSCs [8,27,28]. The design of most organic dyes includes a donor–π spacer–acceptor (D–π–A) architecture [8,21,27,28].

In the DSSC community, ruthenium-based dyes are the most efficient dyes reported up to date [12]. These dyes are popular because they show greater stability in the presence of sunlight and have a considerable advantage that lies in the metal-ligand charge transfer (MLCT) transition, through which electrons are injected into the TiO_2. In 1991, Michael Grätzel reported high-performance Ru-based dyes namely N3, N719 and N749 (Black Dye) with efficiency between 10-11% (Figure 4). These dyes, also known as the "Grätzel Group", have been serving as benchmark dyes for DSSCs. Most ruthenium dyes belonging to the Grätzel group have the general structural formula of ML_2X_2, where L represents any bipyridyl-based ligand (i.e. 2,2-bipyridyl-4,4-dicarboxylic acid), M is ruthenium, and X is a halide, cyanide, thiocyanide or any bidentate ligand [40]. Using this general structural formula as an aid, the synthesis of several ruthenium-based dye complexes with extended π-conjugated molecular systems have been reported as follows.

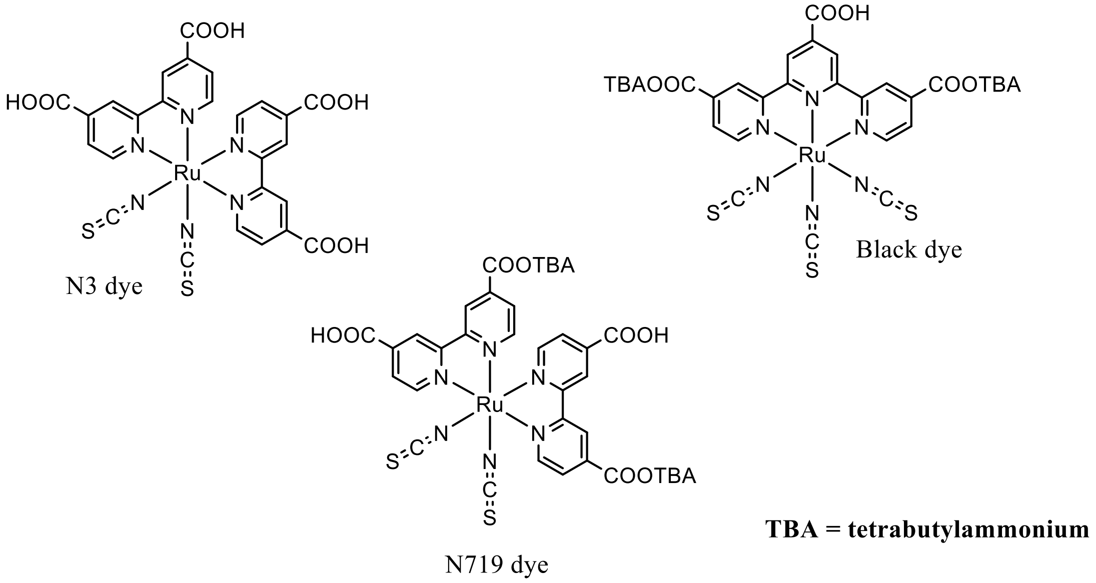

Figure 4. The ruthenium-based dye structures developed by the Grätzel group (serve as the benchmark for DSSC's) [12].

Nazeeruddin et al. [26] reported a series of cis-X_2Bis(2,2'-bipyridyl-4,4'-dicarboxylate)ruthenium(II) Charge-Transfer Sensitizers (X = C1-, Br-, I-, CN-, and SCN^-) on nanocrystalline TiO_2 photoanode. Among this series, cis-di(thiocyanato)bis(2,2'-bipyridyl-4,4'-dicarboxylate)ruthenium(II) showed outstanding performance with a solar-to-electric energy conversion efficiency of 10%. The dye is now known by the code name, "N3" (Figure 4).

Veikko et al. [35] reported the high performance of dinuclear ruthenium(II) dye sensitizer, ($[Ru_2(bpy)_4BL](ClO_4)_2$) derived from the N3 dye. The dye possessed good quantum efficiency as a result of high photon absorption and improved charge population. The study, also emphasized that the use of an oxygen group as an anchoring agent account for less electron recombination than the standard carboxylate anchors.

In 2008, McCall [41] investigated one of the novel ruthenium dye complexes based on the S-donor bidentate ligand, L1, with the aim of studying the effect of this strongly electron-donating system on the light-harvesting ability of the dye. The dye displayed good photoresponse properties with high molar extinction coefficient but however, it showed poor performance in a DSSC due to electron recombination induced by the presence of a cyano group on L1.

The presence of thiocyanate as a monodentate ligand in ruthenium complexes has been reported to cause instability in DSSCs [42]. Further, more effort has been made to introduce the design, synthesis and characterization of a series of thiocyanate-free cyclometalated ruthenium(II) sensitizers for DSSCs. The design of these dyes (labelled M1 to M4) was based on the N749 dye of the Grätzel group. Among the series, M3 showed the best overall efficiency of 7.1% due to increased electron-donating groups in the structure with a red-shifted MLCT absorption band in its spectrum.

A comparative study done by Liu et al. [43] between the N3 dye and a cross-linked dye sensitizer, denoted as Ru-C, was reported in 2009. The dye represents the first cross-linkable dye sensitizer to find applications in the literature of DSSCs. The relative studies between the two dyes revealed that although Ru-C achieved a power conversion efficiency of ±5.1% which is lower than that of N3 dye (10%, [26]), the Ru-C dye was stable and showed unchangeable power conversion efficiency for almost a month. On the other hand, N3 demonstrated a rapid decrease in efficiency within 2 weeks [43]. The results obtained for Ru-C showed its potential applications in DSSCs and has opened new doors to new sensitizers of the same design [44,45].

2.4 Computational details

Over the past years, various ab-initio quantum chemical methods have been employed in the study of DSSCs. Several of the studies combined experimental and theoretical approach in the design, synthesis, and characterization of potential dyes for use in DSSCs [34,42,46–50]. Computational studies have contributed immensely towards optimization of the structures and determination of photophysical properties of the dye molecules, including the adsorption of the latter to the surface of the photoanodes [13]. The most widely used computational approximation in the study of DSSCs is the ab-initio density functional theory (DFT) and its time-dependent extension (TD-DFT) [13,41,42,46–48,51–53].

2.4.1 Density functional theory study for DSSCs

Density functional theory (DFT) is an ab initio method that considers all the electrons in a system when used in modelling [54,55]. DFT partially takes account of electron correlation. When compared to sophisticated wavefunction based approximations such as configuration interaction (CI) and coupled cluster (CC), DFT provides accurate results at a lower computational cost [54,55] and as a result, it is highly recommended. In order to obtain a balance between accuracy and computational cost, the selection of a theoretical model is crucial in theoretical calculations [46]. In the case of DFT, several functionals are available for selection in the Gaussian software package. These functionals include LSDA, BLYP, B3LYP, B3PW91, etc. [46,54].

As noted in section 2.4, the DFT approach is commonly used in the study of DSSCs. The method provides good optimized molecular structures and reasonable estimate of excitation energies when compared to wavefunctions based ab initio methods such as the Hartree-Fock approximation [55]. Yamaguchi et al. [46] suggested DFT to be one of the most suitable and reliable theoretical methods to compute the properties of dye molecules used as sensitizers in DSSCs. The B3LYP variant of DFT is commonly used with basis sets ranging from smaller STO-3G and 3-21G(d) to larger basis sets such as cc-pVXZ [41,46,50,56,57]. Based on the accurate results obtained for a wide range of organic molecular compounds [54], B3LYP has been highly recommended for electronic structure calculations of dyes used in DSSCs.

Other than ground geometry optimization, vibrational frequency calculations are often carried out at the same level of theory used for optimization, in order to verify whether the structures are minima or transition states on their respective potential energy surfaces [41,58]. For metal dye-complexes such as ruthenium-based dye complexes, pseudopotentials such as the Stuttgart-Dresden (SDD) effective core potential (ECP) [48,58], the LanL2DZ ECP [59], and Hay-Wadt VDZ (n+1) ECP [41] are often used to represent the core electrons of the ruthenium metal. Pseudopotentials reduce computational cost (memory requirements and time) by allowing core electrons to be represented with one effective potential function while the outer orbitals are treated with one particle basis sets [60].

2.4.2 TD-DFT study for electronic absorption spectra

The computation of excitation energies using TD-DFT before the “wet” experimental work is done. This approach complements experimental work by predicting possible excitations and the regions where they occur. This information is invaluable in the interpretation of the experimental UV-Vis spectra [47].

In practice, excited state TD-DFT calculations generate the theoretical UV-Vis spectra of molecular dyes by providing information about the absorption band wavelength (λ_{max}), molar extinction coefficient, electronic transitions and oscillator strengths [46,61]. This is done by first carrying out geometry optimization using DFT and then

TD-DFT is performed on the optimized geometry of the structure to describe the excited states and optical properties of the molecular dye [60]. Generally, in order to gain a better insight into the electronic structure and its excited state properties, calculations are often carried out in both singlet and triplet excited states [49,62]. TD-DFT calculations are commonly performed in two ways: (i) in vacuum, where structures are computed in gas phase and (ii) in solutions where the structure interacts with solvents of different polarities. Both calculations are essential in DSSCs studies; excitation energies obtained from the solvent calculations are often compared to those obtained in vacuum to determine whether there is an interaction of the molecular dye with the solvent. Basically, if the dye molecule interacts with a specific solvent, shifts are often observed in energies towards either lower energy (bathochromic shift) or higher energy (hypsochromic shift).

Solvation inclusion in TD-DFT excited-state calculations is crucial in providing information which describes the transitions that make up the experimental absorption bands since the latter is often done in solutions [41]. In practice, solvation calculations are carried out using the polarizable continuum model (PCM) which account for solvent effects [41,46–49,51,63,64]. For metal complexes such as ruthenium dye complexes, solvation effects tend to reflect the most important features such as the MLCT bands in the absorption spectra [58]. A case study is the work of Nazeeruddin et al. [13] who reported a combined experimental and computational study of various ruthenium(II) sensitizers. The results obtained indicated good agreement between experiment and computed absorption spectra. Similarly, Barolo et al. reported experimental and computational investigation of a ruthenium complex coded as N886 and found that the theoretical spectra qualitatively reproduced the experimental absorption spectra [48].

CHAPTER THREE: RESEARCH METHODS

3.1 Research design

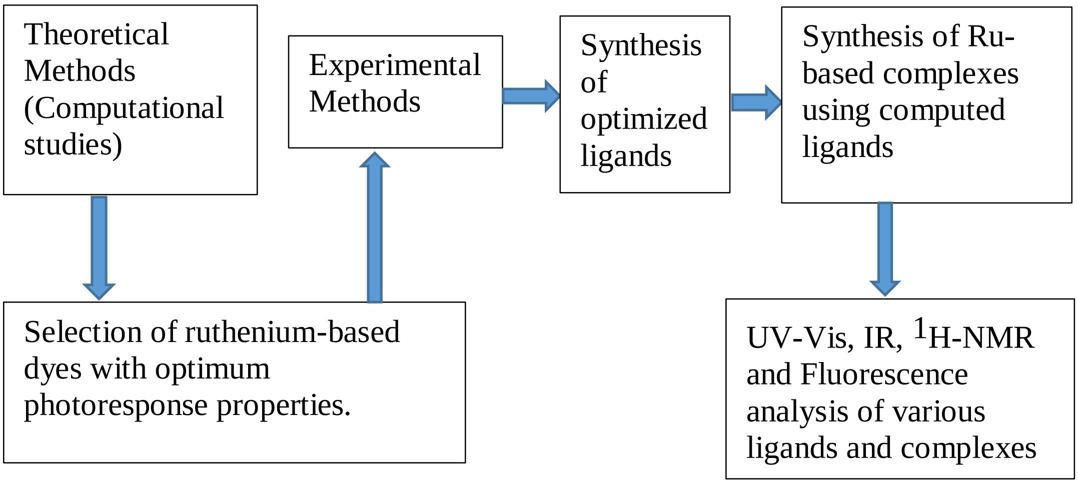

Figure 5. A flow diagram representing the project research design.

3.2 Research instruments

UV-Vis spectrophotometry and fluorescence were used to investigate the photoresponse properties of the dye. Fourier Transform Infrared (FTIR) spectrometry and proton nuclear magnetic resonance (^{1}H-NMR) spectroscopy were used to confirm the identity of the dye structure [65].

3.3 Procedure

3.3.1 Design of ligands and their ruthenium-based complexes as sensitizers for DSSCs

Molecules with highly π-conjugated moieties and carbonyl anchoring groups were designed as bidentate ligands for ruthenium N3-based complexes [12,13,35]. The designed ligands were S1, S2, S3 and S4 and their corresponding ruthenium-based dye complexes were S1*, S2*, S3* and S4* (Figure 6). The systematic names of these compounds are found in Table S1 of Appendix B.

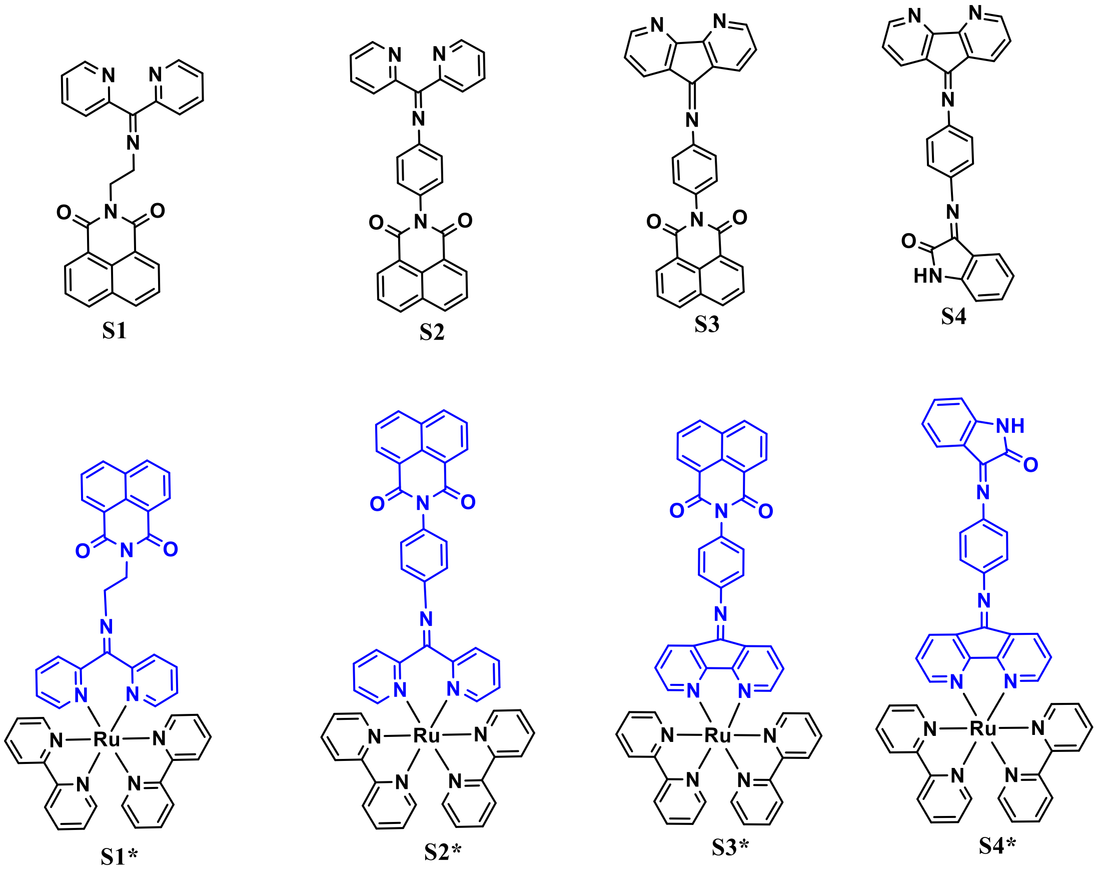

Figure 6. The designed ligands (S1-S4) and their ruthenium-based dye complexes (S1*-S4*).

3.3.2 Computation of excitation energies of the potential dyes and solvatochromic effects on the absorption spectra

Electronic structure calculations were performed using Gaussian 09 electronic structure programme [66]. All structures were fully optimized using B3LYP variant of the density functional theory (DFT) in conjunction with the 6-31G(d,p) basis set. The Stuttgart-Dresden (SDD) effective core potential was used to represent the inner orbitals of ruthenium (Ru). At the same level of theory, the structures were confirmed as minima or transition states via vibrational frequency calculations. Using the geometry of the optimized structures, time-dependent DFT (TD-DFT) calculations were carried out to obtain excitation energies of the dye complexes in the gas phase and in selected solvents using the polarizable continuum model (PCM) [13]. The solvatochromic study was done in solvents of different polarities [i.e. n-hexane (n-hex), tetrahydrofuran (thf), acetonitrile (acn) and methanol (meoh)] and the computed data was used to simulate the electronic absorption spectra [46,63].

The ground state geometry of S2 and its corresponding complex S2* was optimized in vacuum and in solvents of different polarities mentioned in the previous paragraph. Calculations were carried out at the B3LYP/6-31G(d,p) level and solvation effects were incorporated through the PCM method. Additionally, the excited states of S2 and S2* at the corresponding optimized geometries of vacuum, n-hexane, tetrahydrofuran, methanol and acetonitrile were studied by carrying out a single point energy calculation using TD-DFT-B3LYP/6-31G(d,p) as well as the PCM method for solvation effects. The TD calculations were strictly confined to 50 singlet states of allowed spin transitions for S2 and at least 70 singlet states of allowed spin transitions for S2*.

3.3.3 Synthesis of selected dye

The potential π-conjugated ligand was selected based on computational results. The ligand was synthesized according to procedures in the literature [67,68], and subsequently used as a bidentate ligand for the dye complex. The latter was also synthesized following the procedures outlined in the literature [35] and was found to be an N3-based ruthenium dye of the Grätzel group [12].

3.3.3.1 Synthesis of the anchoring group (A1)

1,8-naphthalic anhydride (2.9691 g, 0.015 mol) was dissolved in 60 mL of DMF and p-phenylenediamine (1.9511 g, 0.018 mol) was added to the above solution. The reaction was stirred at 80^{o}C and refluxed for 12 hours. The reaction mixture was poured into ice-cold water at the completion of the reaction and was filtered to yield a golden-cream product (4.2137 g, 0.0146 mol, 94.4%).

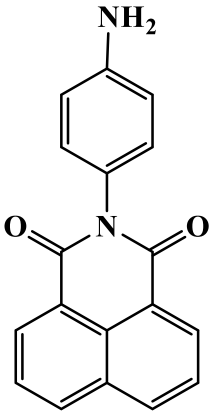

$C_{18}H_{12}N_2O_2$

MW = 288.3 g/mol

2-(4-aminophenyl)-1*H*-benzo[*de*]isoquinoline-1,3(2*H*)-dione

Figure 7. Synthesized anchoring group (A1).

3.3.3.2 Synthesis of bi-dentate ligand (S2)

Di (2-pyridyl) ketone (0.4111 g, 0.0022 mol) was dissolved in 40 mL of hot ethanol and A1 (0.5084 g, 0.0018 mol) was added to the solution followed by 5 drops of phosphoric acid. The mixture was stirred at room temperature overnight. The precipitate formed was filtered, washed successively with ethanol and dried in vacuum to give compound S2 (pale grey powder, 0.6174 g, 0.0014 mol, 75.5%). ^{1}H-NMR (400 MHz, $CDCl_3$) δ (ppm): 8.57 - 8.59 (dd, 4H, CH), 8.18 - 8.20 (dd, 4H, CH), 7.70 – 7.74 (dd, 4H, CH), 7.45 (d, 2H, CH), 7.0 (m 2H, CH), 6.74 - 6.77 (m, 2H, CH).

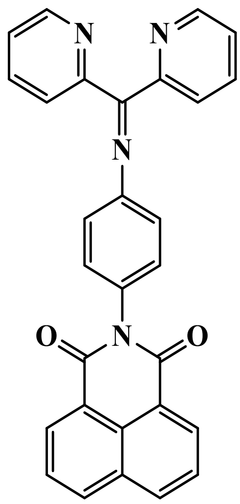

2-(4-((di(pyridin-2-yl)methylene)amino)phenyl)-1*H*-benzo[*de*]isoquinoline-1,3(2*H*)-dione

Figure 8. Synthesized binding ligand (S2).

3.3.3.3 Synthesis of ruthenium-based dye complex, S2*

$AgNO_3$ (0.3439 g, 0.0020 mol) was added to $[Ru(bpy)_2Cl_2].2H_2O$ (0.5161 g, 0.0010 mol) in absolute ethanol and the mixture was refluxed for 1hr at 98˚C. After cooling to room temperature, the solid residue (AgCl) was filtered out, washed with ethanol and discarded. To the filtrate, the ligand (S2) (0.1164 g, 0.0003 mol) was added and refluxed overnight in silicone oil while magnetically stirred. The solution was allowed to cool to room temperature and filtered to remove excess AgCl (solid discarded). Next, the filtrate was concentrated to 10 mL (evaporated to 90% dryness) by rotor-vapour. To the concentrated solution, a saturated ethanolic solution of $NaClO_4.H_2O$ (10 mL) was added and a precipitate formed. The mixture was left to settle at ambient temperature overnight. The reddish-brown precipitate was filtered off, washed with cold water and dried in vacuum to yield S2* ($[Ru(bpy)_2S2](ClO_4)_2$, 0.3578 g, 0.0003 mol, 33.5%).

S2* was recrystallized by dissolving it in 20 mL ethanol contained in 100 mL Erlenmeyer flask. The solution was heated to boiling in a water bath and filtered immediately while hot by using a crucible filter. The filtrate was allowed to cool at ambient temperature overnight in order to recrystallize. The pure dye was obtained as a residue through vacuum filtration using a crucible filter and washed with cold ethanol to yield (0.0418 g, 0.00004 mol, 13%, red S2*). ^{1}H-NMR (400 MHz, $CDCl_3$) δ (ppm): 8.65 - 8.69 (dd, 4H, CH), 8.27 - 8.30 (m, 4H, CH), 7.12 (m 2H, CH), 6.85 (m, 2H, CH).

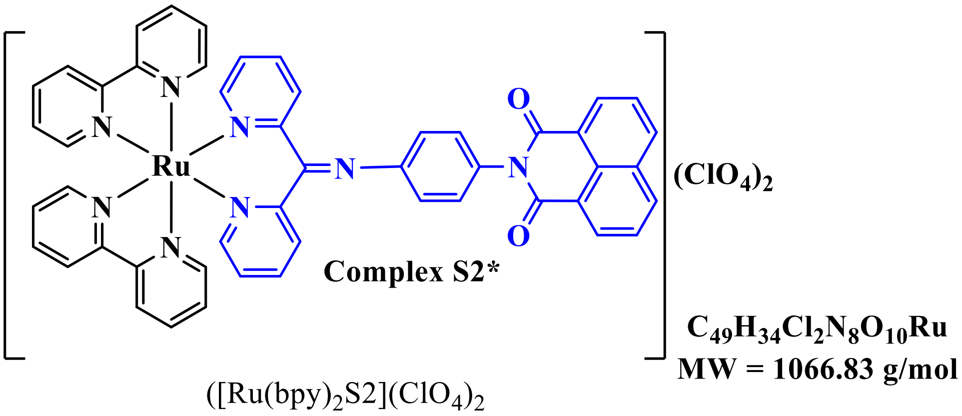

Figure 9. Synthesized dye complex (S2*).

3.3.4 Characterization of the ligands and their ruthenium-based dyes

3.3.4.1 UV-Vis spectrophotometry

A double beam PerkinElmer UV-Vis spectrophotometer Lambda 35 model was used to study the photocatalytic properties of the S2 ligand and its corresponding dye complex (S2*). The absorption spectra were recorded using a 1 cm quartz cuvette at room temperature, over a wavelength range of 200–800 nm unless otherwise stated. The UV-Vis absorption spectra of S2 and S2* were obtained by preparing a solution of both (1.0×10^{-5} M) in 100 mL acetonitrile, whereas the UV-Vis titration spectra of S2* was obtained by preparing a solution of the dye (1.0×10^{-5} M) in 100 mL acetonitrile and $(NH_4)_2Ce(NO_3)_6$ (3.0×10^{-2} M) in 100 mL acetonitrile. Background correction was done for all the spectra by taking the blank solvent absorbance for each measurement.

3.3.4.2 Fluorescence

Fluorescence spectroscopy was used to investigate the properties of the dye complex in terms of emissivity by using the SoftMax Pro 6.4 software. The emission spectrum of the complex was obtained by preparing a solution of the dye complex (1.0 x 10^{-5} M) in 100 mL acetonitrile at different excitation wavelengths ranging from 300 nm to 590 nm at an interval of 5 nm. The sample was analysed by transferring the dye solution into a fluorescence absorbance quartz cuvette (1 cm path-length) and by scanning through a fixed monochromatic beam of light at different excitations within the emission wavelength range of 400-800 nm. All spectra were recorded at room temperature and the blank fluorescence for the background correction was taken for each measurement beforehand.

3.3.4.3 Fourier Transform Infrared spectrometry

FTIR spectrometer was used to characterize and compare the peaks of different functional groups in the ligand before and after complexation. The IR analysis was done using the solid sample.

3.3.4.4 Proton nuclear magnetic resonance spectroscopy

S2 and the dye complex, S2*, were characterized using ^{1}H-NMR spectrometer installed with Bruker software package at Cardiff University. All samples were prepared in deuterated chloroform ($CDCl_3$) and the respective spectra were obtained at a frequency of 400 MHz.

3.3.5 Investigation of photoresponse properties of the ruthenium-based dye

The absorption maxima of the dye complex in the visible region were determined via UV-Vis analysis. The exact properties investigated were the excitations due to metal-to-ligand charge transfer (MLCT), a transition exhibited by most metal complexes in the visible region. The resultant spectrum was compared with computational data obtained from the TD-DFT calculations.

3.3.6 Effect of different solvents on the properties of the dye sensitizer

Since complexes have different absorption properties in different solvents, solvatochromic studies were done using UV-Vis spectrophotometer to determine the best solvent in terms of photoresponse properties enhancement or in terms of bathochromic shift effect. The UV-Vis absorption spectra of the dye complex were obtained by preparing a solution of the dye (1.0 x 10^{-5} M) in 100 mL of n-hexane (n-hex), tetrahydrofuran (thf), acetonitrile (acn) and methanol (meoh). The experimental study was complemented by computational data.

3.4 Data analysis

The total vibrational degree of freedom for each dye molecule is given by 3N-6 where N is the number of atoms in the molecule. For the minima structures, the Hessian index was 0 while the saddle points gave a Hessian index of 1. The zero point correction, ε_0, to the energies was obtained by summing the energy contributed by each vibrational mode (v_i), that is $\varepsilon_0 = \frac{1}{2} h \sum_i^{normal\ modes} v_i$, where h is the Planck's constant. The vibrational enthalpy change (ΔH_{vib}) was obtained from the Gaussian output using: $\Delta H_{vib}(T) = Nh \sum_i^{normal\ modes} \frac{v_i}{e^{\frac{hv_i}{k_B T}}-1}$, where T is the temperature in Kelvins and k_B is the Boltzmann constant.

The Beer Lambert's Law [8,28,69], $A(\lambda) = \varepsilon(\lambda) \cdot c \cdot l$ was used to describe the absorption of the ligand and its corresponding ruthenium-based dye complex. $A(\lambda)$ is the intensity of light at a specified wavelength, λ (nm), $\varepsilon(\lambda)$ is the molar extinction coefficient (mol^{-1} L cm^{-1}) of the dye and it depends on both the nature of the dye and the wavelength, c (mol L^{-1}) is the concentration of the absorbing molecular dye species and l (cm) is the path length of light through the absorbing species (this depends on the width of the sample holder, usually the cuvette being used for analysis). For a better comparison between experimental UV-Vis spectra and computational UV-Vis spectra, peak normalization was carried out by selecting the peak with the maximum intensity and dividing all other peaks in the spectrum with the maximum intensity. This gave normalized spectra with peak intensities ranging from 0 to 1.

CHAPTER FOUR: RESULTS AND DISCUSSION

4.1 Electronic structures of the designed sensitizers

The primary focus of this section is on S2* as the selected dye molecular sensitizer, based on its good optical and redox properties which are discussed in details from sections 4.3 to 4.4. Moreover, a brief discussion of other designed structures (S1*, S3* and S4*) will be highlighted as part of this study. The B3LYP/6-31G(d,p) optimized ground state geometries of the designed ligands and their ruthenium-based dye complexes in vacuum are shown in Table 2. The coordination chemistry of the ruthenium dye complexes is defined by an octahedral geometry [70]. As shown in Table 2, the central metal ion [ruthenium (II) ion] is coordinated to six nitrogen (N) atoms where four of the N atoms are from 2,2'-bipyridyl (bpy) ligands and the remaining two N atoms are from S1, S2, S3 and S4 ligands of each respective S1*, S2*, S3* and S4* dye complex.

The frontier molecular orbitals of S1*-S4* obtained from the molecular orbital analysis, and their calculated HOMO-LUMO (H-L) energy gaps are shown in Figure 10. For all the complexes, the HOMOs are located at the anchoring moieties containing the C=O keto group, and the LUMO are localized on the ruthenium metal with a large contribution from one of the bipyridyl (bpy) ligands for S1*, two bpy ligands for S2*, while for S3* and S4*, all the bpy ligands are contributing to the LUMO with little contribution from the 4,5-diazafluoren-9-one binding moiety of the designed ligands.

Table 2. Optimized ground state geometries of the designed ligands (S1-S4) and their corresponding ruthenium-based dye complexes (S1*-S4*).

Ligand	Dye Complex
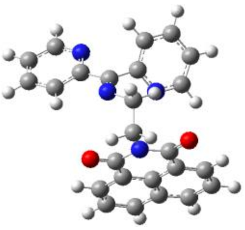 S1	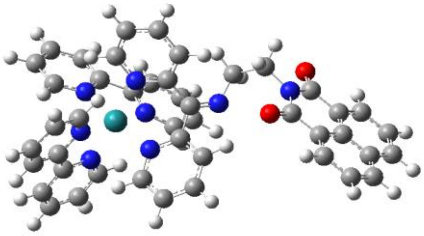 S1*
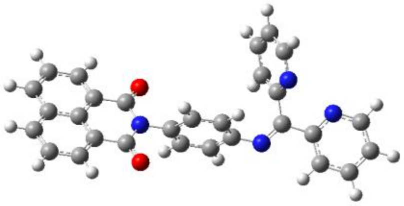 S2	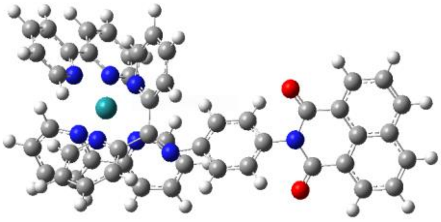 S2*
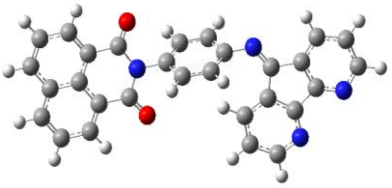 S3	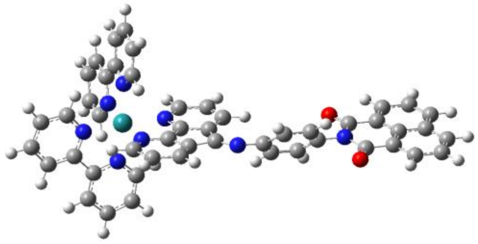 S3*
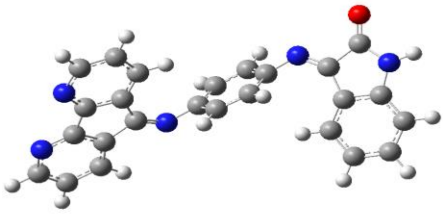 S4	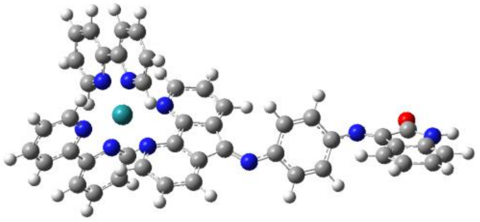 S4*

The general trend in the (H-L) gap of these complexes is in the decreasing order of S1*>S2*>S4*>S3*. The H-L gap is the energy difference between the highest occupied molecular orbital (HOMO) and the lowest unoccupied molecular orbital (LUMO) of the respective dye structures. Molecular structures with a smaller H-L energy gap are less kinetically stable and more chemically reactive whereas molecules that possess a larger H-L energy gap are more kinetically stable and less chemically reactive [71–73]. From this approach, it can be depicted that among all the dye molecules (S1*-S4*), S3* is more chemically reactive and less kinetically stable because of its small H-L energy gap (1.96 eV) relative to other dyes. On the other hand, S1* which exhibit the largest H-L energy gap (2.42 eV) is less chemically reactive but more kinetically stable than S2*, S3* and S4*. These statements can further be justified on the basis of the dye structures; whereby S3* and S4* are more conjugated than S2* and S1* (see Figure 6) hence, possesses a small H-L gap. As a result, increasing conjugation in these molecular dyes results in a decreasing trend in H-L gaps. Thus, the higher the degree of conjugation, the lower the H-L gap and vice-versa [74].

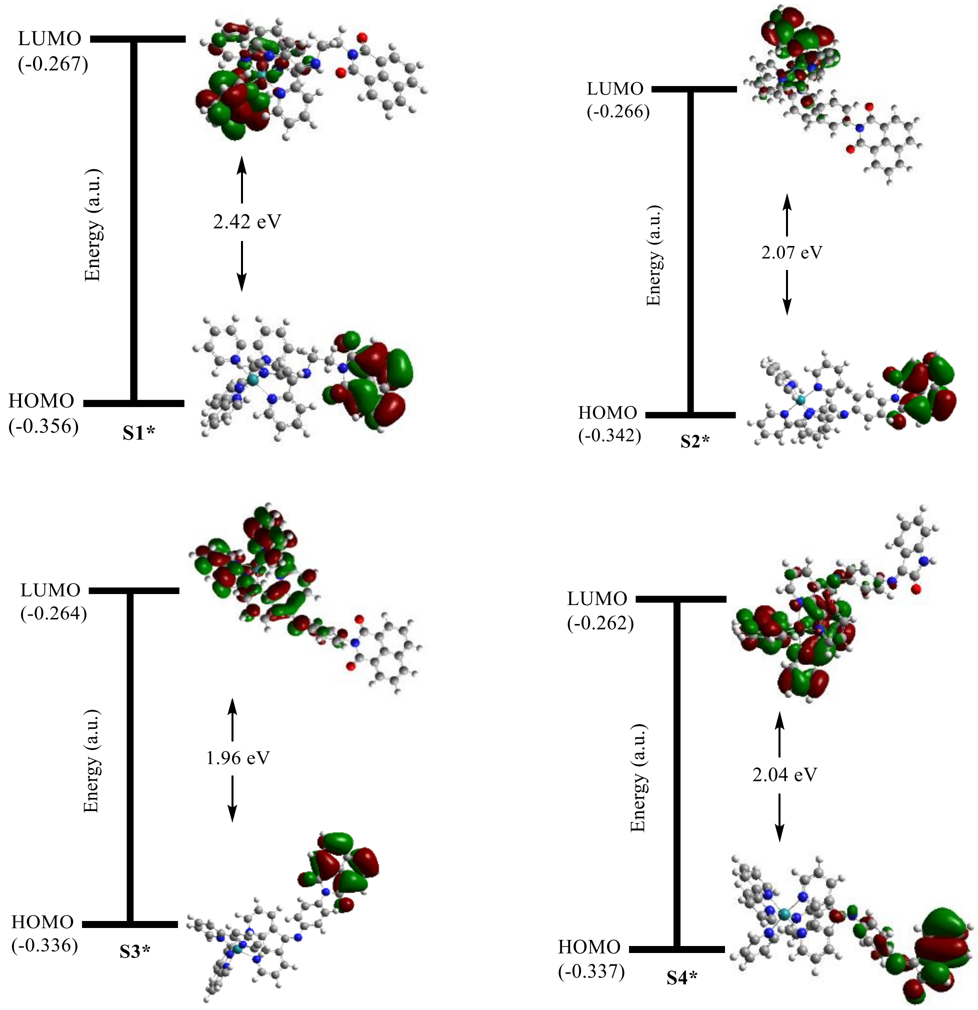

Figure 10. Plotted frontier molecular orbitals of the designed ruthenium-based dye sensitizers and their corresponding calculated energy gaps (eV) of their optimized geometry.

4.2 Criteria for selecting the potential dye: Simulated UV-Vis spectra

In order to select the potential molecular dye sensitizer, the designed molecular dyes (ligands and dye complexes) were characterized theoretically by computing their excitation energies with the primary objective of studying their optical properties. Initially, the optimized geometries of both the ligands and their corresponding dye complexes in vacuum were used to do Time-Dependent single point energy calculations in vacuum, n-hexane, tetrahydrofuran, acetonitrile and methanol. The simulated UV-Vis spectra obtained for the ligands (Figure S1 of Appendix B) and their respective dye complexes in acetonitrile (Figure 11) show a detailed analysis of how each of these designed sensitizers varies photo-responsively.

The spectra were obtained by computing 5 triplet and 5 singlet excited states using TD-DFT B3LYP/6-31G (d,p) model. For comparison purposes, acetonitrile was selected as the reference solvent for all the theoretical and experimental spectroscopic studies. In this regard, simulated UV-Vis spectra obtained for both the ligands and complexes in acetonitrile were used to select the complex with optimal photoresponse properties in the visible region. Accordingly, considerable measures were taken in terms of photocatalytic enhancement or by extension of the functional range towards the near-infrared region of the UV-Vis spectrum [35].

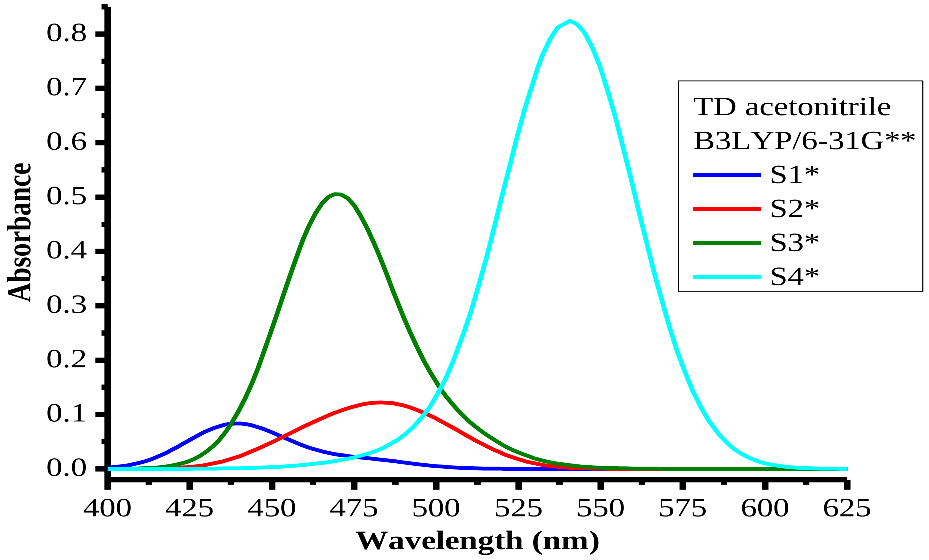

Figure 11. Simulated UV-Vis spectra of the designed dye complexes in acetonitrile.

Shown in Figure 11 is the UV-Vis absorption spectra of the dye complexes (S1* - S4*) in acetonitrile with characterized broad absorption bands in the visible range (λ > 400 nm) due to the metal-to-ligand charge transfer (MLCT) transition band. The MLCT band with the highest absorption maximum belongs to S4* and the band occurs at the longest wavelength (appears to be more red-shifted). On the other hand, the band due to S1* occurs at the shortest wavelength with the lowest intensity. This trend is observed for all spectra recorded in different solvents (Figure S2 of Appendix B). The results show that the spectrum of S4* is the most intense while that of S1* is the least intense, except in vacuum where S3* exhibits the highest absorbance. On the basis of the UV-Vis spectra of the dye complexes, the trend in photoresponse properties, from the highest excitation energies to the lowest excitation energies is S1* > S3* > S2* > S4*. However, while this trend is also observed in methanol, a different trend of S1* > S2* > S3* > S4*is found in tetrahydrofuran, n-hexane and vacuum. The spectra for the preceding trend can be found in Figure S2.

Strict analysis of the simulated UV-Vis spectra indicates that S4* can be selected as the potential dye sensitizer in terms of both photocatalytic enhancement (absorption maximum) and extension of its functional range to the NIR region. The latter observation could be attributed to the extended conjugation in S4* and possibly because the structure contains an isatin moiety which is absent in other dye complexes. Conversely, further experimental analysis on S4* showed that the dye molecule could not display proper redox properties (for example, it does not exhibit distinct isosbetic point) in the UV-Vis titration spectra upon its titration with $(NH_4)_2Ce(NO_3)_6$ which is an oxidative reagent. The UV-Vis titration spectra of S4* is displayed in Figure S8 of Appendix B. The redox property is a very important factor in selecting a potential metal dye complex for DSSC application because the metal centre in the dye complex is expected to exist in mixed-valence states upon photoexcitation of the dye through the MLCT [35,75].

Based on the above consideration, S2* was preferred over S4* and it was selected in this study as the potential dye sensitizer with optimal photoresponse and redox properties compared to S3* and S1*. Detail redox properties of S2* are discussed under the experimental section.

4.3 Theoretical studies of S2*

The simulated IR spectrum of S2 and its metal complex is presented in Figure 12. Assignment of the vibrational modes and their respective frequencies are presented in Table 3. The simulated IR spectra of S2 and S2* have the same features (i.e. most of the vibrational modes present in S2 are observed in S2* except that the intensity and band positions vary slightly and few are merged as one spectral band) and no distinct additional of vibrational band(s) is observed in S2* except for the peak at 1188 cm^{-1}. The latter is due to the fact that both starting materials [S2 and $Ru(bpy)_3^{2+}$] contain pyridine rings coordinated to the central ruthenium (II) ion.

In Figure 12 it can also be noticed that the very weak intense vibrational band at around 1698 cm^{-1} present in the IR spectrum of S2 is not observed in the spectrum of S2*. Noted, however, through simulations with Gaussview, that this vibrational energy peak was observed at 1675 cm^{-1} in S2* with a negligible intensity. Consequently, through simulation of S2 and S2*, this vibrational band has been assigned to the imine (C═N) vibrational stretching. The data in Table 3 shows the presence of metal-to-ligand (Ru-N) vibrational modes in the range of 1030 cm^{-1} to 600 cm^{-1}. All vibrational modes observed for Ru-N are of very low intensities. Based on the literature [76], the Ru-N vibrational band has been reported to appear at lower vibrational energy region of 384 cm^{-1}. Furthermore, the presence of the assigned vibrational energy band at 1784 cm^{-1} in the IR spectrum of S2* (Figure 12) is associated with the keto (C═O) groups. In Table 3, this vibrational energy bands have been assigned to two vibrational modes (symmetric stretching which occur at 1784 cm^{-1} and asymmetric stretching occurring at 1751 cm^{-1}) and are observed to be slightly shifted towards lower energies (shorter wavenumbers) in S2* compared to S2.

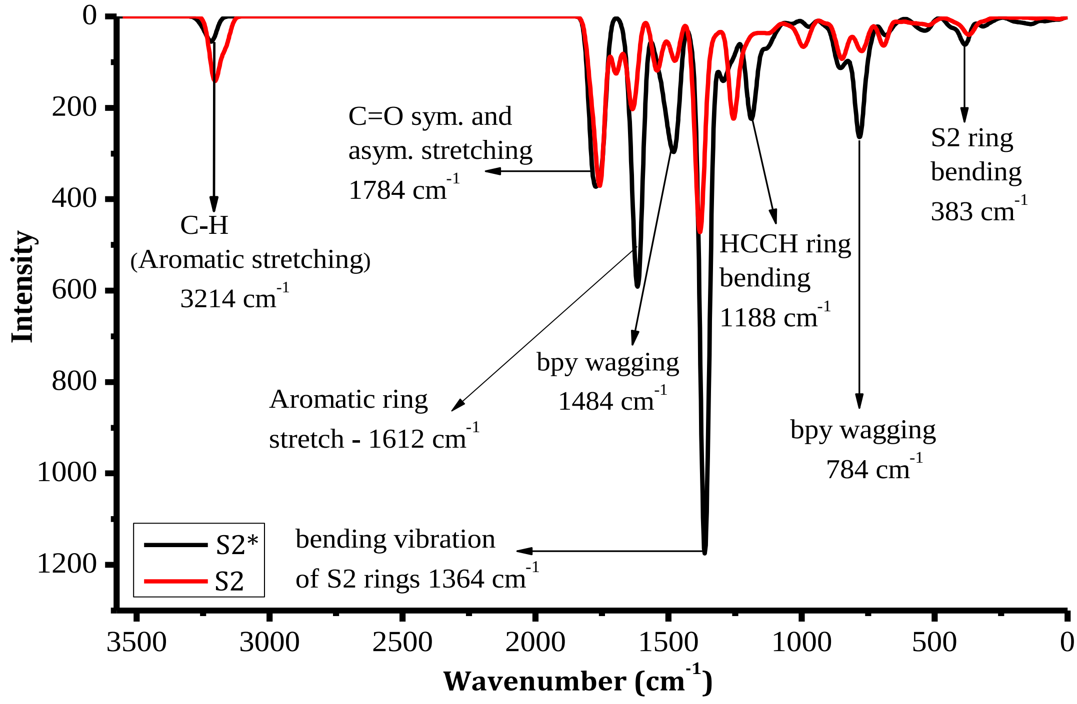

Figure 12. Simulated IR spectra of S2 and S2* using the OriginPro 8 Software [77].

Table 3. Assigned vibrational frequencies and intensities of the ligand (S2) and dye complex (S2*).

Vibrational bands	**Frequency range (cm^{-1})**		**Intensity**	
	Ligand	**Complex**	**Ligand**	**Complex**
C—H (Aromatics stretching)	~3164 - 3233	~3214	Weak	Very weak
C═O (carbonyl stretching) sym. and asym.	~1788 ~1756	~1784 - 1751	Weak to Very weak	Weak to Medium
C═N imine stretching	~1698	~1675	Very weak	Negligibly weak
C=C (Aromatic rings - bending and stretching)	1657 - 219	~1188, 1612, 1364	Moderate to very weak	Strong to very weak
Ru—N(bpy) Ru—N(S2)	—	~1031, 1035, 645, 649, 657	—	Very weak to negligibly weak

4.3.1 Structural parameters of S2 and S2*

Selected bond lengths, bond angles and dihedral angles of S2 and S2* in vacuum and in different solvents are shown in Table 4 and Table 5. This study was done in order to investigate the effects of solvents on the geometrical parameters (bond lengths, bond angles and dihedral angles) of S2 and S2*. The selected geometrical parameters obtained at vacuum geometry are compared with the geometries obtained in hexane, tetrahydrofuran, acetonitrile and methanol (in order of increasing polarities). The bond lengths, bond angles and dihedral angles associated with the metal(Ru)—ligand(N) coordination bonds in S2* are of main consideration. Additionally, geometrical parameters on the anchoring moiety (the ring containing the C═O) of both S2 and S2* are also reported.

From Table 4 it is observed that these geometrical parameters of S2 do not change significantly in different solvents when compared to vacuum. Clearly, in all solvents, the bond lengths of S2 are slightly longer or shorter in going from vacuum to the most polar solvent, methanol. Considering the bond length of the carbonyl, C17—O21, a range of 1.220 Å - 1.225 Å has been obtained from vacuum to methanol, whereas the bond length between N37—C38 of the coordinating atom increases from 1.336 Å in vacuum to 1.339 Å in methanol. A decrease in bond length from 1.412 Å in vacuum to 1.410 Å in methanol is observed between C17—N19 of the anchoring moiety. As for the bond angles, the O21-C17-N19 angle is observed to be larger in vacuum (120.9°) and smaller in methanol (120.3°), while the angle between C34-N37-C38 remained unchanged for all the solvents with an angle of 117.8°. For dihedral angle, the C17-N19-C22-C2 angle was observed to be smaller in hexane (90.4°) and larger in vacuum (103.2°), meaning that the two rings are more perpendicular in hexane than in vacuum. Meanwhile, the dihedral angle for N32-C33-C34-N37 ranges from 162.8°

in vacuum to 161.4° in tetrahydrofuran. Overall, it's worth mentioning that the selected geometrical parameters are observed to behave similarly in a smaller basis set (B3LYP/3-21G(d), data with an asterisk in Table 4) and the geometrical parameters obtained in acetonitrile and methanol are similar in both basis sets. The only observed contradiction between the two basis sets is the trend in the dihedral angle between C17-N19-C22-C2.

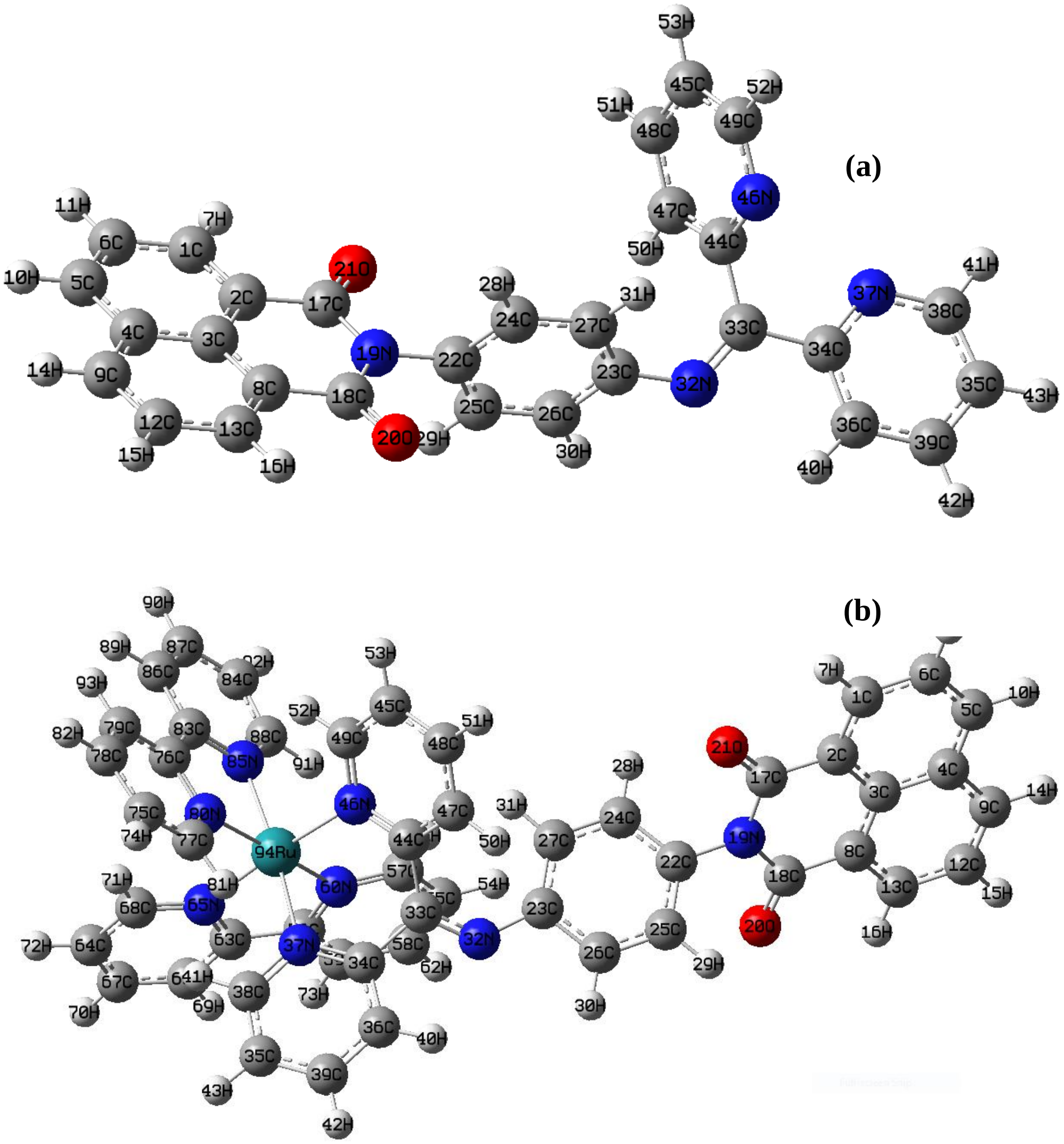

Figure 13. Optimized structures of S2 (a) and S2* (b) in vacuum at B3LYP/6-31G(d,p).

Table 4. Selected Geometrical parameters of optimized S2 in vacuum and in selected various solvents at B3LYP/6-31G(d,p) and at B3LYP/3-21G(d) (data with asterisks).

Parameter	**Vac**	**Hex**	**Thf**	**Acn**	**Meoh**
Bond lengths (Å)					
C17—O21	1.220	1.222	1.224	1.225	1.225
	1.237*	1.238*	1.239*	1.239*	1.239*
C17—N19	1.412	1.411	1.410	1.410	1.410
	1.421*	1.420*	1.415*	1.415*	1.415*
N19—C22	1.446	1.447	1.446	1.446	1.446
	1.451*	1.450*	1.452*	1.452*	1.452*
C23—N32	1.406	1.406	1.407	1.407	1.407
	1.405*	1.406*	1.409*	1.410*	1.410*
N32—C33	1.284	1.284	1.284	1.284	1.284
	1.285*	1.285*	1.285*	1.285*	1.285*
C34—N37	1.343	1.344	1.345	1.345	1.345
	1.349*	1.350*	1.351*	1.351*	1.351*
N37—C38	1.336	1.337	1.337	1.338	1.338
	1.349*	1.349*	1.350*	1.350*	1.350*
C44—N46	1.342	1.342	1.343	1.344	1.344
	1.351*	1.351*	1.351*	1.352*	1.352*
N46—C49	1.337	1.338	1.339	1.340	1.340
	1.352*	1.353*	1.354*	1.355*	1.355*
Bond angles (°)					
C17-N19-C18	125.3	125.4	125.4	125.4	125.4
	124.7*	124.9*	125.8*	125.8*	125.8*
O21-C17-N19	120.9	120.6	120.4	120.3	120.3
	121.4*	121.2*	120.9*	120.8*	120.8*
C27-C23-N32	122.8	122.7	122.5	122.5	122.5
	125.6*	125.4*	124.7*	124.5*	124.5*
C23-N32-C33	123.7	123.7	123.7	123.7	123.7
	131.6*	131.1*	129.6*	129.0*	129.0*
C34-C33-C44	117.0	117.1	117.2	117.3	117.3
	115.3*	115.2*	115.0*	114.9*	114.9*
C34-N37-C38	117.8	177.8	117.8	117.8	117.8
	118.4*	118.4*	118.3*	118.2*	118.2*
C44-N46-C49	117.5	117.4	117.4	117.4	117.4
	118.4*	118.3*	118.1*	118.0*	118.0*
Dihedral angle (°)					
C17-N19-C22-C24	103.2	90.4	90.6	90.6	90.6
	54.0*	57.5*	84.0*	85.4*	85.3*
N32-C33-C34-N37	162.8	161.6	161.4	162.4	162.4
	179.0*	179.7*	178.5*	177.4*	177.4*
N32-C33-C44-N46	115.1	115.7	115.8	115.0	115.0
	59.1*	61.5*	67.4*	70.5*	70.4*

Table 5. Geometrical parameters of optimized S2* in vacuum and in selected various solvents at B3LYP/6-31G(d,p) and at B3LYP/3-21G(d) (data with asterisks).

Parameter	**Vac**	**Hex**	**Thf**	**Acn**	**Meoh**
Bond length (Å)					
94Ru—N37	2.149	2.149	2.145	—	2.144
	2.119*	2.119*	2.114*	2.114*	2.114*
94Ru—N46	2.146	2.148	2.148	—	2.146
	2.107*	2.105*	2.105*	2.105*	2.105*
94Ru—N65	2.105	2.103	2.102	—	2.101
	2.078*	2.078*	2.075*	2.075*	2.075*
94Ru—N60	2.113	2.111	2.108	—	2.106
	2.082*	2.081*	2.078*	2.077*	2.077*
94Ru—N80	2.104	2.100	2.099	—	2.100
	2.076*	2.075*	2.075*	2.074*	2.074*
94Ru—N85	2.099	2.097	2.094	—	2.095
	2.075*	2.074*	2.074*	2.073*	2.073*
C17—O21	1.222	1.222	1.225	—	1.225
	1.239*	1.239*	1.239*	1.239*	1.239*
N37—C34	1.356	1.357	1.356	—	1.356
	1.365*	1.365*	1.365*	1.365*	1.365*
C33—N32	1.286	1.285	1.284	—	1.284
	1.291*	1.289*	1.288*	1.288*	1.288*
Bond angle (°)					
C17-N19-C18	125.0	125.3	125.5	—	125.6
	123.9*	124.5*	125.0*	125.2*	125.2*
C23-N32-C33	130.7	129.5	129.0	—	128.9
	132.2*	131.4*	130.6*	130.0*	130.0*
O21-C17-N19	120.1	120.2	120.2	—	120.1
	120.5*	120.6*	120.7*	120.7*	120.7*
C34-N37-C38	117.7	117.7	117.6	—	117.6
	118.0*	117.9*	117.9*	117.8*	117.8*
N46-Ru94-N37	87.2	87.4	87.5	—	87.4
	87.7*	87.8*	87.9*	88.1*	88.1*
N80-Ru94-N85	78.0	78.1	78.2	—	78.2
	78.8*	78.8*	78.9*	78.9*	78.9*
N60-Ru94-N65	77.6	77.7	77.7	—	77.7
	78.5*	78.5*	78.5*	78.6*	78.6*
Dihedral angle (°)					
C17-N19-C22-C24	54.1	61.9	74.3	—	93.3
	42.3*	47.5*	54.9*	58.7*	58.5*
N32-C33-C34-N37	144.7	146.7	147.0	—	146.7
	148.8*	148.5*	150.8*	152.1*	152.1*
C44-C33-C34-N37	44.0	42.3	42.0*	—	42.1
	41.3*	41.5*	39.7*	38.4*	38.4*

Geometry optimization of S2* could not be achieved in acetonitrile due to convergence problems. However, optimized geometries in all solvents including acetonitrile were obtained and reported with the smaller basis set, B3LYP/3-21G(d) as displayed in Table 5. Since the geometrical parameters of S2* in the larger 6-31G(d,p) basis set is similar to that of the smaller 3-21G(d) basis set, the results of the latter have been used to discuss the effect of solvents on the geometrical parameters of S2*.

From Table 5 and Figure 13, the bonds connecting the S2 moiety to the ruthenium atom are 94Ru—N37 and 94Ru—N46, respectively. However, since S2* is an octahedral ruthenium complex, the four coordinating bonds from the two bpy ligands are also reported. 94Ru—N37 bond length is longer in vacuum (2.149 Å) compared to its corresponding value in methanol (2.144 Å), while the 94Ru—N46 bond length is shorter in vacuum (2.146 Å) when compared to 2.148 Å computed in hexane and tetrahydrofuran. Compared to S2, the bond length between N37—C34 ranges from 1.356 Å in vacuum to 1.357 Å in hexane and the bonds are elongated in S2*. Meanwhile, the N46-Ru94-N37 angle is noticed to be smaller in vacuum (87.2°) and larger in tetrahydrofuran (87.5°). Additionally, the angle in C34-N37-C38 ranges from 117.7° in vacuum to 117.6° in methanol, which when compared to S2 they are slightly reduced. Moreover, the dihedral angle of S2* between C17-N19-C22-C24 is reported to range from 54.1° in vacuum to 93.3° in methanol, making the two rings to be more orthogonal in the most polar solvent just like in S2. For N32-C33-C34-N37, the dihedral angle is smaller in vacuum (144.7°) and larger in tetrahydrofuran (147.0°), an opposite scenario observed with S2. Overall, just like in S2, the effect of solvents on the geometrical parameters of S2* is very insignificant and does not change the bond lengths to more than a difference of 0.05 Å when compared.

4.3.2 Frontier molecular orbitals and theoretical spectral properties

Table 6 summarizes the HOMO (H) and LUMO (L) energy levels, as well as the HOMO-LUMO energy gap (3.32 eV) of S2 and S2* in vacuum, hexane, tetrahydrofuran, acetonitrile and methanol. Noticeably, observation on S2 shows that the smallest HOMO-LUMO gap is associated with the least polar solvent (hexane) which means that S2 is less kinetically stable in hexane and more kinetically stable in acetonitrile and methanol which exhibits the largest H-L energy gap of 3.78 eV [71–73]. Most importantly, the solvents stabilize the LUMO and HOMO energy levels of S2 ongoing from the least polar solvent (hexane) to the most polar solvent (methanol) when compared to vacuum. This implies that the HOMO of S2 reduces its ability to easily donate electrons in more polar solvents (acetonitrile and methanol) because it is easier for the HOMO to donate an electron when its energy is higher [78]. LUMO as an electron acceptor shows its ability to easily accept an electron in acetonitrile and methanol because the lower the LUMO energy the easier it can accept an electron [78]. On the contrary, S2* is observed to be less kinetically stable (most chemically reactive) in vacuum with a H-L energy gap of 2.07 eV but more kinetically stable (less chemically reactive) in the most polar solvent, methanol, with a large H-L energy gap of 3.27 eV [71–73]. The solvents tend to destabilize the HOMO and LUMO energies of S2* as the solvents increase in polarity in such a way that large HOMO-LUMO energy gaps are obtained.

Table 6. Calculated HOMO/LUMO energies and H-L gap (eV) for the optimized geometries of S2 and S2* in vacuum and various selected solvents computed at B3LYP/6-31G(d,p).

Structure	**Solvent**	**HOMO (a.u.)**	**LUMO(a.u.)**	**H-L Gap (eV)**
S2	Vacuum	-0.214	-0.087	3.46
	n-Hexane	-0.219	-0.088	3.32
	Tetrahydrofuran	-0.226	-0.089	3.73
	Acetonitrile	-0.229	-0.090	3.78
	Methanol	-0.229	-0.090	3.78
S2*	Vacuum	-0.342	-0.266	2.07
	n-Hexane	-0.289	-0.188	2.75
	Tetrahydrofuran	-0.243	-0.122	3.29
	Acetonitrile	-0.223*	-0.111*	3.05*
	Methanol	-0.225	-0.105	3.27

Data in (*) are computed with B3LYP/3-21G(d).

Displayed in Table 7 are the associated frontier molecular orbitals of S2 and S2* in various solvents. In all solvents, the HOMO of S2 is of π character with major contributions from the pi orbitals on the carbons of the phenyl ring. The LUMO of S2 is of π* character with major contributions from the carbons on the naphthalic anhydride ring. As for S2*, the HOMO is of π character in vacuum and hexane with major contributions from the pi orbitals on the naphthalic anhydride carbons, whereas in tetrahydrofuran, acetonitrile and methanol, the HOMO is mainly localized on the d-orbital of the central ruthenium metal. The LUMO of S2* is of π* character, with localization that varies in different solvents. As a result, the LUMO of S2* is localized on one of the bpy rings in vacuum, while in hexane the LUMO is localized on all the bpy rings of the dye complex. Conversely, in tetrahydrofuran, acetonitrile and methanol, the LUMO is localized on the pyridyl rings of the ligand (S2).

Table 7. Analysis of the HOMO and LUMO of S2 and S2* at the optimized geometries in vacuum and various solvents computed at B3LYP/6-31G(d,p).

Solvent	**HOMO**	**LUMO**
Ligand (S2)		
Vac	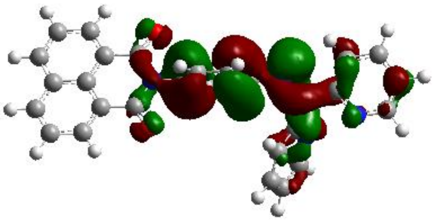	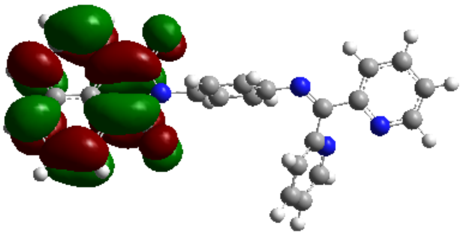
Hex	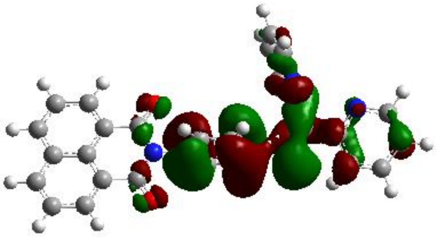	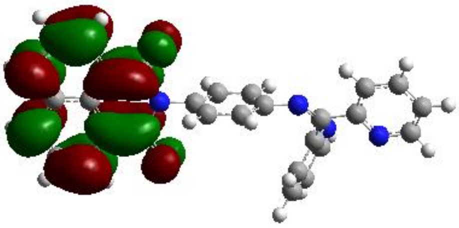
Thf	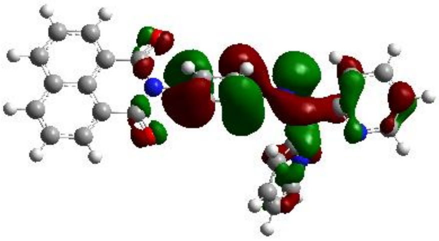	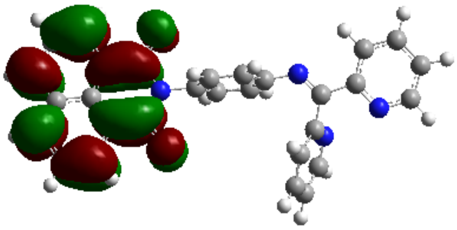
Acn	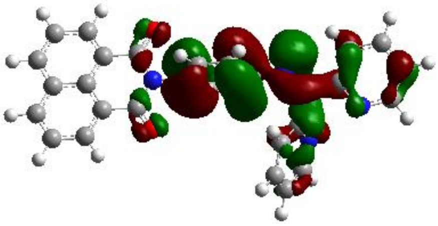	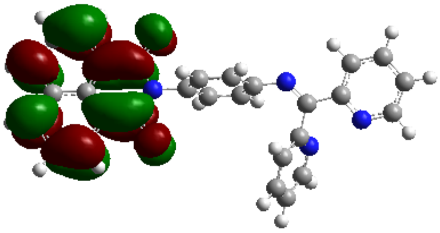
meoh	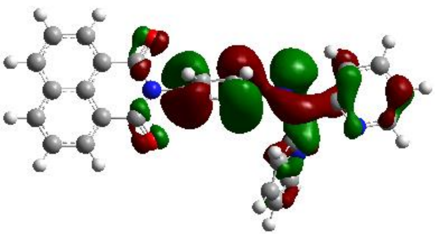	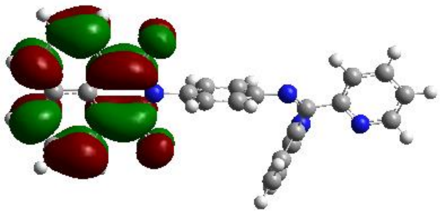

Dye complex (S2*)		
Vac	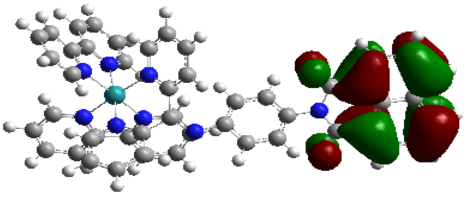	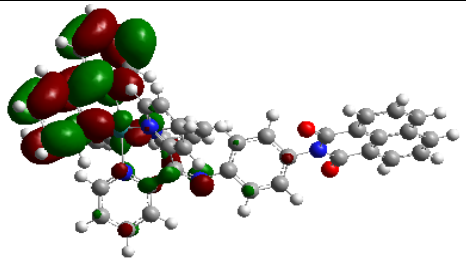
Hex	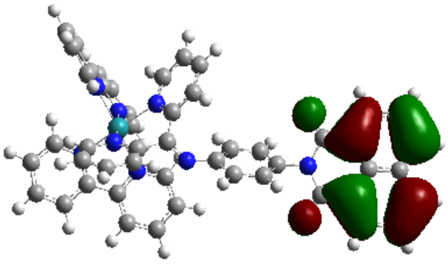	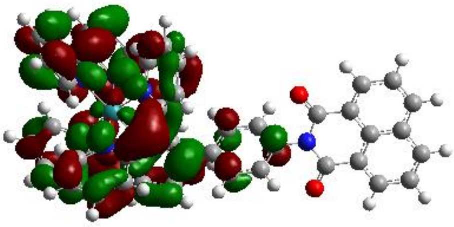
Thf	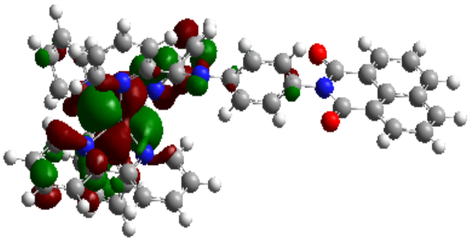	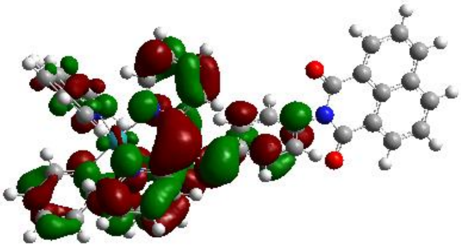
acn*	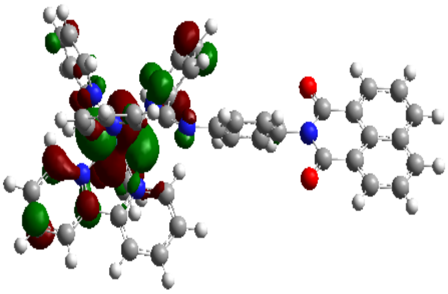	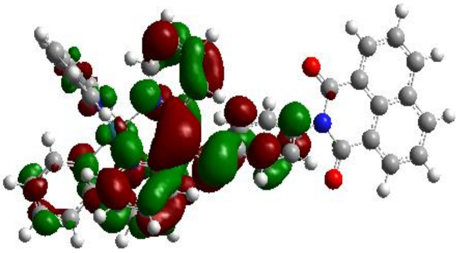
meoh	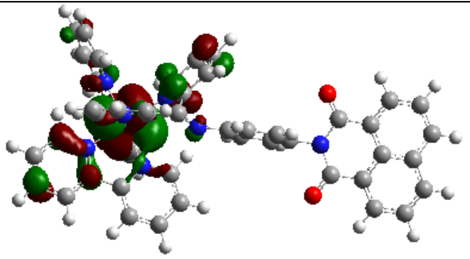	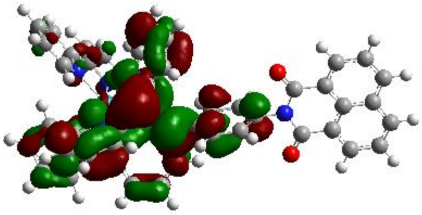

Data in (*) are computed with B3LYP/3-21G(d).

The simulated UV-Vis absorption spectrum of S2 (Figure 14) shows distinctive bands of various intensities in the UV region of $\lambda < 400$ nm. These absorption bands are all attributed to spin and symmetry allowed π - π^* intraligand charge transfer (ILCT) transitions (Figure 15). The absorption band at the wavelength of maximum absorbance, $\lambda_{max} = 336.73$ nm, is due to π - π^* transition associated with the 1,8-naphthalic anhydride moiety of S2 and this has been confirmed in literature [79–81]. Results presented in Figure 15 and Table 8 clearly show that the bands at absorption maxima $\lambda_{max} = 336.73$ nm and $\lambda_{max} = 360.54$ nm involve H-1 → L and a H → L+1 excitations. Specifically, the well enhanced higher energy band at $\lambda_{max} = 336.73$ nm involves a transition within the 1,8-naphthalic anhydride moiety while the shoulder band at $\lambda_{max} = 360.54$ nm is a charge transfer transition band between the phenyl ring and the pyridyl moiety. Assignment of these transitions agrees with literature reports on 1,8-naphthalic anhydride derivatives [79,82]. The less-intense π - π^* transition band at $\lambda_{max} = 305.88$ nm corresponds to H-2 → L+1 excitation of the pyridyl rings and the shoulder at $\lambda_{max} = 277.23$ nm is ascribed to as the π - π^* transition band between the pyridine rings of S2, with the largest contribution involving H-8 MO to the L+1 MO. Lastly, the narrow most intense π - π^* transition band at higher energies ($\lambda_{max} = 221.91$ nm) is attributed to the H→ L+8 excitation of the phenyl ring.

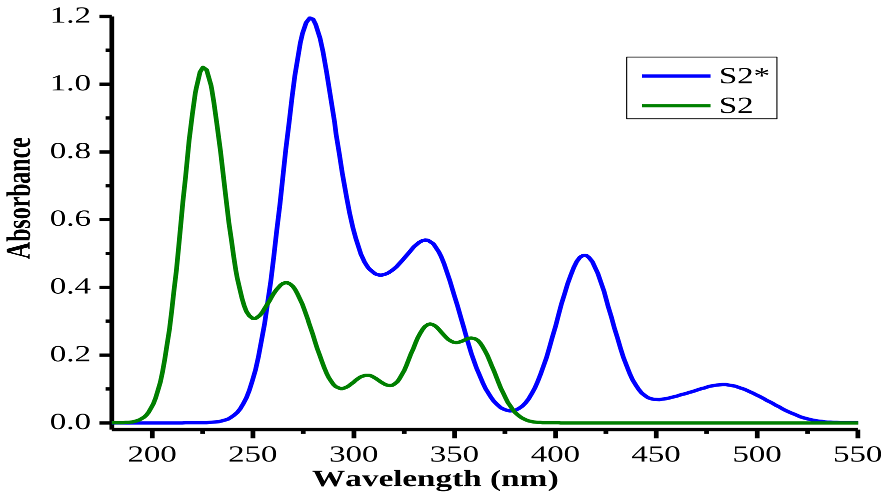

Figure 14. Theoretical UV-Vis plot of S2 and S2* in acetonitrile obtained at B3LYP/6-31G(d,p). (**NB:** S2 is obtained at optimized geometry in acetonitrile and S2* is obtained at optimized geometry in vacuum).

Table 8. Computed vertical excitation energies, MO contribution to major electronic transitions, oscillator strength (f ≥ 0.0500) and calculated H-L energy gaps for the simulated absorption spectra of S2 in various solvents at the B3LYP/6-31G(d,p) level.

S2	Excited State	Excitation Energies (nm)	Oscillator strength, *f*	MO contribution (Major contribution and composition)	H-L Gap (eV)
Vac	2	365.62	0.1881	H → L+1 (89%)	4.22
	4	331.45	0.0788	H-1 → L (53%)	4.05
	5	326.04	0.1778	H-2 → L (46%)	4.14
	7	309.30	0.0697	H-2 → L+1 (67%)	4.90
	13	280.80	0.0803	H-5 → L+1 (37%)	5.36
	18	269.99	0.0957	H → L+3 (27%)	5.17
	21	262.18	0.0953	H → L+5 (27%)	5.44
	23	255.57	0.1103	H → L+5 (47%)	5.44
	24	252.23	0.0814	H-2 → L+4 (28%)	5.85
	38	231.15	0.0724	H-14 → L (27%)	5.85
	49	220.51	0.0507	H-7 → L+4 (22%)	6.45
	50	220.37	0.2180	H → L+8 (15%)	6.04
n-hex	2	364.28	0.2202	H → L+1 (90%)	4.25
	4	333.60	0.2655	H-1 → L (89%)	4.05
	7	308.34	0.0912	H-2 → L+1 (73%)	4.87
	13	279.89	0.1079	H-8 → L+1 (32%)	5.50
	18	269.31	0.0799	H-5 → L+1 (41%)	5.36
	19	263.04	0.1990	H-8 → L+1 (38%)	5.50
	22	254.84	0.0591	H → L+6 (66%)	5.61
	37	231.92	0.1977	H-14 → L (30%)	5.82
	42	225.26	0.0870	H-2 → L+4 (44%)	5.90
	43	224.93	0.0652	H-10 → L+1 (62%)	5.50
	44	224.56	0.2445	H-10 → L+1 (23%)	5.93
	45	222.92	0.0869	H-3 → L+2 (20%)	6.10
	47	221.43	0.2774	H → L+8 (26%)	6.07
Thf	2	361.79	0.2318	H → L+1 (90%)	4.30
	3	336.26	0.2869	H-1 → L (96%)	4.03
	7	306.53	0.0979	H-2 → L+1 (72%)	4.90
	13	278.06	0.1362	H-8 → L+1 (43%)	5.52
	17	268.79	0.0726	H-6 → L+1 (37%)	5.39
	19	263.58	0.2203	H-4 → L+1 (39%)	5.28
	21	252.52	0.0517	H → L+6 (65%)	5.66
	37	232.32	0.1784	H-1 → L+3 (32%)	5.69
	41	225.65	0.4304	H-1 → L+4 (58%)	5.74

	44	222.18	0.2541	H → L+8 (32%)	6.10
	46	220.67	0.1237	H-8 → L+2 (28%)	6.50
Acn	2	360.54	0.2339	H → L+1 (90%)	4.30
	3	336.73	0.2785	H-1 → L (96%)	4.03
	7	305.88	0.0928	H-2 → L+1 (71%)	4.90
	13	277.23	0.1489	H-8→ L+1 (44%)	5.50
	17	268.48	0.0651	H-6 → L+1 (29%)	5.36
	18	263.69	0.1087	H-8→ L (49%)	4.98
	19	263.67	0.1114	H-8→ L (48%)	4.98
	37	232.14	0.1584	H-13→ L (36%)	5.77
	41	225.56	0.2806	H-1→ L+4 (39%)	5.77
	42	225.23	0.1793	H-10→ L+1 (50%)	5.93
	45	221.91	0.3111	H→ L+8 (34%)	6.10
	47	220.25	0.0569	H-8 → L+2 (34%)	6.50
Meoh	2	360.52	0.2322	H → L+1 (90%)	4.30
	3	336.55	0.2775	H-1 → L (96%)	4.03
	7	305.87	0.0923	H-2 → L+1 (71%)	4.90
	13	277.23	0.1469	H-8 → L+1 (44%)	5.50
	17	268.47	0.0646	H-6 → L+1 (30%)	5.36
	19	263.63	0.2183	H-5 → L+1 (39%)	5.25
	37	232.08	0.1556	H-13 → L (37%)	5.77
	41	225.48	0.1925	H-10 → L+1 (46%)	5.93
	42	225.16	0.2649	H-10 → L+1 (34%)	5.93
	45	221.89	0.3090	H → L+8 (34%)	6.12
	47	220.26	0.0593	H-8 → L+2 (34%)	6.50

Table 9. Computed vertical excitation energies, MO contribution of major electronic transitions, oscillator strength ($f \geq 0.0500$) and calculated H-L energy gaps for the simulated absorption spectra of S2* in various solvents at the B3LYP/6-31G(d,p) level.

S2*	Excited State	Excitation Energies (nm)	Oscillator strength, *f*	MO contribution (Major contribution and composition)	H-L Gap (eV)
Vac	4	520.83	0.1254	H-1 → L (51%)	2.69
	11	459.98	0.2367	H-1 → L+2 (60%)	3.07
	48	337.61	0.0528	H → L+9 (84%)	3.95
	49	336.80	0.2002	H → L+10 (64%)	3.97
Hex	3	475.20	0.1311	H-1 → L (32%)	3.18
	6	460.61	0.1795	H-4 → L+1 (32%)	3.59
	7	446.19	0.0838	H-5 → L (29%)	3.62
	10	432.33	0.0681	H-5 → L+1 (44%)	3.70
	28	340.28	0.1270	H → L+7 (27%)	4.00
	29	339.85	0.1635	H → L+7 (32%)	4.00
	32	338.24	0.0739	H-6 → L+2 (58%)	4.03
Thf	2	472.10	0.0745	H-1 → L (54%)	3.40
	8	420.44	0.1695	H-3 → L+1 (60%)	3.73
	9	414.28	0.1855	H-4 → L (84%)	3.67
	22	338.69	0.0624	H-1 → L+5 (22%)	4.52
	23	338.26	0.2691	H-2 → L+3 (84%)	4.00
	43	307.36	0.0526	H-5 → L+3 (80%)	4.68
	49	299.16	0.0799	H-12 → L (22%)	4.95
	65	283.08	0.0773	H-9 → L+1 (27%)	4.82
	68	279.44	0.0528	H-13 → L (31%)	5.06
	70	278.09	0.1572	H-8 → L+2 (20%)	4.93
Acn	2[a]	482.97[a]	0.0872[a]	H-1 → L (78%)[a]	3.32[a]
	2[b]	508.99[b]	0.1040[b]	H-1 → L (76%)[b]	3.16[b]
	8[a]	421.04[a]	0.1437[a]	H-2 → L+1 (60%)[a]	3.70[a]
	8[b]	434.45[b]	0.1598[b]	H-2 → L+1 (59%)[b]	3.62[b]
	9[a]	412.27[a]	0.3656[a]	H-3 → L (89%)[a]	3.59[a]
	9[b]	422.10[b]	0.2363[b]	H-3 → L (89%)[b]	3.62[b]
	14[b]	361.15[b]	0.0716[b]	H → L+4 (79%)[b]	4.19[b]
	22[a]	339.64[a]	0.1318[a]	H-1 → L+5 (24%)[a]	4.52[a]

	23 [a]	339.12 [a]	0.1846 [a]	H-4 → L+2(53%) [a]	4.00 [a]
	28 [b]	327.67 [b]	0.2533 [b]	H-4 → L+2 (44%) [b]	4.11 [b]
	30 [b]	326.13 [b]	0.0889 [b]	H-5 → L+2 (44%) [b]	4.82 [b]
	31 [b]	324.99 [b]	0.0770 [b]	H-1 → L+7 (42%) [b]	4.60 [b]
	45 [a]	306.65 [a]	0.0509 [a]	H-2 → L+7 (58%) [a]	4.79 [a]
	56 [a]	286.53 [a]	0.0518 [a]	H-11 → L (15%) [a]	4.98 [a]
	58 [a]	284.67 [a]	0.0682 [a]	H-8 → L+1 (25%) [a]	4.79 [a]
	63 [b]	274.15 [b]	0.1050 [b]	H-13 → L (35%) [b]	5.14 [b]
	64 [a]	278.27 [a]	0.2052 [a]	H-8 → L+3 (42%) [a]	4.93 [a]
	66 [a]	276.40 [a]	0.2670 [a]	H-3 → L+7 (22%) [a]	4.95 [a]
	67 [a]	275.78 [a]	0.1138 [a]	H-8 → L+3 (12%) [a]	4.93 [a]
	68 [a]	274.65 [a]	0.1911 [a]	H-4 → L+4 (24%) [a]	4.79 [a]
	69 [a]	274.43 [a]	0.1066 [a]	H-4 → L+4 (64%) [a]	4.79 [a]
meoh	2	476.29	0.0735	H-1 → L (77%)	3.37
	8	419.57	0.1281	H-2 → L+1 (63%)	3.73
	9	401.22	0.2450	H-4 → L (87%)	3.81
	22	337.51	0.2797	H-3 → L+2 (83%)	4.03
	48	294.11	0.0668	H-11 → L (29%)	4.98
	62	278.66	0.0742	H-6 → L+3 (28%)	4.87
	64	277.27	0.1134	H-8 → L+3 (46%)	4.93
	65	277.10	0.0932	H-7 → L+3 (23%)	4.93
	68	273.91	0.1239	H-4 → L+6 (21%)	5.06
	69	273.31	0.5291	H-7 → L+3 (20%)	4.93
	70	272.62	0.1270	H-4 → L+6 (39%)	5.06

a excitation energies of S2* in acn obtained at 6-31G (d,p) at opt geometry in vac.
b excitation energies of S2* in acn obtained at 3-21G(d) at opt geometry in acn.

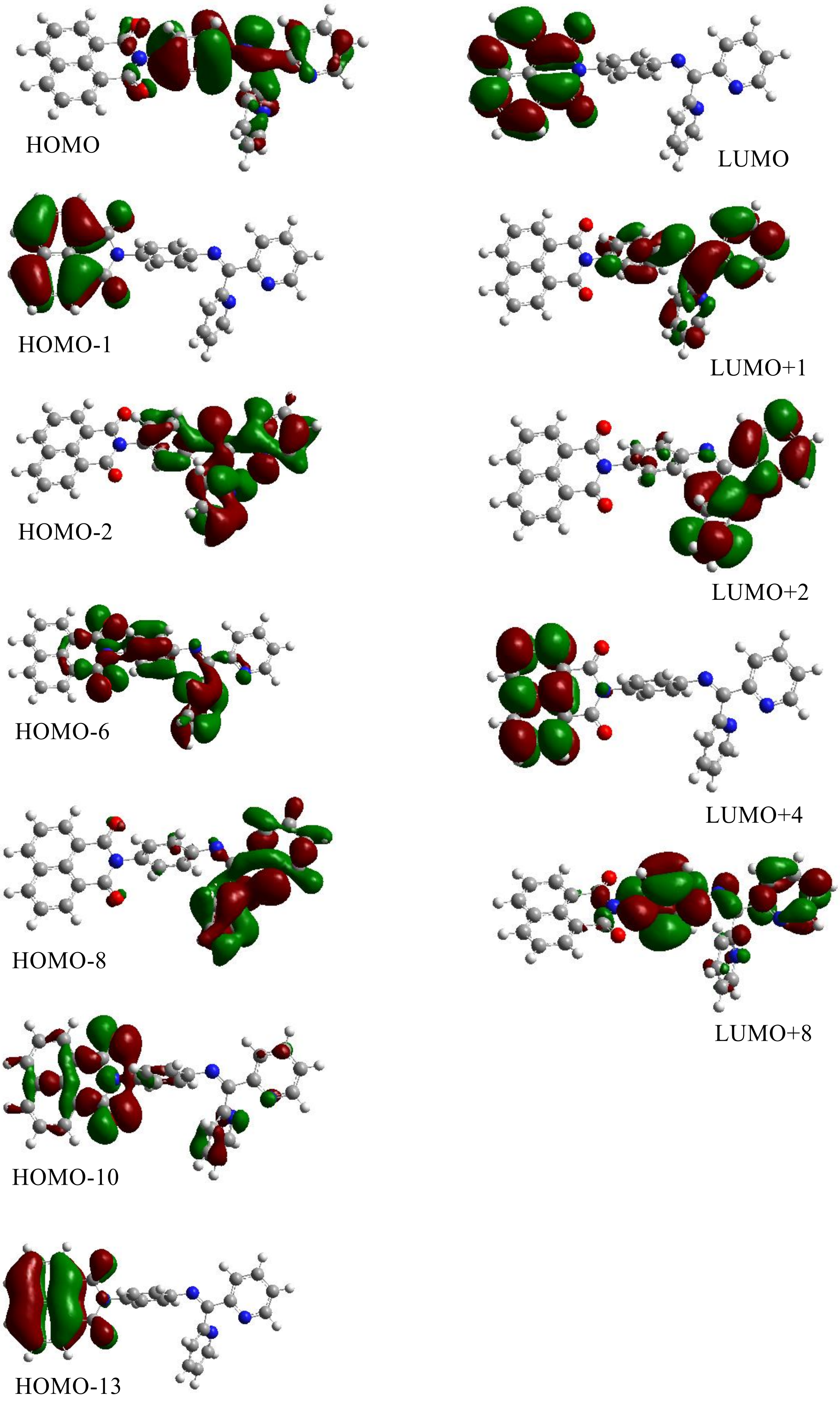

Figure 15. Frontier MO of S2 associated with the main transitions in acetonitrile computed using B3LYP/6-31G(d,p) optimized geometry in acetonitrile.

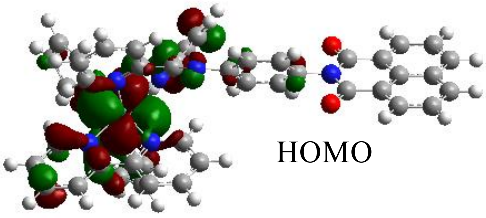

HOMO

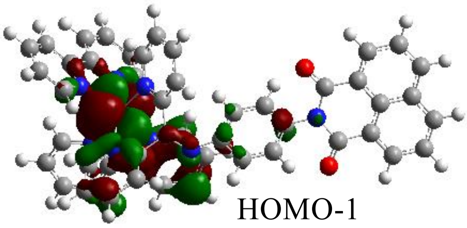

HOMO-1

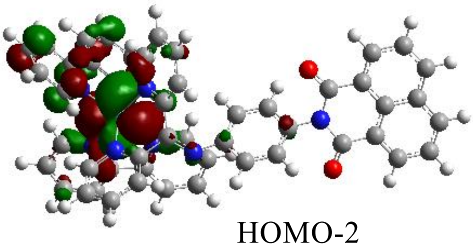

HOMO-2

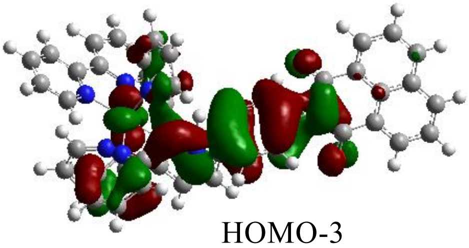

HOMO-3

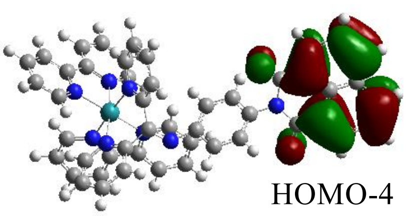

HOMO-4

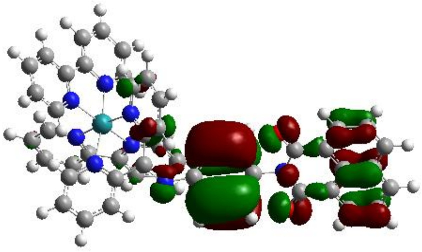

HOMO-5

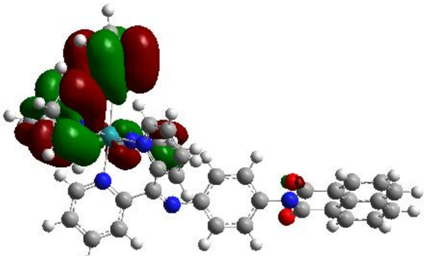

HOMO-8

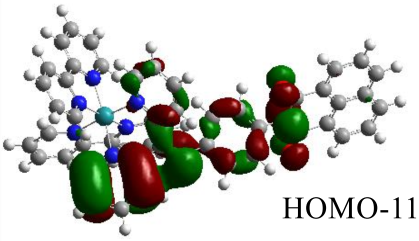

HOMO-11

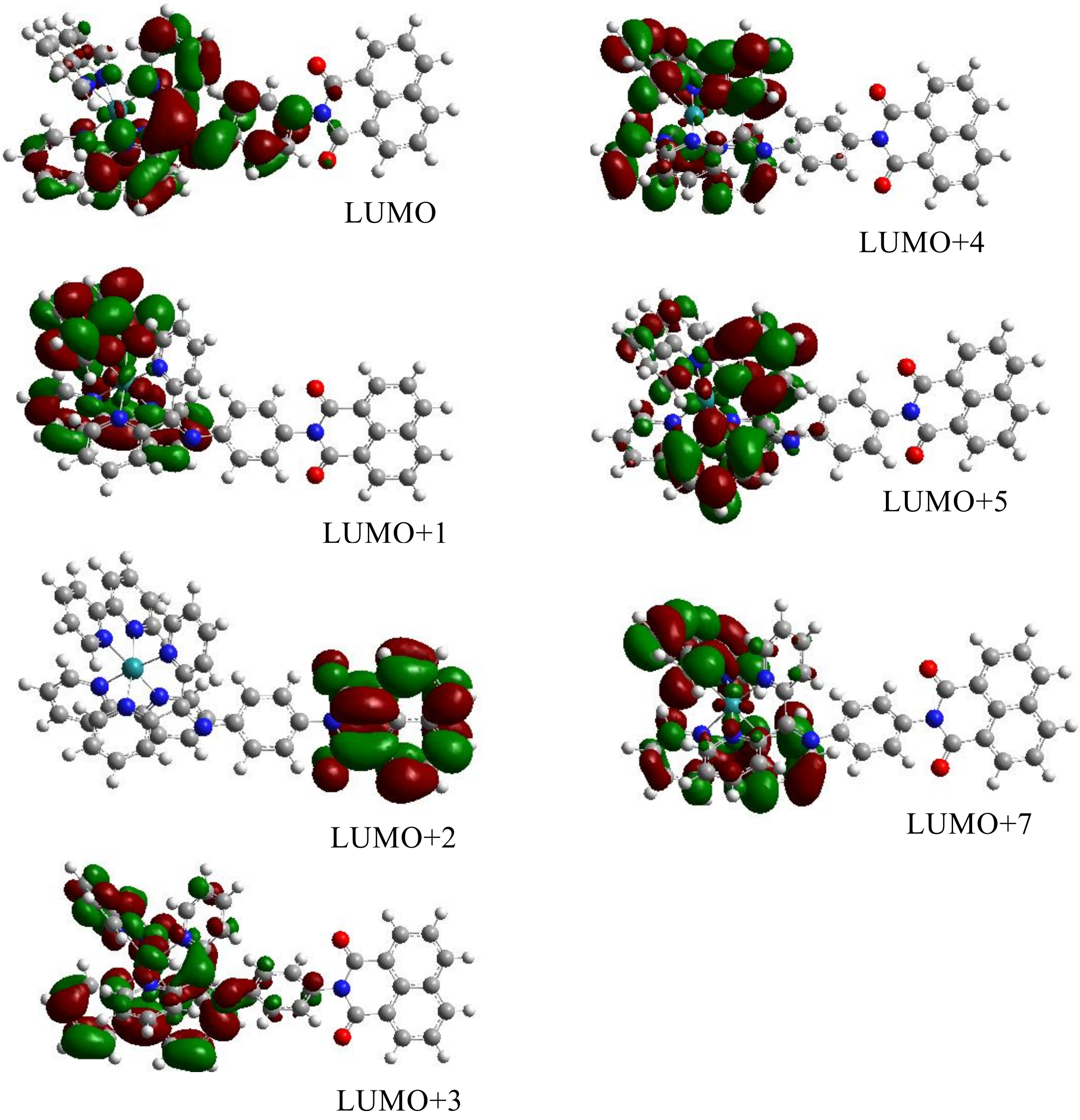

LUMO

LUMO+4

LUMO+1

LUMO+5

LUMO+2

LUMO+7

LUMO+3

Figure 16. Frontier MO of S2* associated with the main transitions in acetonitrile computed using B3LYP/6-31G(d,p) optimized geometry in vacuum.

The simulated absorption spectrum of S2* in acetonitrile is included in Figure 14 and detailed information of the excitation energies are summarized in Table 9. The spectrum of S2* displays four distinct absorption bands with two bands positioned in the 400 nm – 700 nm visible region and the other two bands positioned in the 200 nm – 350 nm UV region. The most intense narrow absorption band at higher energies, λ_{max} = 276.40 nm, is ascribed to an ILCT transition band of π - π* character. The major contribution to this band results from the H-3 MO of the S2 moiety to the L+7 MO of the two bpy groups. Additionally, the π - π* transition band at λ_{max} = 339.12 nm is due to excitation from H-4 MO to L+2 MO within the 1,8-naphthalic anhydride moiety of the attached S2 moiety of S2*. This band can be related to the π - π* transition band of S2 at λ_{max} = 336.73 nm bathochromically shifted by 2.39 nm in the dye complex (S2*). Furthermore, the intense narrow absorption band at λ_{max} = 412.27 nm is attributed to a π - π* ILCT transition between the phenyl ring and the pyridyl rings of the attached S2 ligand. This transition is due to an excitation that originates from the HOMO-3 energy orbital of the phenyl ring to the LUMO energy orbital of the pyridyl rings with a major contribution of 89%. When compared to the spectrum of S2, this absorption band can be somewhat related to the π - π* transition band of S2 at λ_{max} = 360.54 nm with a shift in wavelength (51.73 nm) towards lower energies in the dye complex (S2*).

The bands in the visible region of the spectrum are of significant importance in the study of DSSCs as they represent the photoresponse properties of the dye molecule as a light-harvesting dye sensitizer. Generally, an ideal dye should harvest light over the wavelength of visible range in the UV-Vis spectrum because that region consists of about 43% of the incoming solar radiation [4,18]. In most cases, for a metal dye complex, the low energy absorption band in the visible region of the UV-Vis spectra is usually ascribed to a metal-ligand charge transfer (MLCT) transition through which the photoinduced charge is injected into the conduction band of TiO_2 [12]. Based on this information, the low-intense broad absorption band at λ_{max} = 482.97 nm in Figure 14 is assigned to the MLCT (d - π*) transition of which electron excites from the $d_z{}^2$-orbital of the centred-ruthenium metal to the π- orbitals of the ligand (S2). From Table 9 and Figure 16, this MLCT excitation originates from the HOMO-1 orbital (t_{2g}) localized on the Ru metal to the LUMO orbital of S2 which is a π- orbital.

The energy gap accompanying this transition has been calculated as 3.32 eV which measures the splitting between the two involved MOs and it almost matches the band gap value of 3.23 eV of TiO_2 [83,84]. However, in order to compare the calculated energy gap with the experimental energy gap, the following equation was used to obtain the corrected HOMO-LUMO gap from the theoretical values: $E_{H-Lcorr} = -0.51 + 0.99(H - L_{calc})$, where, -0.51 and 0.99 are constants which account for the average absolute errors for the hybrid functional used in the theoretical calculations of this study [85]. Aided by the preceding equation, the corrected energy gap obtained for the photoexcitation of the dye into the MLCT band was 2.78 eV. This energy gap is analogous to that of the TiO_2 semiconductor and marks the onset photoresponse of S2* to be above the wavelength of 446 nm in the visible range of the UV-Vis spectrum.

The results obtained so far confirm S2* to be an ideal dye due to acceptable photoresponse properties at which the dye absorbs light over the visible range of 446 – 530 nm at λ_{max} = 482.97 nm with an oscillator strength, *f*, of 0.0872. However, an ideal dye should not only absorb light of wavelength across the visible region of the UV-Vis spectra but should also exhibit other cell properties for improved overall cell conversion efficiency. Therefore, an ideal dye should, in addition, consist of the

LUMO eigenvalues greater than -4.05 eV energy of the TiO_2 conduction band (CB) in order to promote efficient charge transfer of the photoexcited electrons [86–88]. Moreover, the dye HOMO eigenvalues should be slightly lower than the HOMO (-4.9 eV) energies of the redox couple (I^-/I_3^-), in order to ensure efficient regeneration of the oxidized dye [87,89,90]. For S2* the occupied molecular orbital (HOMO-1) at which the dye excites into the MLCT transition have been calculated as -6.20 eV which is 1.3 eV units below that of the redox couple, implying that S2* can regenerate the oxidized dye effectively, however, this process will not occur efficiently due to a larger gap between the HOMO energy levels. On the other hand, the calculated LUMO (-2.88 eV) of S2* is 1.2 eV above the CB of TiO_2 value indicating that electrons can be efficiently injected into the CB of TiO_2. The HOMO-LUMO energy levels of S2* which account for the MLCT transition are graphically presented in Figure 17 below.

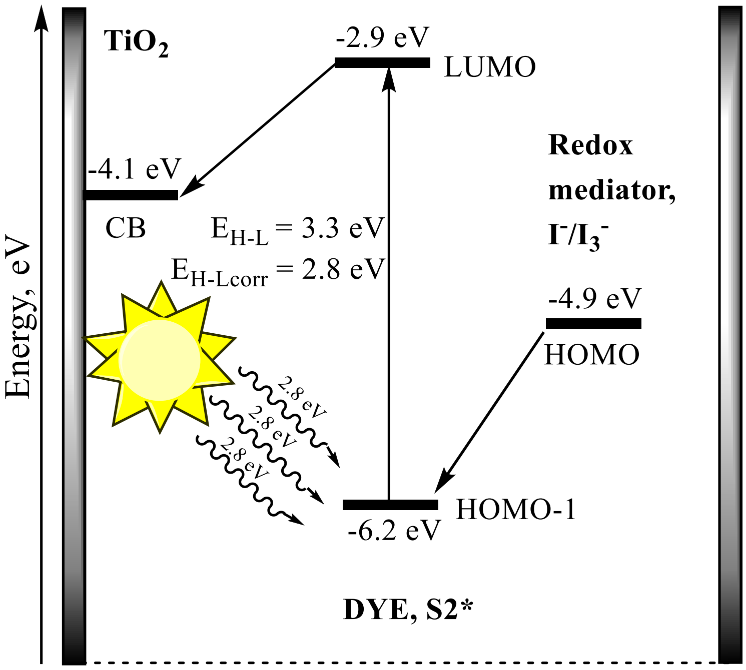

Figure 17. Energy levels of S2* in its oxidized (LUMO) and reduced (HOMO-1) states.

4.3.3 Theoretical solvatochromic studies

Figure 18 shows the simulated solvatochromic spectra of S2 in various solvents of different dielectric constants. Table 10 gives a detailed interpretation of the solvent-solute interaction of S2 in the solvatochromic spectra. As discussed previously, the observed absorption bands in S2 are all due to the $\pi - \pi^*$ transition with excitations involving different molecular orbitals. The absorption spectrum of S2 exhibit five distinct absorption bands (I, II, III, IV and V) which are all affected significantly by the presence of solvents on the surrounding structure of S2. Depending on the nature of the solvent used, each of these absorption bands varies independently in shape, intensity and most importantly, in their positions (wavelength, λ). Hence, the term solvatochromism is used to describe the behaviour of the molecule due to the solvent interaction of different polarities, causing a change in the absorption bands of the UV-Vis spectra [91,92].

In order of their increasing polarities, i.e. vacuum < hexane < tetrahydrofuran < acetonitrile < methanol, effects of solvent on each absorption band of S2 was done via the investigation of the solvatochromic spectra (Figure 18**)**. Based on the absorption maxima and oscillator strength (Table 10), the investigation was done by comparing the spectra in vacuum to that of selected solvents for individual absorption band. As a result, a very small bathochromic shift was observed for bands I, II and IV in all solvents when compared to vacuum and a small hypsochromic shift was observed for band V in all solvents when compared to vacuum. Band III was not observed in vacuum. Band III is noticed as a newly added absorption band in the spectrum of S2 which, however, is not present in vacuum and hence its formation can be as a result of solvent-interaction with the surrounding structure of S2. Additionally, an overlap between the solvatochromic spectra of S2 in acetonitrile and methanol can be noted in which the two most polar solvents behaves in an optically similar manner.

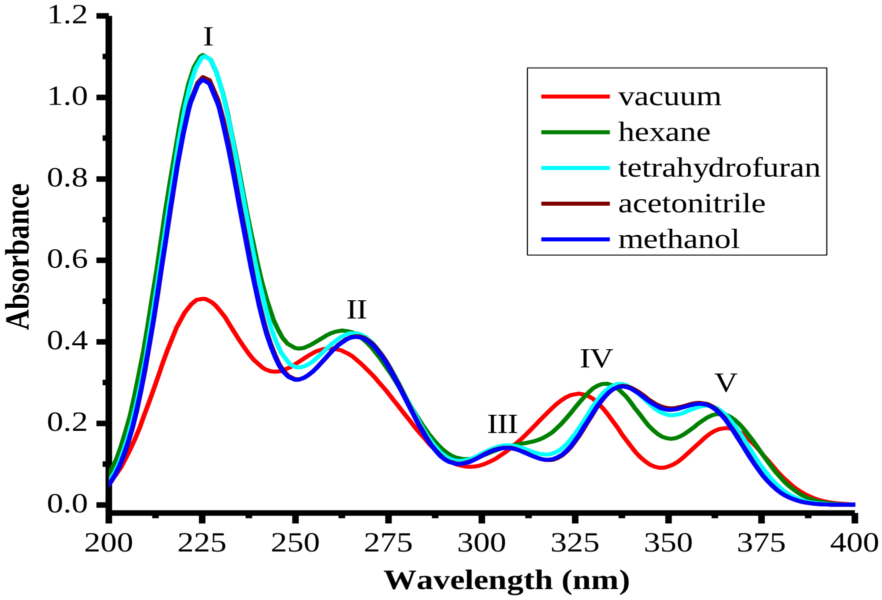

Figure 18. Theoretical UV-Vis plot of S2 in various solvents obtained at B3LYP/6-31G(d,p).

Table 10. Spectral data of S2 based on the peak position (λ_{max}) and oscillator strength (*f*) in different solvents.

Absorption Band	**Solvent**	**λ_{max} (nm)**	***f***
I	Vac	220.37	0.2180
	Hex	221.42	0.2774
	Thf	225.65	0.4304
	Acn	221.91	0.3111
	Meoh	221.89	0.3090
II	Vac	255.57	0.1103
	Hex	263.04	0.1990
	Thf	263.58	0.2203
	Acn	277.23	0.1489
	meoh	263.63	0.2183
III	Vac	—	—
	Hex	308.34	0.0912
	Thf	306.53	0.0979
	Acn	305.88	0.0928
	meoh	305.87	0.0923
IV	Vac	326.04	0.1778
	Hex	333.60	0.2655
	Thf	336.26	0.2869
	Acn	336.73	0.2785
	meoh	336.55	0.2775
V	Vac	365.62	0.1881
	Hex	364.28	0.2202
	Thf	361.79	0.2318
	Acn	360.54	0.2339
	meoh	360.52	0.2322

The solvatochromic behaviour of S2* dye complex was assessed with respect to its MLCT transition band within the visible range of wavelength in vacuum, hexane, tetrahydrofuran, acetonitrile and methanol. This evaluation strictly focused on the interaction of solvents with the MLCT transition involving the d-orbital of the ruthenium central metal and the π-orbitals of S2 ligand in S2* dye. Additionally, this was done in order to account for the successful study of the photoresponse properties within the visible region of the designed S2* dye complex as well as to select the best solvent in terms of photocatalytic enhancement or red-shifting of the visible range towards NIR region.

Figure 19 shows the solvatochromic spectra of S2* dye in vacuum, hexane, tetrahydrofuran, acetonitrile and methanol within the 400 nm to 600 nm visible region. The H-L energy levels, as well as the corrected H-L energy gaps associated with the MLCT transition of S2* in each solvent, are summarized in Table 11. Based on the analysis made on the solvatochromic spectra of the dye complex through the Gaussian TD-DFT output file as well as peak analysis with Gabedit [93] and MO visualization with GaussView, it is obvious that not all visible absorption bands present in the spectra are due to the MLCT transition between Ru-t2g and the π- orbitals of the attached S2 ligand. For clarity, the frontier MOs of S2* in vacuum, hexane, tetrahydrofuran and methanol that are involved with the major transitions as summarized in Table 9 are reported in Figure S3 of Appendix B. From Figure 19, the spectrum of S2* in vacuum shows two distinct absorption bands (λ_{max} = 520.83 nm and λ_{max} = 459.98 nm) within the visible region which are not associated with the MLCT transition. Conversely, with the spectrum of hexane, the absorption band at λ_{max} = 460.61 nm and a shoulder band at λ_{max} = 432.33 nm are of MLCT transition character involving the d-orbital of the ruthenium centre and the π- orbitals of the two bpy rings.

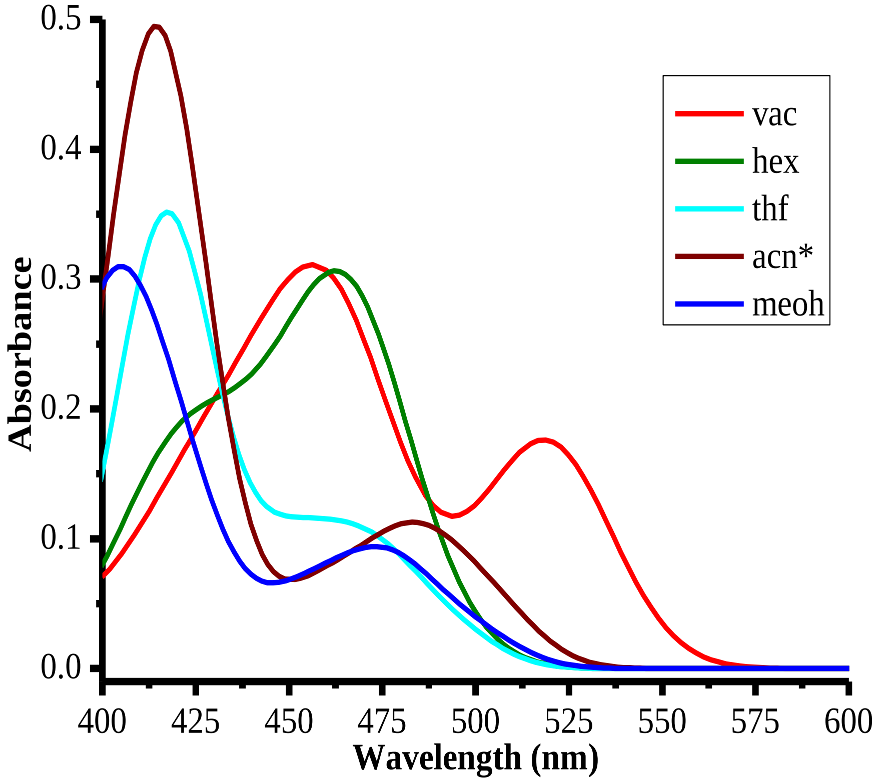

Figure 19. Theoretical UV-Vs plot of S2* in various solvents obtained at the B3LYP/6-31G(d,p). **NB:** (acn* = B3LYP/6-31G(d,p) optimized geometry in vacuum).

Table 11. Solvent effect on the MLCT band of S2* from the d-orbital of Ru to the π-orbitals of S2.

Metal-Ligand Charge Transfer (MLCT) transition band					
	vac	hex	thf	acn*	meoh
λ_{max} (nm)	__	__	472.10	482.92	476.29
F	__	__	0.0745	0.0872	0.0735
Occupied MO (eV)	__	__	-6.72	-6.20	-6.23
Virtual MO (eV)	__	__	-3.32	-2.88	-2.86
E_{gap} (eV)	__	__	3.40	3.32	3.37
Corrected E_{gap} (eV)	__	__	2.86	2.78	2.83

acn* = B3LYP/6-31G(d,p) optimized geometry in vacuum.

With the aid of Figure 19 and Table 11, the MLCT absorption band of λ_{max} = 482.92 nm in acetonitrile is red-shifted by 10.82 nm from tetrahydrofuran and 6.63 nm from methanol. Additionally, the MLCT absorption band in acetonitrile is the most intense in the visible region of the spectra, with the highest oscillator strength of 0.0872 compared to tetrahydrofuran and methanol. The corrected H-L energy gap of acetonitrile is also calculated to be 2.78 eV, showing a narrower energy gap compared to tetrahydrofuran and methanol. However, the corrected H-L gaps of all the polar solvents fall within a range of 2.78 – 2.86 eV, which is in agreement with desired energy gaps reported in the literature for dye sensitizers and is analogous to 3.23 eV, a bandgap of the TiO_2 [83,84]. Consequently, the visible MLCT absorption bands for tetrahydrofuran, acetonitrile and methanol indicate good photoresponse properties within the visible range for an ideal dye absorber [4,8] with acetonitrile being the best solvent of choice. On the basis of the analysis above, acetonitrile is chosen to be the best solvent because it provides the highest degree of photon absorption within the visible range of the spectrum (as measured by the oscillator strength) and extends the functional range of S2* towards the NIR region (as measured by its broad MLCT band and its absorption maxima) [12,35].

4.4 Experimental details on S2*

4.4.1 Synthesis and characterization of S2

The ancillary ligand, S2 (Scheme 1), was synthesized via a two-step procedure. Firstly, compound A1 containing the anchoring group (carbonyl oxygen) was prepared through the reaction of 1,8-naphthalic anhydride and p-phenylenediamine in DMF under refluxing conditions. Secondly, the target ligand, S2, was prepared through the reaction of compound A1 and Di (2-pyridyl) ketone in ethanolic solution at room temperature and a good yield of S2 was obtained as a pale greyish precipitate which was purified through successive washing and recrystallization with ethanol in which reactants were highly soluble. Ligand S2 was designed to anchor to TiO_2 through the carbonyl groups by forming weak interacting bonds with the titanol hydrogens on the surface of TiO_2 [94]. The ^{1}H-NMR results obtained for S2 (Figure S5) shows that the protons adjacent to the nitrogen atom of the pyridine rings and the carbonyl carbon as well as the protons adjacent to the non-protonated carbons of the naphthalic ring and pyridine rings appear more downfield (8.18 - 8.57 ppm) in the spectrum.

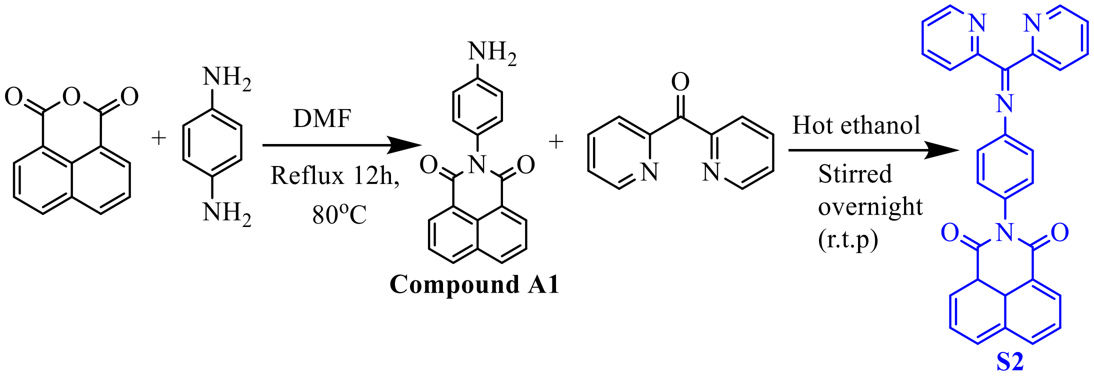

Scheme 1. Synthesis of 2-(4-((di(pyridin-2-yl)methylene)amino)phenyl)-1H-benzo[de]isoquinoline-1,3(2H)-dione (S2).

The IR spectrum of S2 (Figure 20) is characterized by C—H, C═C, C═N and C═O vibrational bands. The presence of multiple weak bands appearing in the 2995-2823 cm^{-1} region of the spectrum is assigned to the C—H vibrational stretching of the aromatic rings, whereas for the same aromatic rings in S2, the intense bands in the fingerprint region, 1238-521 cm^{-1}, due to aromatic C═C stretching is observed. More interestingly, the vibrational stretching band of moderate-intensity at 1589 cm^{-1} indicate the formation of C═N in the ligand. The most characteristic feature of S2 is the carbonyl oxygen which is represented by two bands in the IR spectrum. These characteristics confirm the presence of the C═O in the ligand as the anchoring group. The moderate band at higher wavenumber (1711 cm^{-1}) is due to the symmetric stretch of C═O, whereas the strong band at lower wavenumber (1661 cm^{-1}) is due to the asymmetric stretch of C═O. This symmetrical assignment of the C═O vibrational bands in diketones is clarified by [95] and is an agreement with [96,97], verifying that the symmetric stretch occurs at higher frequencies than the antisymmetric stretch in carbonyl vibrational stretches. In addition, the ab initio calculations also confirm that the in-phase (symmetric) vibrational stretching of C═O occurs at higher wavenumber and the out-of-phase (asymmetric) vibrational stretching occurs at lower wavenumber in the simulated spectra (Figure12 and Table 3).

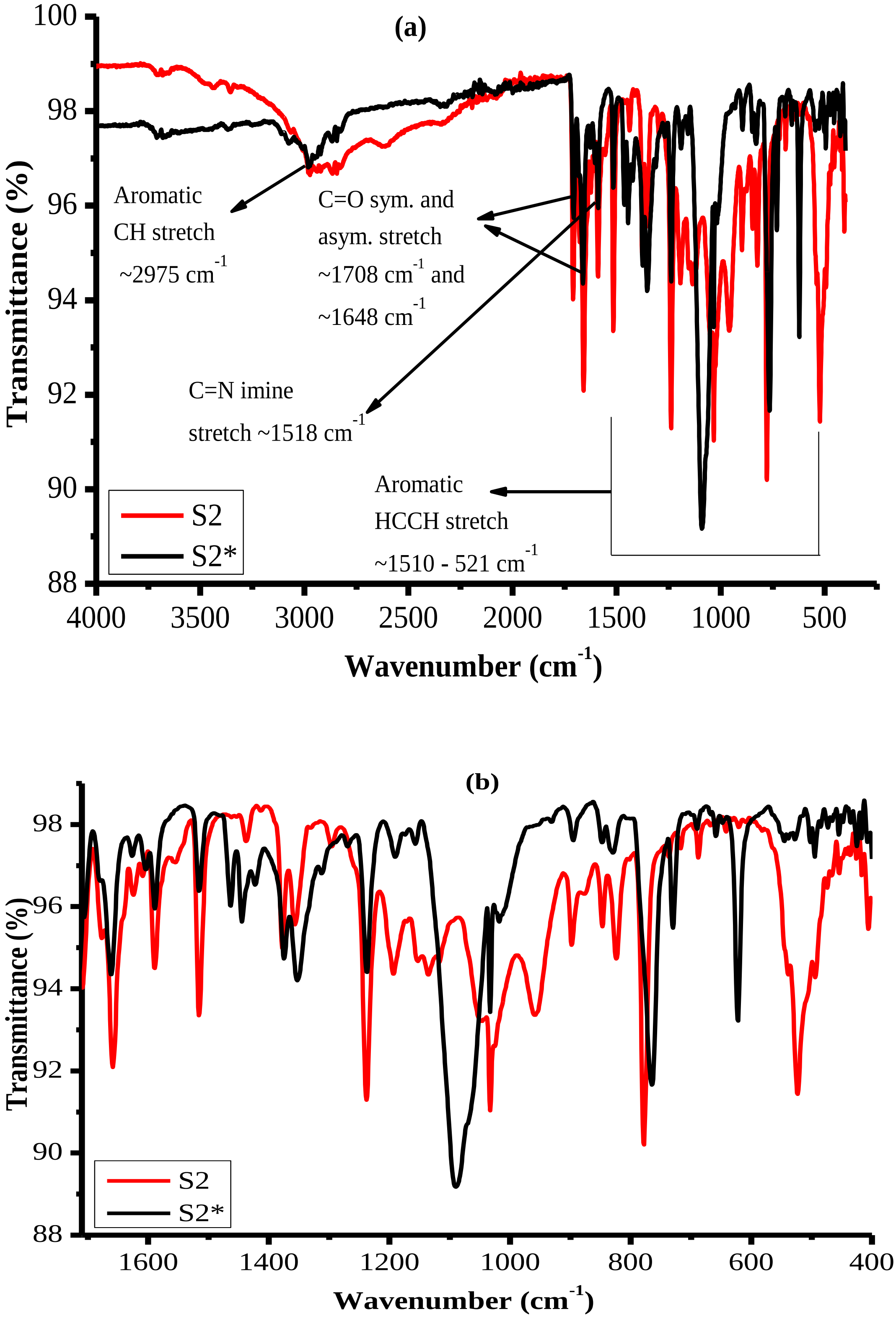

Figure 20. Experimental IR spectrum of S2 and S2*; (a) Full range spectra and (b) its fingerprint region (1700-400 cm^{-1}) of the IR spectra.

The UV-Vis spectrum of S2 (Figure 21) was characterized in acetonitrile and display absorption in the UV region ($\lambda < 400$ nm). Since the structure of S2 contains 1,8-naphthalic anhydride moiety as one of its starting materials, its UV-Vis spectrum contains features that are present in most of the absorption spectra of the reported 1,8-naphthalic anhydride derivatives [79–81]. The UV-Vis spectrum of S2 is characterized by two main distinct absorption bands at high energies and low energies, respectively. The distinctive band of S2 at $\lambda_{max} = 330$ nm with a broad shoulder band at $\lambda_{max} = 342$ nm is assigned to a low-energy band that is mainly attributed to the π - π^* transitions. The band at $\lambda_{max} = 330$ nm can be assigned as a π - π^* transition of the 1,8-naphthalic anhydride moiety, whereby the band at $\lambda_{max} = 342$ nm is attributed to the π - π^* intraligand charge transfer (ICT) transition between the phenyl ring and the pyridyl rings [79,82]. This assignment has also been confirmed by the TD-DFT results discussed previously in this section whereby the peak at the absorption maximum of 330 nm corresponds to a π transition that originates from the HOMO-1 to the LUMO and the peak at the absorption maximum of 342 nm correspond to π transition from the HOMO to the LUMO+1.

The most intense narrow absorption band at higher energy, $\lambda_{max} = 232$ nm, observed in the spectrum is also attributed to $\pi - \pi^*$ transition and has been confirmed computationally to correspond to H → L+8 excitation transition of the phenyl ring. In order to confirm the low energy $\pi - \pi^*$ transition bands at absorption maxima 330 nm and 342 nm in the spectrum of S2, solvatochromic studies in solvents of various polarities (hexane, tetrahydrofuran, acetonitrile and methanol) was carried out and results obtained showed that the two absorption bands are bathochromically shifted with increasing polarity (see Figure S7 of Appendix B).

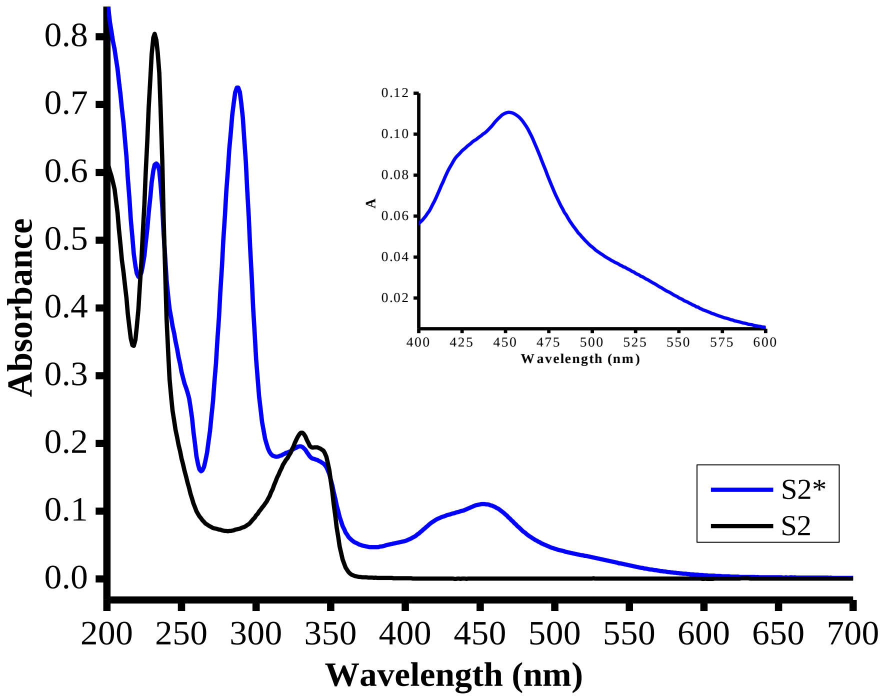

Figure 21. UV-Vis spectra of S2 and S2* in acetonitrile ($1x10^{-5}$ M).

4.4.2 Synthesis and characterization of S2*

The ruthenium dye complex, S2* (Scheme 2), was prepared by refluxing techniques of the reaction of aqueous $[Ru(bpy)_2(NO_3)_2]$ with S2 ligand in a 1:1 ratio. The resultant product was a reddish-brown powder of the desired ruthenium-based dye complex, $[Ru(bpy)_2S2](ClO_4)_2$ denoted as S2*. Further purification methods of S2* was done by recrystallizing the product in hot ethanol and the pure product was obtained as a red powder of S2* in petite yield. The resultant ^{1}H-NMR spectrum of S2* (Figure S6) shows not much of the difference from that of S2. However, the existence of singlet peaks and overlapping of some complex multiplets in the ^{1}H-NMR spectrum of S2* makes it difficult to successfully assign the protons of S2* dye complex. Similarly, the protons adjacent to the nitrogen atoms that are coordinated to ruthenium are allocated more downfield (8.27 - 8.69 ppm) in the spectrum.

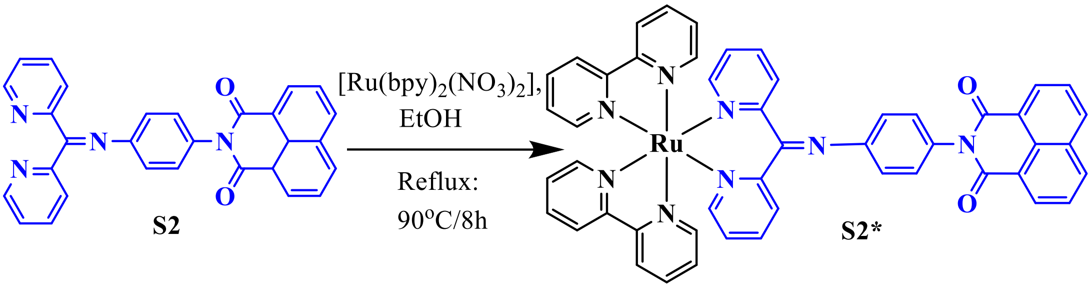

Scheme 2. Synthesis of $[Ru(bpy)_2S2](ClO_4)_2$ (S2*).

For structural identification, the IR spectrum of S2* dye complex was obtained and the assignment of functional groups present in the S2* dye was successfully done by the allocation of the vibrational energy bands present in the spectrum (Figure 20). Comparison studies were also implemented between the IR spectrum of S2 ligand and the IR spectrum of S2* dye complex. This was done in order to account for the change in vibration energy bands (i.e. frequencies, intensity, formation or disappearance of vibrational energy bands) between the two IR spectrum as well as to confirm the successful attachment of S2 to the dye complex, S2*. After careful analysis, it was observed that the spectral features of S2 and S2* are similar and the common functional groups (imine C═N and C═O) present in S2 were also observed in S2*. In the IR spectrum of S2*, the imine C═N vibrational stretching band appears less intense with a slight vibrational energy shift of 3 cm^{-1} towards lower energies. On the other hand, the symmetric and asymmetric vibrational energy band of the C═O stretching also appears to be slightly red-shifted with a reduction in their peak intensities compared to S2. Based on this analysis and observation made, it can, therefore, be concluded that S2 was successfully attached to S2*.

The photoresponsive properties of S2* were studied via its characterization through UV-Vis spectrophotometer. In Figure 21, the UV-Vis of the synthesized dye complex in acetonitrile is labelled as S2*. Observation from the UV-Vis spectrum of S2* shows that the dye complex displays the presence of all absorption peaks present in S2 with two new additional peaks at the absorption maxima of 287 nm and 452 nm. More importantly, the occurrence of the two distinct π - π* transition bands within the wavelength range of 292 – 368 nm in both spectra present the existence of the 1,8-naphthalic anhydride moiety in the starting material, S2, and in its coordinated metal dye complex, S2*.

The new absorption band at λ_{max} = 287 nm is due to the π - π* excitation transition of the bpy ligands on the ruthenium complex [45], while the broad absorption band in the visible range (λ_{max} = 452 nm) is generally ascribed to the MLCT, a characteristic exhibited by most metal-dye complexes [12,35,45] due to the transition between the d-orbital of ruthenium and π-electrons on the ligand (in this case S2). The molar extinction coefficient (ε) of S2* at λ_{max} = 452 nm, is 11,590 M^{-1} cm^{-1} which is lower than that of the N3 dye (14,000 M^{-1} cm^{-1} at λ_{max} = 535 nm) [12]. The value of ε for S2* is attributed by the lack of more π-conjugated moieties in S2 as a ligand and this can be improved by the addition of highly π-electron moieties in order to extend the conjugation of S2* [12,35]. This manipulation can have a positive impact on the absorption spectrum of S2* by promoting more light-harvesting of incident photons and therefore increasing the value of ε and overall, the power conversion efficiency of the cell. Consequently, the HOMO-LUOMO energy gap ($E_{H\text{-}L}$) of S2* due to the MLCT excitation band was estimated as 2.24 eV via the intersection wavelength of 553.89 nm between the normalized absorption spectra and emission spectra shown in Figure 22 below. This energy gap was estimated from the equation: $E_{H-L}/eV = 1240/\lambda\,(nm)$ whereby λ is the wavelength at the intersection point of the normalized spectra and at the same it is the photocurrent onset of S2*[98].

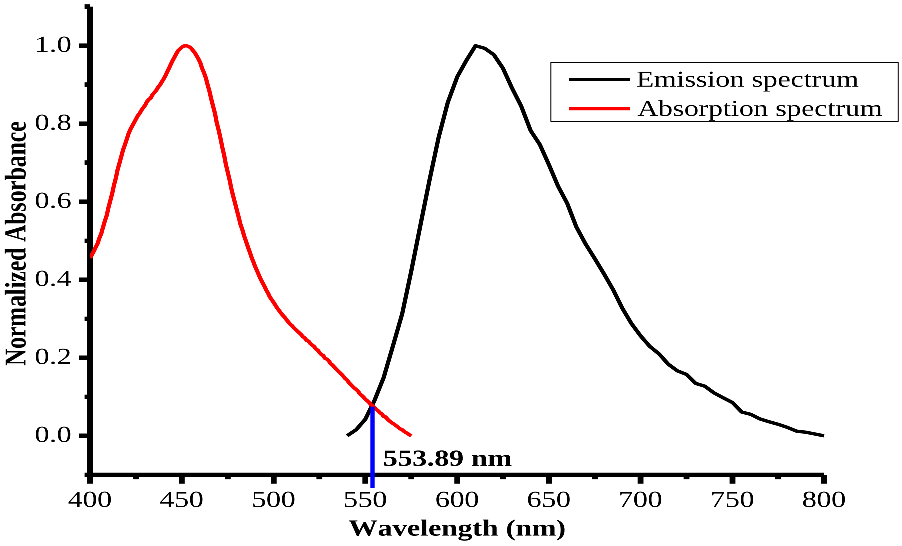

Figure 22. Normalized absorption and emission spectra of S2* in acetonitrile at a concentration of $1x10^{-5}$ M.

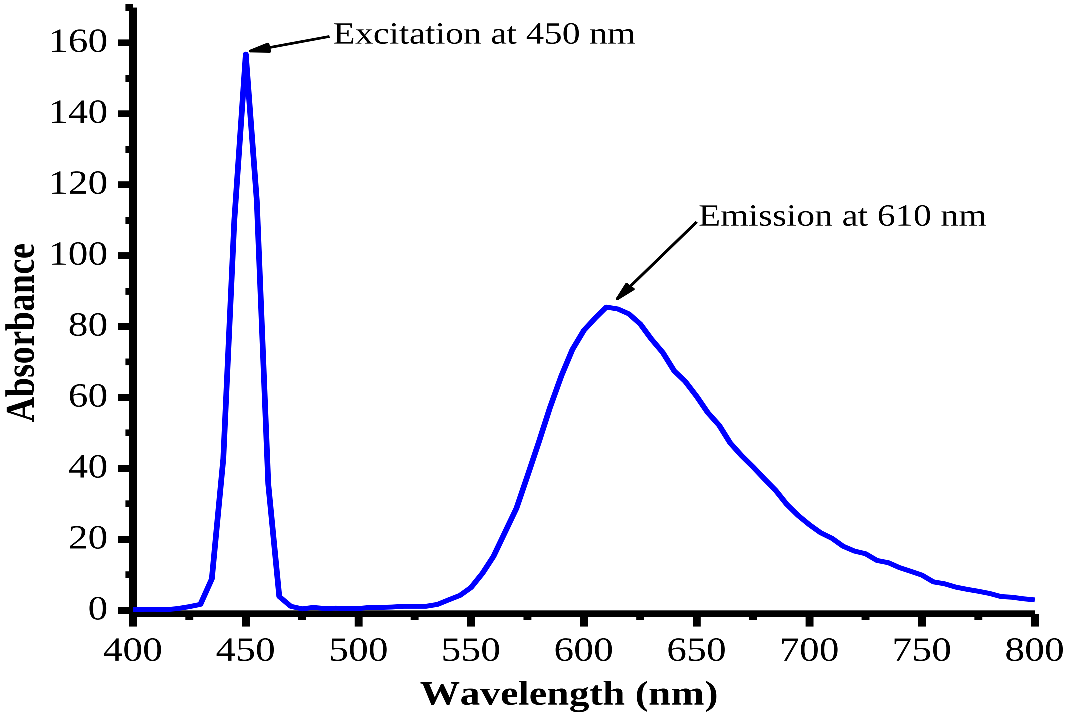

Figure 23. The emission spectrum of S2* in acetonitrile at a concentration of $1x10^{-5}$ M.

Several excitation wavelengths in the range 300 nm to 590 nm with an interval of 5 nm were selected to study the emission spectra of S2*. An excitation of 450 nm was then selected as the best excitation wavelength into the MLCT band for S2* because of its high emission intensity (Figure S9 of Appendix B) and its excitation into the visible region. Shown in Figure 23 is the emission spectrum of S2* in acetonitrile obtained at an excitation wavelength of 450 nm of the MLCT absorption band.

Generally, the absorption spectra only display the excitation of an electron to higher energy electronic states upon absorption of photon energy by that electron in a system. However, this process does not explain the behaviour of that electron once it reaches the excited state. Fluorescence spectroscopy enables one to understand the processes that occur at higher energy state at which an excited electron resides. An excited electron possesses higher potential energy and thus, usually very unstable in that energy state. In order for that electron to stabilize, its energy should be released in order to return to its stable ground energy state by a process called emission [99].

In this study, S2* was excited with a wavelength of 450 nm into its MLCT transition band and emitted a wavelength of 610 nm of an intense emission band observed at a longer wavelength (Figure 23). More noticeably, S2* exhibit a Stokes shift of 160 nm, which is in good agreement with the fluorescence spectra of the standard $[Ru(bpy)_3]^{2+}$ dye complex (Stokes shift of 155 nm) reported in [99] having an emission wavelength maximum of 610 nm and excitation wavelength of 455 nm. The Stokes shift ($\Delta\lambda$) is referred to as the difference in wavelength between the absorption maxima and emission maxima [100]. Generally, ruthenium polybipyridyl complexes exhibit a Stokes shift of up to $\Delta\lambda = 200\ nm$ [99]; a range in which a Stokes shift, $\Delta\lambda = 160\ nm$, of S2* is obtained.

4.4.3 Solvatochromic study of S2*

In order to study the solvent behaviour on the MLCT band of S2*, solvatochromism was carried out in various solvents of different polarities. The absorption spectra of S2* (Figure 24) was recorded in selected solvents ranging from the least polar solvent to the most polar solvent (hexane < tetrahydrofuran < acetonitrile < methanol) at a concentration of $1x10^{-5}$ M. The reported spectra only display a cut-off wavelength of range 400 – 700 nm in which the characterized band of the MLCT occur.

Solvatochromism depicts whether the solvent causes a shift in the spectrum (hypsochromically or bathochromically) or cause the intensity of the spectrum to either change hyperchromically or hypochromically [92,101,102]. In Table 12, a summarized study on the effect of the selected solvents on S2* is displayed, based on their absorption maxima and the intensities observed from the spectra. In both Table 12 and Figure 23, it is observed that the best solvent in terms of bathochromic shift (a shift to longer wavelength or red-shift) is tetrahydrofuran (λ_{max} = 564 nm) and the best solvent in terms of molar extinction coefficient (hyperchromic shift) is acetonitrile with an intensity of 0.1159 which is equivalent to 11,590 M^{-1} cm^{-1}. Therefore, in acetonitrile, S2* fairly offers a high degree of photon absorption within the functional range and in tetrahydrofuran, S2* slightly extends the functional range to the NIR region [12,35]. In terms of bathochromic shifts, the effects of these solvents on the position of the MLCT band of the UV-Vis spectra of S2* is in decreasing order of tetrahydrofuran > acetonitrile > methanol > hexane, while in terms of hyperchromic shift, the solvent effect on the intensity of the MLCT band of S2* follows a decreasing order of acetonitrile > methanol > tetrahydrofuran > hexane. In both cases, n-hexane has no significant effect on either the intensity or the band position on the absorption spectrum of S2* due to its low polarity and very low solubility in S2*.

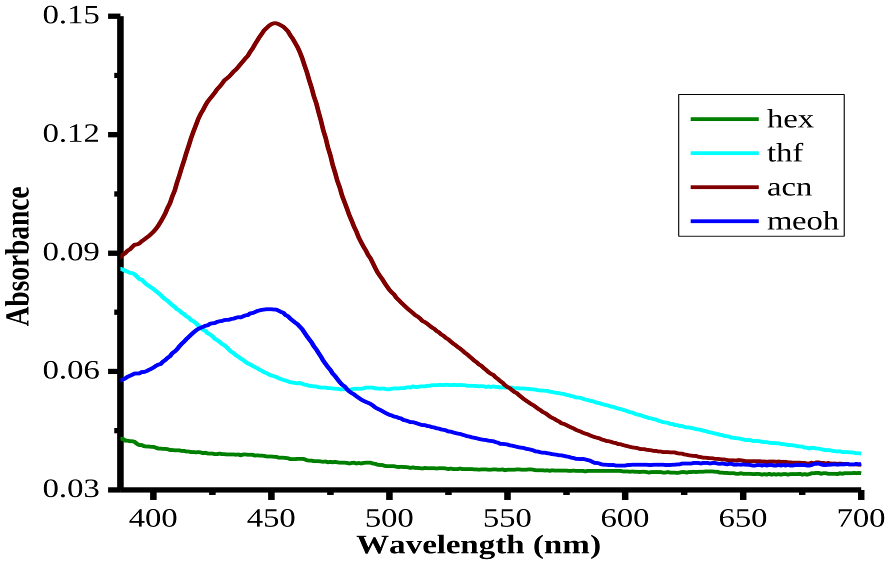

Figure 24. Absorption spectra of S2* in various solvents at 1x10^{-5} M.

Table 12. Various solvent effect on the MLCT absorption band of the UV-Vis spectra of S2*.

Solvent	λ_{max} (nm)	Intensity
Acetonitrile	452	0.1159
Methanol	448	0.08
Tetrahydrofuran	564	0.05
n-Hexane	____	____

4.4.4 UV-Vis titration: Redox properties of S2*

Redox properties of S2* were studied via UV-Vis titration of the dye complex with a strong oxidizing agent ceric ammonium nitrate ($(NH_4)_2Ce(NO_3)_6$) in a concentration of 3.0×10^{-2} M. Ceric ammonium nitrate, which is often abbreviated as CAN [75] is a strong oxidizing agent commonly used in the study of most metal dye complexes [35,75,103]. The UV-Vis titration was done in order to verify whether S2* can appear in mixed-valence states through the MLCT band. In this study, a UV-Vis spectrum of S2* in acetonitrile (1×10^{-5} M) was initially prepared and subsequently, 0.25 molar equivalent of Ce^{4+} was added and the spectrum was again recorded. This subsequent addition of 0.25 molar equivalent of Ce^{4+} to the dye solution and retaking of the UV-Vis spectrum at every molar equivalent interval was repeatedly done until a total of 2 molar equivalents of Ce^{4+} was added to the $[Ru(bpy)_2S2]^{2+}$ dye solution. The UV-Vis titration spectra of S2* is displayed in Figure 24 with an inset diagram giving a better visual of the point of inflection or isosbestic point for this UV-Vis titration.

At the wavelength of 440 nm an inflection point is clearly observed which separated the MLCT band into two regions: **A** ($\lambda \leq 440$ nm) and **B** ($\lambda \geq 440$ nm). Upon the molar equivalent addition of Ce^{4+}, the MLCT absorption band in region **A** increased in intensity while in region **B,** the MLCT absorption band decreased in intensity, an indication that ruthenium is oxidized to Ru^{3+} in region A while in region B, it is in its reduced form (Ru^{2+}). The inflection point referred to as an isosbestic point is a point that marks the existence of ruthenium in mixed-valence states (Ru^{2+}/Ru^{3+}) [35]. The redox properties obtained from the UV-Vis titration gives a redox couple of ruthenium (Ru^{2+}/Ru^{3+}), which represents the ground and excited states of S2*, respectively, upon photoionization.

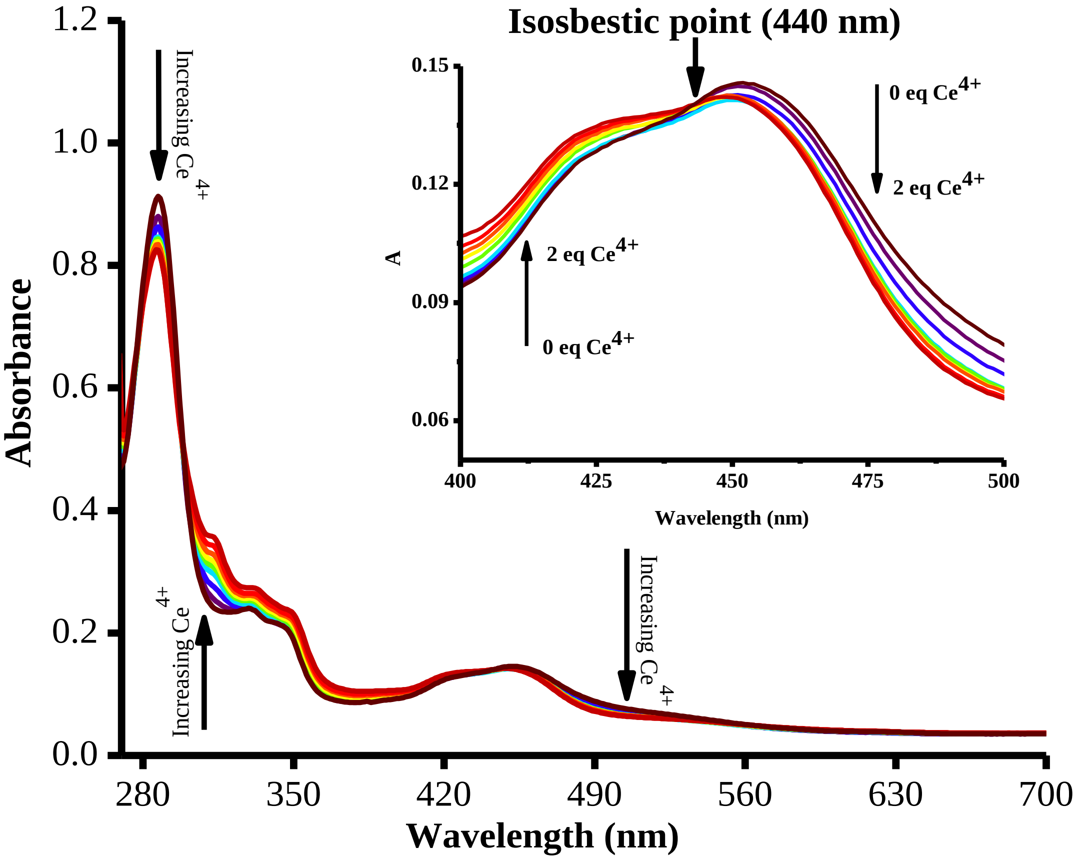

Figure 25. UV-Vis titration spectra of S2* with ($(NH_4)_2Ce(NO_3)_6$) in acetonitrile.

4.5 Comparison between Theory and Experiment

4.5.1 UV-Vis Spectra

Figures 25 and 26 show the normalized UV-Vis spectra of the designed potential ligand, S2, and its ruthenium-based dye sensitizer complex, S2*. In both figures, the UV-Vis absorption spectrum for S2 and S2* from experimental and theoretical approaches are compared. From the spectra of S2 (Figure 25), both the experimental and theoretical spectra show absorption bands within the UV region ($\lambda < 400$ nm) as well as the same spectral features, with the exception of two distinctive absorption bands (at $\lambda_{max} = 277.23$ nm and $\lambda_{max} = 305.88$ nm) that are only present in the computed spectrum. Additionally, the computed absorption bands appear red-shifted with higher intensity compared to the experimental UV bands, however, the difference in their absorption maxima is not more than 20 nm which makes them be in agreement with each other (Figure 25). Based on the previous discussions made in this section, the absorption bands for S2 were all assigned to $\pi - \pi^*$ transition bands both computationally and experimentally.

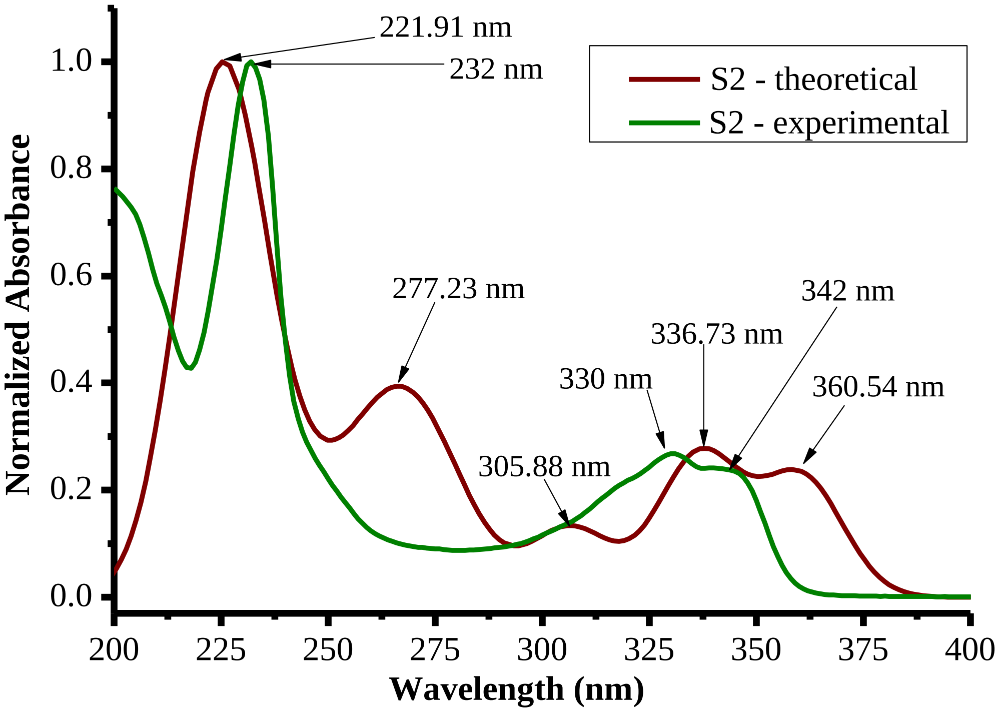

Figure 26. Normalized experimental and theoretical UV-Vis spectra of the designed ligands in acetonitrile.

For the S2* ruthenium-based dye complex, the visible MLCT absorption band was investigated theoretically and experimentally in the UV-Vis region (Figure 26). The MLCT transition band in both cases was compared with that of the computed UV-Vis spectrum of the standard $[Ru(bpy)_3]^{2+}$. This was done in order to account for any bathochromic shift or enhancement in the MLCT absorption band after substitution of one of the bpy ligands with S2 ligand to form S2*. From Figure 26, it is observed that the MLCT absorption band of S2* is significantly shifted to longer wavelengths in both theoretical and experimental UV-Vis spectra. The absence of the π(S2) – π*(S2) transition bands in the standard $[Ru(bpy)_3]^{2+}$ indicates successful attachment of S2 ligand in the dye complex, S2*, both theoretically and experimentally. These transitions have absorption maxima at λ_{max} = 339.12 nm and λ_{max} = 412.27 nm for the simulated S2* absorption spectra whereas for the experimental UV-Vis spectra, they are observed at λ_{max} = 328 nm and λ_{max} = 341 nm respectively.

Further comparisons also show that the MLCT band is observed at a longer wavelength (λ_{max} = 482.92 nm) in the simulated spectrum of S2* while the experimental MLCT absorption band occur at λ_{max} = 452 nm with a blue shift of 30.92 nm. These results can be said to be in good agreement with each other. In addition, the red-shifting in the MLCT absorption band of S2* from that of the standard $[Ru(bpy)_3]^{2+}$ (λ_{max} = 420.93 nm) signifies a great effect on the substitution of S2 with one of the bpy ligands in $[Ru(bpy)_3]^{2+}$. The H-L energy gap of S2* with respect to the MLCT transition band was calculated as 2.78 eV computationally and 2.24 eV experimentally. The best solvent selected in terms of photocatalytic enhancement is acetonitrile in both approaches, whereas in terms of extension of the functional range towards NIR, it is tetrahydrofuran (experimentally) and acetonitrile (computationally).

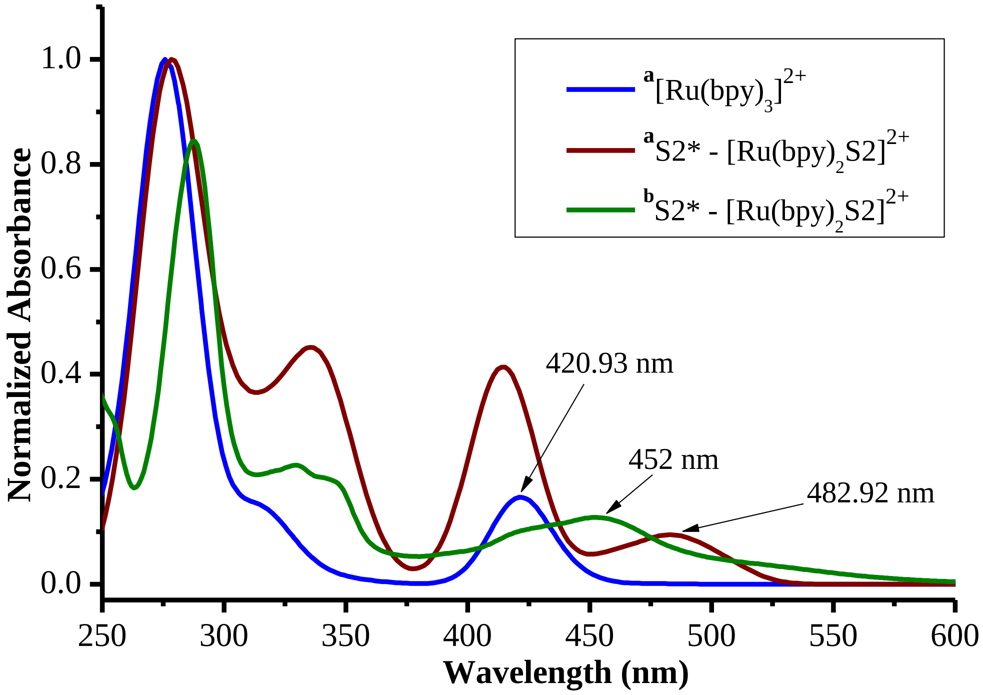

Figure 27. Normalized UV-Vis spectra of the designed dye complex in acetonitrile: a) obtained computationally and b) obtained experimentally.

4.5.2. IR Spectra

In order to compare the experimental IR spectrum of S2* to the theoretical IR spectrum, the simulated vibrational frequencies are often scaled by a factor of 0.89 - 0.95 [103]. This is due to the fact that the computed vibrational frequencies tend to produce higher estimate values compared to experiment. Therefore, scaling the harmonic vibrational frequencies brings the computed data to within a better agreement with the experimental data [103]. Table 13 shows compared vibrational frequencies of the assigned functional groups of S2* in both the computational (scaled by a factor of 0.95) and experimental approaches. Notably, the vibrational frequencies of the assigned functional groups in both the IR spectra are in good agreement and most experimental data falls within the scaled range of the computational data.

However, due to the congestion of the experimental IR spectrum, assignment of the experimental (Ru—N(S2)) vibrational mode was problematic. Scaling the simulated harmonic vibrational frequencies by 0.95 factor shows that the Ru—N(S2) vibrational energy band can be found within the range of approximately 983 – 574 cm^{-1} experimentally (Table 13).

Table 13. Comparison of vibrational frequencies of the computational and experimental IR spectra of S2*.

Vibrational bands	**Frequency range (cm^{-1})**	
	Theoretical scaled (0.95) values	**Experimental**
C—H (Aromatics stretching)	~3053	~2975
C═O (carbonyl stretching) sym. and asym.	~1695 - 1663	~1708 – 1648
C═N imine stretching	~1591	~1586
C=C (Aromatic rings - bending and stretching)	~1531 - 1128	~1510 – 521
Ru—N(bpy) Ru—N(S2)	~983 - 613	—

CHAPTER FIVE: CONCLUSIONS

This study combines both experimental and theoretical approach to design, synthesize and characterize a potential dye sensitizer (S2*) for use in DSSCs. First, a series of novel ruthenium-based dye sensitizers (S1* - S4*) were designed and the S2* dye complex was ultimately selected as a potential dye sensitizer on the basis of its photoresponse properties in the visible region. The results from the experimental and theoretical studies show that S2* displays a well distinct MLCT absorption band within the visible range of the electromagnetic spectrum. Absorption maxima of S2* at 483 nm (computationally) and 452 nm (experimentally) due to the MLCT transition were obtained. Compared to the computed excitation energy of S2*, the experimental MLCT absorption band is hypsochromically shifted to higher energies with a blue-shift of 30.92 nm. The TD-DFT studies indicate that the MLCT transition band belongs to excitation from HOMO-1 (d_{z^2}-orbital) on ruthenium to the LUMO which is a π-orbital primarily located on the S2 moiety of S2*.

The fluorescence properties of S2* investigated for its MLCT showed that at an excitation wavelength of 450 nm, the dye emitted light with absorbance maxima at 610 nm. The redox properties of S2* indicated that the dye can appear in mixed-valence states (Ru^{2+}/Ru^{3+}) upon which the dye complex changes its oxidation state through the process of photoionization and charge injection/ regeneration. This was confirmed by the presence of an isosbestic point at λ_{max} = 440 nm in the UV-Vis titration spectra of S2*.

In terms of solvatochromic studies, acetonitrile was selected as the best solvent based on photocatalytic enhancement (increasing the degree of photon absorption within the visible region) and tetrahydrofuran was chosen to be the best solvent which displayed an extension of the functional range towards the NIR. The presence of the symmetric and asymmetric C═O vibrational stretching bands in both the experimental and theoretical IR spectra of S2* indicated the presence of the S2 ligand in the S2* dye complex.

Finally, the results obtained from both the experimental and computational approach are in good agreement with each other. More importantly, based on the analysis made in this study, S2* is a potential candidate for the DSSCs because it exhibits remarkable photoresponse properties for both its λ_{max}, absorption range in the visible region and H-L energy gap.

CHAPTER SIX: RECOMMENDATIONS

Although S2* has remarkable photoresponse properties in the visible region, compared to the standard dye (i.e. N3 dye), the designed dye still offers room for improvement. Therefore, S2* should be re-engineered or modified in such a way that its π-conjugation system is extended. This can either increase its molar extinction coefficient or reduce its energy gap, allowing it to absorb photon energy in the NIR region of the UV-Vis spectrum. Furthermore, adsorption of S2* dye on TiO_2 should be carried out both experimentally and computationally in order to ensure that the dye can stick to the surface of TiO_2 and that it can efficiently inject electrons to the CB of TiO_2.

For structural identification of S2* dye, spectroscopic methods such as electrospray ionisation mass spectrometry (ESI-MS) and carbon-13 nuclear magnetic resonance (^{13}C-NMR) should also be employed in future studies. Additionally, it is recommended that different theoretical functionals of DFT or other computational methods be employed in similar studies. This will account for a better comparison between theoretical and experimental data as well as improvement in the computational error encountered with other methods. S2* should also be tested as a photocatalytic dye in the splitting of water activities for the evolution of H_2 gas which is used in fuel cells. Finally, in order to assess the efficiency of S2* as a novel dye, the construction of a solar cell device should be carried out.

CHAPTER SEVEN: REFERENCES

[1] World Energy Resources: 2013 Survey, World Energy Council, 2013. https://www.worldenergy.org/publications/2013/world-energy-resources-2013-survey/ (accessed August 21, 2019).

[2] M. Grätzel, Recent Advances in Sensitized Mesoscopic Solar Cells, 42 (2009) 1788–1798. doi:10.1021/ar900141y.

[3] M. Ye, X. Wen, M. Wang, J. Iocozzia, N. Zhang, C. Lin, Z. Lin, Recent advances in dye-sensitized solar cells : from photoanodes , sensitizers and electrolytes to counter electrodes, Biochem. Pharmacol. 18 (2015) 155–162. doi:10.1016/j.mattod.2014.09.001.

[4] E.S. Falsgraf, Biologically-Derived Dye-Sensitized Solar Cells: A Cleaner Alternative for Solar Energy, Pomona College, 2012. http://scholarship.claremont.edu/pomona_theses/61.

[5] S. Kohtani, M. Mori, E. Yoshioka, H. Miyabe, Photohydrogenation of Acetophenone Using Coumarin Dye-Sensitized Titanium Dioxide under Visible Light Irradiation, Catalysts. 5 (2015) 1417–1424. doi:10.3390/catal5031417.

[6] F.N.& J.U. William Ghann, Hyeonggon Kang, Tajbik Sheikh, Sunil Yadav, Tulio Chavez-Gil, Fabrication , Optimization and Characterization of Natural Dye Sensitized Solar Cell, Sci. Rep. 7 (2017) 41470. doi:10.1038/srep41470.

[7] L. Zhang, J.M. Cole, Anchoring Groups for Dye-Sensitized Solar Cells, ACS Appl. Mater. Interfaces. 7 (2015) 3427–3455. doi:10.1021/am507334m.

[8] S. Shalini, R. Balasundaraprabhu, T.S. Kumar, N. Prabavathy, S. Senthilarasu,

S. Prasanna, Status and outlook of sensitizers/dyes used in dye sensitized solar cells (DSSC): a review, Int. J. Energy Res. 40 (2016) 1303–1320. doi:10.1002/er.3538.

[9] B. Cerda, R. Sivakumar, M. Paulraj, Natural dyes as sensitizers to increase the efficiency in sensitized solar cells, J. Phys. Conf. Ser. 720 (2016) 012030. IOP Publishing. doi:10.1088/1742-6596/720/1/012030.

[10] B. Basheer, D. Mathew, B.K. George, C.P.R. Nair, An overview on the spectrum of sensitizers: the heart of dye sensitized solar cells, Sol. Energy. 108 (2014) 479–507. doi:10.1016/j.solener.2014.08.002.

[11] N. Rawal, A.G. Vaishaly, H. Sharma, B.B. Mathew, Dye sensitized solar cells: The emerging technology, Energy Power Eng. Serv. 2 (2015) 46–52. doi:10.12966/epes.05.03.2015.

[12] M. Ryan, PGM HIGHLIGHTS: Progress in Ruthenium Complexes for Dye Sensitised Solar Cells, Platin. Met. Rev. 53 (2009) 216–218. doi:10.1595/147106709X475315.

[13] M.K. Nazeeruddin, F. De Angelis, S. Fantacci, A. Selloni, G. Viscardi, P. Liska, S. Ito, B. Takeru, M. Grätzel, Combined experimental and DFT-TDDFT computational study of photoelectrochemical cell ruthenium sensitizers, J. Am. Chem. Soc. 127 (2005) 16835–16847. doi:10.1021/ja052467l.

[14] M.A. Green, Y. Hishikawa, E.D. Dunlop, D.H. Levi, J. Hohl-Ebinger, A.W.Y. Ho-Baillie, Solar cell efficiency tables (version 51), Prog. Photovoltaics Res. Appl. 26 (2018) 3–12. doi:10.1002/pip.2978.

[15] M. Kasemann, K. Rühle, L.M. Reindl, Photovoltaic Energy Harvesting under

Low Lighting Conditions, Proc. Sens. 2013. (2013) 483–485. doi:10.5162/sensor2013/C8.3.

[16] P. Hastings, The Illustrated Guide to Electrical Building Services, Second edi, BSRIA, 2005.

[17] L. El Chaar, L.A. Lamont, N. El Zein, Review of photovoltaic technologies, 15 (2011) 2165–2175. doi:10.1016/j.rser.2011.01.004.

[18] M.T. Kibria, A. Ahammed, S.M. Sony, F. Hossain, Shams-Ul-Islam, A Review: Comparative studies on different generation solar cells technology, Proc. 5th Int. Conf. Environ. Asp. Bangladesh. (2014) 51–53.

[19] S.H. Poder, Potentials and challenges of facade mounted PV in urban areas – with Copenhagen International School as case, Technical University of Denmark, 2018.

[20] N.A. Ludin, A.M.A. Mahmoud, A.B. Mohamad, A.A.H. Kadhum, K. Sopian, N.S.A. Karim, Review on the development of natural dye photosensitizer for dye-sensitized solar cells, Renew. Sustain. Energy Rev. 31 (2014) 386–396. doi:10.1016/j.rser.2013.12.001.

[21] S. Mozaffaria, M.R. Nateghib, M.B. Zarandi, An overview of the Challenges in the commercialization of dye sensitized solar cells, Renew. Sustain. Energy Rev. 71 (2017) 675–686. doi:10.1016/j.rser.2016.12.096.

[22] S. Sharma, B. Siwach, S.K. Ghoshal, D. Mohan, Dye sensitized solar cells: From genesis to recent drifts, Renew. Sustain. Energy Rev. 70 (2017) 529–537. doi:10.1016/j.rser.2016.11.136.

[23] G. Richhariya, A. Kumar, P. Tekasakul, B. Gupta, Natural dyes for dye

sensitized solar cell: A review, Renew. Sustain. Energy Rev. 69 (2017) 705–718. doi:10.1016/j.rser.2016.11.198.

[24] M. Gul, Y. Kotak, T. Muneer, Review on recent trend of solar photovoltaic technology, Energy Explor. Exploit. 34 (2016) 485–526. doi:10.1177/0144598716650552.

[25] M.G. Walter, A.B. Rudine, C.C. Wamser, Porphyrins and phthalocyanines in solar photovoltaic cells, J. Porphyr. Phthalocyanines. 14 (2010) 759–792. doi:10.1142/S1088424610002689.

[26] M.K. Nazeeruddin, A. Kay, I. Rodicio, R. Humphry-Baker, E. Müller, P. Liska, N. Vlachopoulos, M. Grätzel, Conversion of light to electricity by cis-X2bis (2, 2'-bipyridyl-4, 4'-dicarboxylate) ruthenium (II) charge-transfer sensitizers (X= Cl^-, Br^-, I^-, CN^-, and SCN^-) on nanocrystalline titanium dioxide electrodes, 115 (1993) 6382–6390. doi:10.1021/ja00067a063.

[27] S. Zhang, X. Yang, Y. Numata, L. Han, Highly efficient dye-sensitized solar cells: progress and future challenges, Energy Environ. Sci. 6 (2013) 1443–1464. doi:10.1039/c3ee24453a.

[28] A. Fattori, Electrochemical and Spectroelectrochemical Studies of Dyes used in Dye-sensitized Solar Cells, University of Bath, 2010.

[29] G.M. Shoro, D.M.A. Hussain, D. Sera, Photovoltaic System in Progress: A Survey of Recent Development, in: InInternational Multi Top. Conf., Springer International Publishing Switzerland, 2014: pp. 239–250. doi:10.1007/978-3-319-10987-9_22.

[30] J. Cosgrove, Dyesol Limited, Solar technology in development, Wilson HTM

Investment Group, (2009). http://www.greatcellsolar.com/investors/analyst-reports/ (accessed August 21, 2019).

[31] J. Gong, J. Liang, K. Sumathy, Review on dye-sensitized solar cells (DSSCs): Fundamental concepts and novel materials, Renew. Sustain. Energy Rev. 16 (2012) 5848–5860. doi:10.1016/j.rser.2012.04.044.

[32] S. Ito, Investigation of dyes for dye-sensitized solar cells: Ruthenium-complex dyes, metal-free dyes, metal-complex porphyrin dyes and natural dyes. Solar Cells-Dye-Sensitized Devices, Sol. Cells-Dye-Sensitized Devices. (2011) 19–48.

[33] E. Tasal, E. Gungor, T. Gungor, Study in the Solvent Polarity Effects on Solvatochromic Behaviour of Pomiferin, Phys. Chem. 6 (2016) 33–38. doi:10.5923/j.pc.20160602.01.

[34] L. Muthaiyan, S. Sriram, B.G. Jeyaprakash, D. Balamurugan, Combined experimental and DFT/TDDFT study of berry dye chelated TiO_2 for dssc applications, Rasayan J. Chem. 10 (2017) 1417–1423.

[35] U. Veikko, X. Zhang, T. Peng, P. Cai, G. Cheng, The synthesis and characterization of dinuclear ruthenium sensitizers and their applications in photocatalytic hydrogen production, Spectrochim. ACTA PART A Mol. Biomol. Spectrosc. 105 (2013) 539–544. doi:10.1016/j.saa.2012.12.061.

[36] H. Desilvestro, Y. Hebting, Ruthenium-based dyes for Dye- sensitized Solar Cells, Sigma-Aldrich Anal. Biol. Chem. Mater. Sci. Prod. Serv. 2 (2011). https://www.sigmaaldrich.com/technical-documents/articles/materials-science/organic-electronics/dye-solar-cells.html (accessed August 21, 2019).

[37] A.O. Adeloye, P.A. Ajibade, Towards the Development of Functionalized PolypyridineLigands for Ru (II) Complexes as Photosensitizers in Dye-Sensitized Solar Cells (DSSCs), Molecules. 19 (2014) 12421–12460. doi:10.3390/molecules190812421.

[38] A. Islam, F.A. Chowdhury, Y. Chiba, R. Komiya, N. Fuke, N. Ikeda, K. Nozaki, L. Han, Synthesis and characterization of new efficient tricarboxyterpyridyl (β-diketonato) ruthenium (II) sensitizers and their applications in dye-sensitized solar cells, Chem. Mater. 18 (2006) 5178–5185. doi:10.1021/cm0602141.

[39] S. PM, J. K, R. RA, A. S, Synthesis, characterization and solvatochromic spectra of novel thiazole based azo dye, Der Chem. Sin. 4 (2013) 49–54.

[40] K.E. Jasim, Dye sensitized solar cells-working principles, challenges and opportunities, in: Sol. Cells-Dye-Sensitized Devices, 2011: pp. 172–204.

[41] K.L. Mccall, Novel Ruthenium Complexes and their Application in Dye Sensitised Solar Cells, PhD [dissertation], The University of Edinburgh, 2008. https://era.ed.ac.uk/handle/1842/4346.

[42] R.K. Chitumalla, K.S.V. Gupta, C. Malapaka, R. Fallahpour, A. Islam, L. Han, B. Kotamarthi, S.P. Singh, Thiocyanate-free cyclometalated ruthenium (II) sensitizers for DSSC: a combined experimental and theoretical investigation, Phys. Chem. Chem. Phys. 16 (2014) 2630–2640. doi:10.1039/c3cp53613k.

[43] K. Liu, C. Hsu, S. Chang, J. Chen, K. Ho, K. Lin, Synthesis and Characterization of Cross-Linkable Ruthenium Complex Dye and Its Application on Dye-Sensitized Solar Cells, J. Polym. Sci. Part A Polym. Chem. 48 (2010) 366–372. doi:10.1002/pola.23793.

[44] K. Liu, C. Ko, K. Ho, K. Lin, Synthesis and characterization of cross-linkable ruthenium dye with ion coordinating property for dye-sensitized solar cells, Polymer (Guildf). 52 (2011) 3318–3324. doi:10.1016/j.polymer.2011.05.035.

[45] H.M. Nguyen, D.N. Nguyen, N. Kim, Improved performance of dye-sensitized solar cells by tuning the properties of ruthenium complexes containing conjugated bipyridine ligands, Adv. Nat. Sci. Nanosci. Nanotechnol. 1 (2010) 025001. doi:10.1088/2043-6254/1/2/025001.

[46] Y. Yamaguchi, S.S. Pandey, N. Fujikawa, Y. Ogomi, S. Hayase, A Combined Theoretical and Experimental Approaches Towards Designing NIR Dyes for Dye-Sensitized Solar Cells, J. Eng. Sci. Technol. Spec. (2014) 51–65.

[47] S. Fantacci, F. De Angelis, J. Wang, S. Bernhard, A. Selloni, D. Chimica, V. Uni, V. Elce, A Combined Computational and Experimental Study of Polynuclear Ru− TPPZ Complexes: Insight into the Electronic and Optical Properties of Coordination Polymers, J. Am. Chem. Soc. 126 (2004) 9715–9723. doi:10.1021/ja048421u.

[48] C. Barolo, M.K. Nazeeruddin, S. Fantacci, D. Di Censo, P. Comte, P. Liska, G. Viscardi, P. Quagliotto, F. De Angelis, S. Ito, M. Gra1tzel, Synthesis, characterization, and DFT-TDDFT computational study of a ruthenium complex containing a functionalized tetradentate ligand, Inorg. Chem. 45 (2006) 4642–4653. doi:10.1021/ic051970w.

[49] S. Das, S. Karmakar, D. Saha, S. Baitalik, A combined experimental and DFT/TD-DFT investigation of structural, electronic, and cation-induced switching of photophysical properties of bimetallic Ru (II) and Os (II) complexes derived from imidazole-4, 5-dicarboxylic acid and 2, 2′-bipyridine,

Inorg. Chem. 52 (2013) 6860–6879. doi:10.1021/ic302566p.

[50] C. Sun, Y. Li, P. Song, F. Ma, An experimental and theoretical investigation of the electronic structures and photoelectrical properties of ethyl red and carminic acid for DSSC application, Materials (Basel). 9 (2016) 813. doi:10.3390/ma9100813.

[51] J.-F. Guillemoles, V. Barone, L. Joubert, C. Adamo, A theoretical investigation of the ground and excited states of selected Ru and Os polypyridyl molecular dyes, J. Phys. Chem. A. 106 (2002) 11354–11360. doi:10.1021/jp021517v.

[52] M. Pastore, First principle modelling of materials and processes in dye-sensitized photoanodes for solar energy and solar fuels, Computation. 5 (2017) 5. doi:10.3390/computation5010005.

[53] S.B. Novir, S.M. Hashemianzadeh, Density functional theory study of new azo dyes with different π-spacers for dye-sensitized solar cells, Spectrochim. ACTA PART A Mol. Biomol. Spectrosc. 143 (2015) 20–34. doi:10.1016/j.saa.2015.02.026.

[54] D.C. Young, Computational chemistry: A practical guide for applying techniques to real world problems, John Wiley & Sons, Inc, New York, 2001.

[55] F. Jensen, Introduction to Computational Chemistry, Second Edi, John Wiley & Sons Ltd, Chichester, 2007.

[56] F. Gao, Y. Wang, D. Shi, J. Zhang, M. Wang, X. Jing, R. Humphry-baker, P. Wang, S.M. Zakeeruddin, M. Grätzel, Enhance the optical absorptivity of nanocrystalline TiO_2 film with high molar extinction coefficient ruthenium sensitizers for high performance dye-sensitized solar cells, J. Am. Chem. Soc.

130 (2008) 10720–10728. doi:10.1021/ja801942j.

[57] J. Dervaux, P. Cormier, C. Struzzi, M. Scardamaglia, C. Bittencourt, L. Petaccia, D. Cornil, L. Lasser, J. Cornil, R. Lazzaroni, R. Snyders, Probing the interaction between 2, 2′-bithiophene-5-carboxylic acid and TiO_2 by photoelectron spectroscopy: A joint experimental and theoretical study, J. Chem. Phys. 147 (2017) 244704. doi:10.1063/1.5008800.

[58] L.A. Fredin, T.C. Allison, Predicting Structures of Ru – Centered Dyes: A Computational Screening Tool, J. Phys. Chem. A. 120 (2016) 2135–2143. doi:10.1021/acs.jpca.6b00921.

[59] B. Ma, Y. Peng, T. Tao, J. Geng, W. Huang, Ruthenium sensitizers with various 2-thiophenimidazo [4, 5-f][1,10] phenanthroline based ancillary ligands and their performance for dye-sensitized solar cells, Dye. Pigment. 117 (2015) 100–107. doi:10.1016/j.dyepig.2015.02.008.

[60] N. Martsinovich, A. Troisi, Theoretical studies of dye-sensitised solar cells: from electronic structure to elementary processes, Energy Environ. Sci. 4 (2011) 4473–4495. doi:10.1039/c1ee01906f.

[61] A.A. Hasanein, Y.R. Elmarassi, B.A. Ali, TD-DFT study of charge transfer excitation in D-π-A metal complex dyes as sensitizers in DSSCs, J. Comput. Methods Mol. Des. 5 (2015) 109–119.

[62] J. Chen, F. Bai, J. Wang, L. Hao, Z. Xie, Q. Pan, H. Zhang, Theoretical studies on spectroscopic properties of ruthenium sensitizers absorbed to TiO_2 film surface with connection mode for DSSC, Dye. Pigment. 94 (2012) 459–468. doi:10.1016/j.dyepig.2012.01.018.

[63] S. Boumendil, J. Cornard, M. Sekkal-rahal, A. Moncomble, Solvent effects to compute UV–vis spectra for ionic metal complexes, Chem. Phys. Lett. 636 (2015) 39–45. doi:10.1016/j.cplett.2015.07.019.

[64] C.D.D. Sundari, M.A. Martoprawiro, A.L. Ivansyah, A DFT and TDDFT study of PCM effect on N3 dye absorption in ethanol solution, InJournal Phys. Conf. Ser. 812 (2017) 012068. IOP Publishing. doi:10.1088/1742-6596/812/1/012068.

[65] A.A. Bhuiyan, S. Kudo, J. Bartlett, Synthesis and characterization of ruthenium complexes containing chlorophenanthroline and bipyridine, J. Ark. Acad. Sci. 64 (2010) 33–40.

[66] M.H. M. J. Frisch, G. W. Trucks, H. B. Schlegel, G. E. Scuseria, M. A. Robb, J. R. Cheeseman, G. Scalmani, V. Barone, B. Mennucci, G. A. Petersson, H. Nakatsuji, M. Caricato, X. Li, H. P. Hratchian, A. F. Izmaylov, J. Bloino, G. Zheng, J. L. Sonnenberg, D.J. Fox, GAUSSIAN 09, (2009).

[67] A. Saini, A.K.K. Bhasin, N. Singh, N. Kaur, Development of a Cr (III) ion selective fluorescence probe using organic nanoparticles and its real time applicability, New J. Chem. 40 (2015) 278–284. doi:10.1039/C5NJ01843A.

[68] Z. Li, Y. Zhou, K. Yin, Z. Yu, Y. Li, J. Ren, A new fluorescence “turn-on” type chemosensor for Fe^{3+} based on naphthalimide and coumarin, Dye. Pigment. 105 (2014) 7–11. doi:10.1016/j.dyepig.2013.12.032.

[69] Z. Arifin, S. Soeparman, D. Widhiyanuriyawan, S. Suyitno, Performance Enhancement of Dye-Sensitized Solar Cells Using a Natural Sensitizer, Int. J. OfPhotoenergy Absorbance. 2017 (2017). doi:10.1155/2017/2704864.

[70] A.A. Soliman, M.A. Amin, A.A. El-sherif, C. Sahin, C. Varlikli, Synthesis, characterization and molecular modeling of new ruthenium (II) complexes with nitrogen and nitrogenoxygen donor ligands, Arab. J. Chem. 10 (2017) 389–397. doi:10.1016/j.arabjc.2015.04.001.

[71] E.B. Ituen, I.J. Akpan, O.R. Oluwaseyi, Molecular structure, chemical reactivity, stability and vibrational spectroscopic investigation of stearic and palmitic acid using density functional theory, IOSR J. Appl. Chem. 7 (2014) 8–12.

[72] A. Bendjeddou, T. Abbaz, A.K. Gouasmia, D. Villemin, Molecular structure, HOMO-LUMO, MEP and Fukui function analysis of some TTF-donor substituted molecules using DFT (B3LYP) calculations, Int. Res. J. Pure Appl. Chem. 12 (2016) 1–9. doi:10.9734/IRJPAC/2016/27066.

[73] P. Wałejko, Ł. Dobrzycki, A. Ratkiewicz, P. Socha, S. Witkowski, M.K. Cyrański, An X-ray and Natural Bond Orbital (NBO) structural study of α-tocopheryl and 2,2,5,7,8-pentamethylchroman-6-yl succinates, J. Saudi Chem. Soc. 23 (2018) 365–377. doi:10.1016/j.jscs.2018.08.010.

[74] G.L. Eakins, J.S. Alford, B.J. Tiegs, B.E. Breyfogle, C.J. Stearman, Tuning HOMO–LUMO levels: trends leading to the design of 9-fluorenone scaffolds with predictable electronic and optoelectronic properties, J. Phys. Org. Chem. 24 (2011) 1119–1128. doi:10.1002/poc.1864.

[75] A.D. Basner, Synthesis of heteroaromatic ruthenium dyes for use as electron reservoirs in dye-sensitized solar cells, PhD [dissertation], Syracuse University, 2017. https://surface.syr.edu/etd/738.

[76] A. Garza-ortiz, P.U. Maheswari, M. Siegler, A.L. Spek, J. Reedijk, A new

family of Ru(II) complexes with a tridentate pyridine Schiff-base ligand and bidentate co-ligands: Synthesis, characterization, structure and in vitro cytotoxicity studies, New J. Chem. 37 (2013) 3450–3460. doi:10.1039/C3NJ00415E.

[77] OriginLab© Corporation. OriginPro 8 SR4, (2008). http://www.originlab.com/.

[78] A.H. Mekky, H.G. Elhaes, M.M. El-Okr, A.S. Al-Aboodi, M.A. Ibrahim, Effect of Solvents on the Electronic Properties of Fullerene Based Systems: Molecular Modelling, Appl. Comput. Math. 4 (2015) 1000203. doi:10.4172/2168-9679.1000203.

[79] S. Sánchez, A.Y.Y. Wo, T. Baumgartner, Electron-accepting π-conjugated species with 1,8-naphthalic anhydride or diketophosphanyl units, Mater. Chem. Front. 1 (2017) 2324–2334. doi:10.1039/c7qm00336f.

[80] M. Soni, S.K. Das, P.K. Sahu, U.P. Kar, A. Rahaman, M. Sarkar, Synthesis, photophysics, live cell imaging, and aggregation behavior of some structurally similar alkyl chain containing bromonaphthalimide systems: Influence of alkyl chain length on the aggregation behavior, J. Phys. Chem. C. 117 (2013) 14338–14347. doi:10.1021/jp403409d.

[81] M.S. Alexiou, V. Tychopoulos, S. Ghorbanian, J.H.P. Tyman, R.G. Brown, P. 1. Brittain, The UV–Visible absorption and fluorescence of some substituted 1,8-naphthalimides and naphthalic anhydrides, J. Chem. Soc. Perkin Trans. 2. 5 (1990) 837–842. doi:10.1039/P29900000837.

[82] L. Wang, Y. Shi, Y. Zhao, H. Liu, X. Li, M. Bai, “Push–pull” 1,8-naphthalic anhydride with multiple triphenylamine groups as electron donor, J. Mol. Struct. 1057 (2014) 339–346. doi:10.1016/j.molstruc.2013.10.004.

[83] J.-J. Lee, M.M. Rahman, S. Sarker, N.C.D. Nath, A.J.S. Ahammad, J.K. Lee, Metal oxides and their composites for the photoelectrode of dye sensitized solar cells, in: Adv. Compos. Mater. Med. Nanotechnol., InTech, Rijeka, Croatia, 2011: pp. 181–210. doi:10.5772/15280.

[84] M.S. Ahmad, N.A. Rahim, A.K. Pandey, Improved electron transfer of TiO_2 based dye sensitized solar cells using Ge as sintering aid, Optik (Stuttg). 157 (2018) 134–140. doi:10.1016/j.ijleo.2017.11.073.

[85] G. Zhang, C.B. Musgrave, Comparison of DFT methods for molecular orbital eigenvalue calculations, J. Phys. Chem. A. 111 (2007) 1554–1561. doi:10.1021/jp061633o.

[86] J. Fujisawa, T. Eda, M. Hanaya, Comparative study of conduction-band and valence-band edges of TiO_2, $SrTiO_3$, and $BaTiO_3$ by ionization potential measurements, Chem. Phys. Lett. 685 (2017) 23–26. doi:10.1016/j.cplett.2017.07.031.

[87] M.I. Khan, A Study on the Optimization of Dye-Sensitized Solar Cells, MSc [thesis], University of South Florida, 2013. doi:10.13140/RG.2.1.2291.4801.

[88] E. V. Verbitskiy, P.A. Slepukhin, Y.O. Subbotina, M.S. Valova, A. V. Schepochkin, E.M. Cheprakova, G.L. Rusinov, V.N. Charushin, 2-amino-5-aryl-and 2-amino-5-hetaryl-3-cyano-6-(2-thienyl) pyridines as organic dyes for dye-sensitized solar cells: Synthesis, quantum-chemical calculations, spectral and electrochemical properties, Chem. Heterocycl. Compd. 50 (2014) 883–896. doi:10.1007/s10593-014-1536-x.

[89] J.K. Roy, S. Kar, J. Leszczynski, Insight into the optoelectronic properties of designed solar cells efficient tetrahydroquinoline dye-sensitizers on $TiO_2(101)$

surface: first principles approach, Sci. Rep. 8 (2018) 10997. doi:10.1038/s41598-018-29368-9.

[90] T. Funaki, H. Otsuka, N. Onozawa-komatsuzaki, K. Kasuga, K. Sayama, H. Sugihara, Systematic evaluation of HOMO energy levels for efficient dye regeneration in dye-sensitized solar cells, J. Mater. Chem. A. 2 (2014) 15945–15951. doi:10.1039/c4ta00613e.

[91] M.S. ZAKERHAMIDI, A. GHANADZADEH., M. MOGHADAM, Solvent effects on the UV/visible absorption spectra of some aminoazobenzene dyes, Chem. Sci. Trans. 1 (2012) 1–8. doi:10.7598/cst2012.118.

[92] G. George, Photochemical and photophysical studies of a few bischromophoric systems, Conchin University of Science & Technology, 2010.

[93] A.-R. Allouche, Gabedit - A graphical user interface for computational chemistry softwares, J. Comput. Chem. 32 (2011) 174–182. http://gabedit.sourceforge.net.

[94] N. Shibayam, H. Ozawa, M. Abe, Y. Ooyamac, H. Arakawa, A new cosensitization method using the Lewis acid sites of a TiO_2 photoelectrode for dye-sensitized solar cells, Chem. Commun. 50 (2014) 6398–6401. doi:10.1039/c3cc49461f.

[95] F. Miller, F. Kiviat, I. Matsubara, The infrared and Raman spectra of cyclobutane-1,3-dione, Spectrochim. Acta Part A Mol. Spectrosc. 24 (1968) 1523–1526. doi:10.1016/0584-8539(68)80176-X.

[96] R. Aroca, S. Corrent, J.R. Menendez, Vibrational spectra and structure of 1,8-naphthalic anhydride, Vib. Spectrosc. 13 (1997) 221–226. doi:10.1016/S0924-

2031(96)00052-5.

[97] B. Smith, Infrared spectral interpretation: a systematic approach, CRC Press, London New York Washington, D.C., 1999.

[98] X. Zhang, U. Veikko, J. Mao, P. Cai, T. Peng, Visible-Light-Induced Photocatalytic Hydrogen Production over Binuclear RuII–Bipyridyl Dye-Sensitized TiO_2 without Noble Metal Loading, Chem. Eur. J. 18 (2012) 12103–12111. doi:10.1002/chem.201200725.

[99] Z.J. Stack, The synthesis and characterisation of novel Ruthenium(II)polypyridyl complexes for use in cellular imaging, MSc [thesis], Dublin City University, 2013. http://doras.dcu.ie/19181/.

[100] D. Avcı, S. Altürk, Ö. Tamer, M. Kuşbazoğlu, Y. Atalay, Solvent effect in implicit/explicit model on FT–IR, ^{1}H, ^{13}C and ^{19}F NMR, UV–vis and fluorescence spectra, linear, second–and third–nonlinear optical parameters of 2–(trifluoromethyl)benzoic acid: Experimental and computational study, J. Mol. Struct. 1143 (2017) 116–126. doi:10.1016/j.molstruc.2017.04.080.

[101] U. Balijapalli, S. Manickam, M.D. Thiyagarajan, S.K. Iyer, Highly emissive, naked-eye solvatochromic probe based on styryl tetrahydrodibenzo [a,i] phenanthridine for acidochromic applications, RSC Adv. 6 (2016) 58549–58560. doi:10.1039/C6RA09359K.

[102] V.S. Pavlovich, Solvatochromism and Nonradiative Decay of Intramolecular Charge-Transfer Excited States: Bands-of- Energy Model , Thermodynamics , and Self-Organization, ChemPhysChem. 13 (2012) 4081–4093. doi:10.1002/cphc.201200426.

[103] S. Zeroual, J. Meinnel, A. Lapinski, S.F. Parker, A. Boudjada, A. Boucekkine, Vibrational spectroscopy and DFT calculations of 1,3-dibromo-2,4,6-trimethylbenzene: Anharmonicity, coupling and methyl group tunneling, Vib. Spectrosc. 67 (2013) 27–43. doi:10.1016/j.vibspec.2013.03.007.

[104] CambridgeSoft ChemBioDraw Ultra, (2013).

APPENDICES

Appendix A: University of Namibia Ethical Clearance Certificate

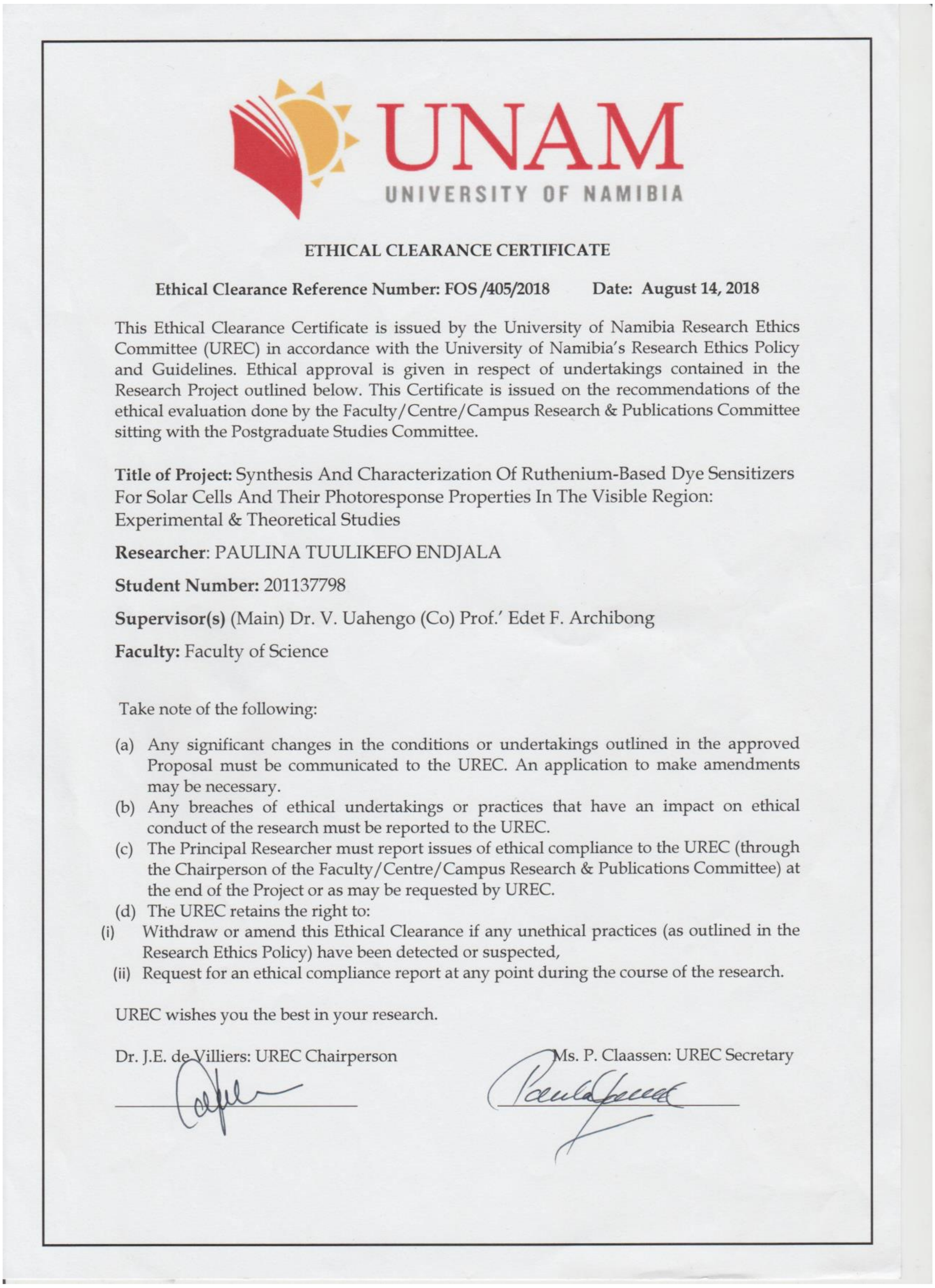

UNAM
UNIVERSITY OF NAMIBIA

ETHICAL CLEARANCE CERTIFICATE

Ethical Clearance Reference Number: FOS /405/2018 **Date: August 14, 2018**

This Ethical Clearance Certificate is issued by the University of Namibia Research Ethics Committee (UREC) in accordance with the University of Namibia's Research Ethics Policy and Guidelines. Ethical approval is given in respect of undertakings contained in the Research Project outlined below. This Certificate is issued on the recommendations of the ethical evaluation done by the Faculty/Centre/Campus Research & Publications Committee sitting with the Postgraduate Studies Committee.

Title of Project: Synthesis And Characterization Of Ruthenium-Based Dye Sensitizers For Solar Cells And Their Photoresponse Properties In The Visible Region: Experimental & Theoretical Studies

Researcher: PAULINA TUULIKEFO ENDJALA

Student Number: 201137798

Supervisor(s) (Main) Dr. V. Uahengo (Co) Prof.' Edet F. Archibong

Faculty: Faculty of Science

Take note of the following:

(a) Any significant changes in the conditions or undertakings outlined in the approved Proposal must be communicated to the UREC. An application to make amendments may be necessary.
(b) Any breaches of ethical undertakings or practices that have an impact on ethical conduct of the research must be reported to the UREC.
(c) The Principal Researcher must report issues of ethical compliance to the UREC (through the Chairperson of the Faculty/Centre/Campus Research & Publications Committee) at the end of the Project or as may be requested by UREC.
(d) The UREC retains the right to:
(i) Withdraw or amend this Ethical Clearance if any unethical practices (as outlined in the Research Ethics Policy) have been detected or suspected,
(ii) Request for an ethical compliance report at any point during the course of the research.

UREC wishes you the best in your research.

Dr. J.E. de Villiers: UREC Chairperson

Ms. P. Claassen: UREC Secretary

Appendix B: Supplementary information

Table S1. Systematic names of the designed ligands and their corresponding dye complexes obtained with ChemBioDraw [104].

Coded names	**Nomenclature of Ligands**
A1	2-(4-aminophenyl)-1H-benzo[de]isoquinoline-1,3(2H)-dione
S1	2-(2-((di(pyridin-2-yl)methylene)amino)ethyl)-1H-benzo[de]isoquinoline-1,3(2H)-dione
S2	2-(4-((di(pyridin-2-yl)methylene)amino)phenyl)-1H-benzo[de]isoquinoline-1,3(2H)-dione
S3	2-(4-((5H-cyclopenta[2,1-b:3,4-b']dipyridin-5-ylidene)amino)phenyl)-1H-benzo[de]isoquinoline-1,3(2H)-dione
S4	3-((4-((5H-cyclopenta[2,1-b:3,4-b']dipyridin-5-;9 ylidene)amino)phenyl)imino)indolin-2-one
	Nomenclature of the dye complexes
S1*	$[Ru(bpy)_2S1]^{2+}$
S2*	$[Ru(bpy)_2S2]^{2+}$
S3*	$[Ru(bpy)_2S3]^{2+}$
S4*	$[Ru(bpy)_2S4]^{2+}$

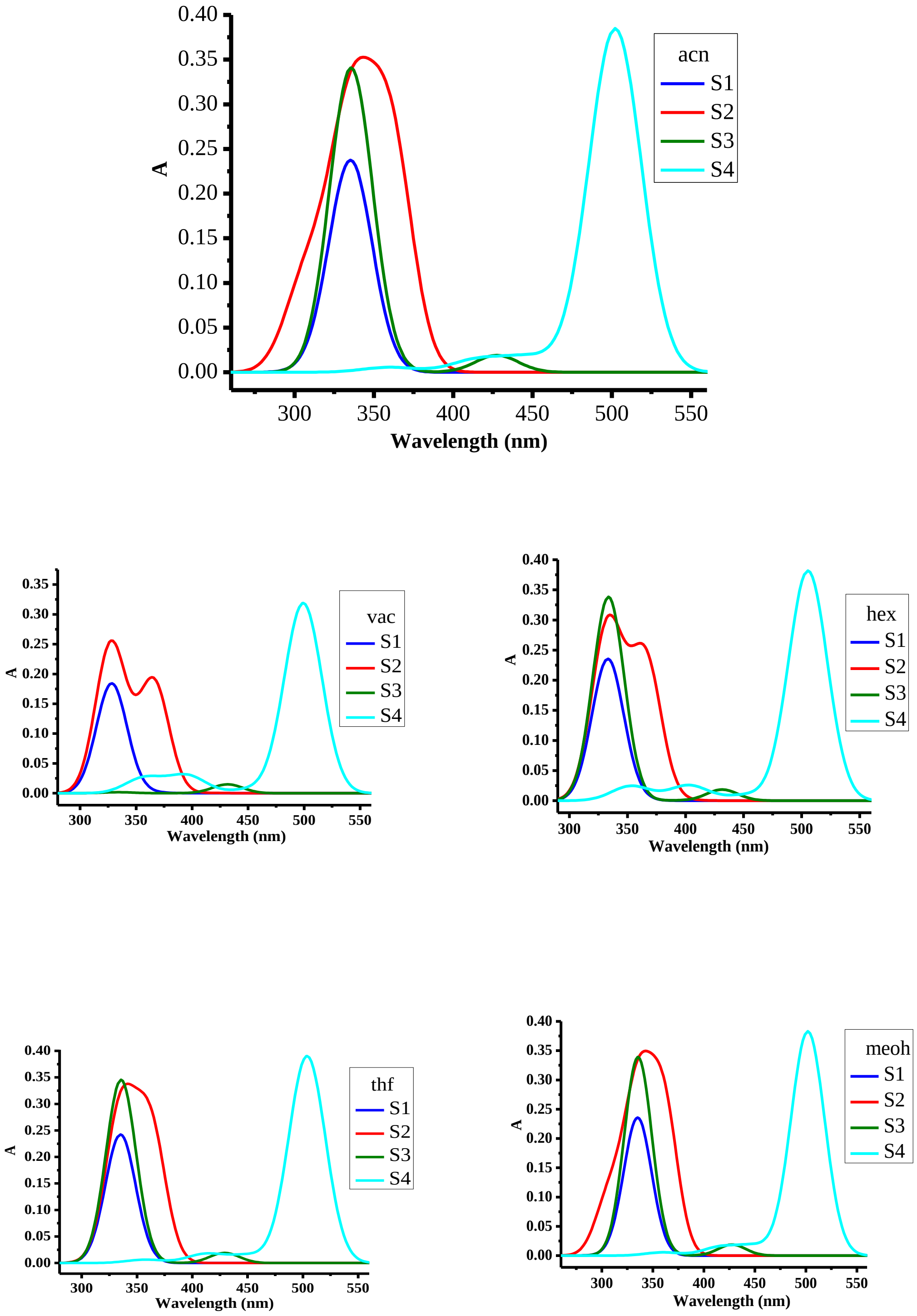

Figure S 1. Simulated UV-Vis spectra of the designed ligands in acetonitrile (acn), vacuum (vac), n-hexane (hex), tetrahydrofuran (thf) and methanol (meoh) computed at the B3LYP/6-31G(d,p) level.

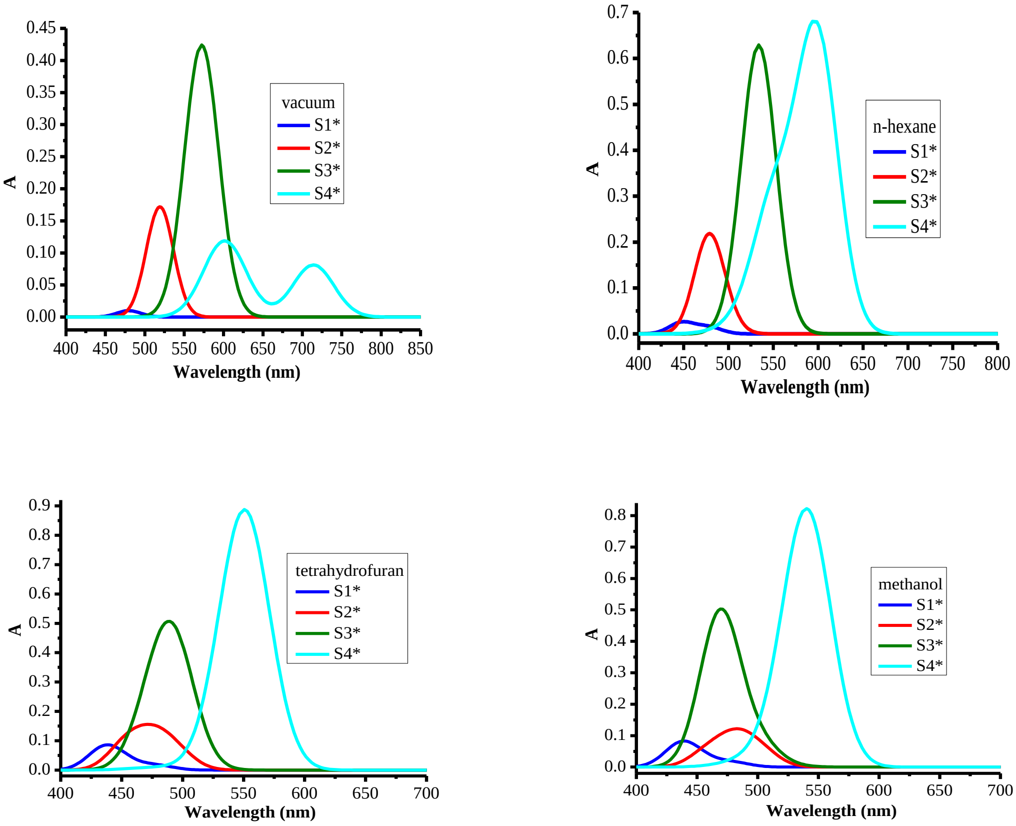

Figure S 2. Simulated UV-Vis spectra of the designed dye complexes in vacuum, n-hexane, tetrahydrofuran and methanol computed at the B3LYP/6-31G(d,p) level.

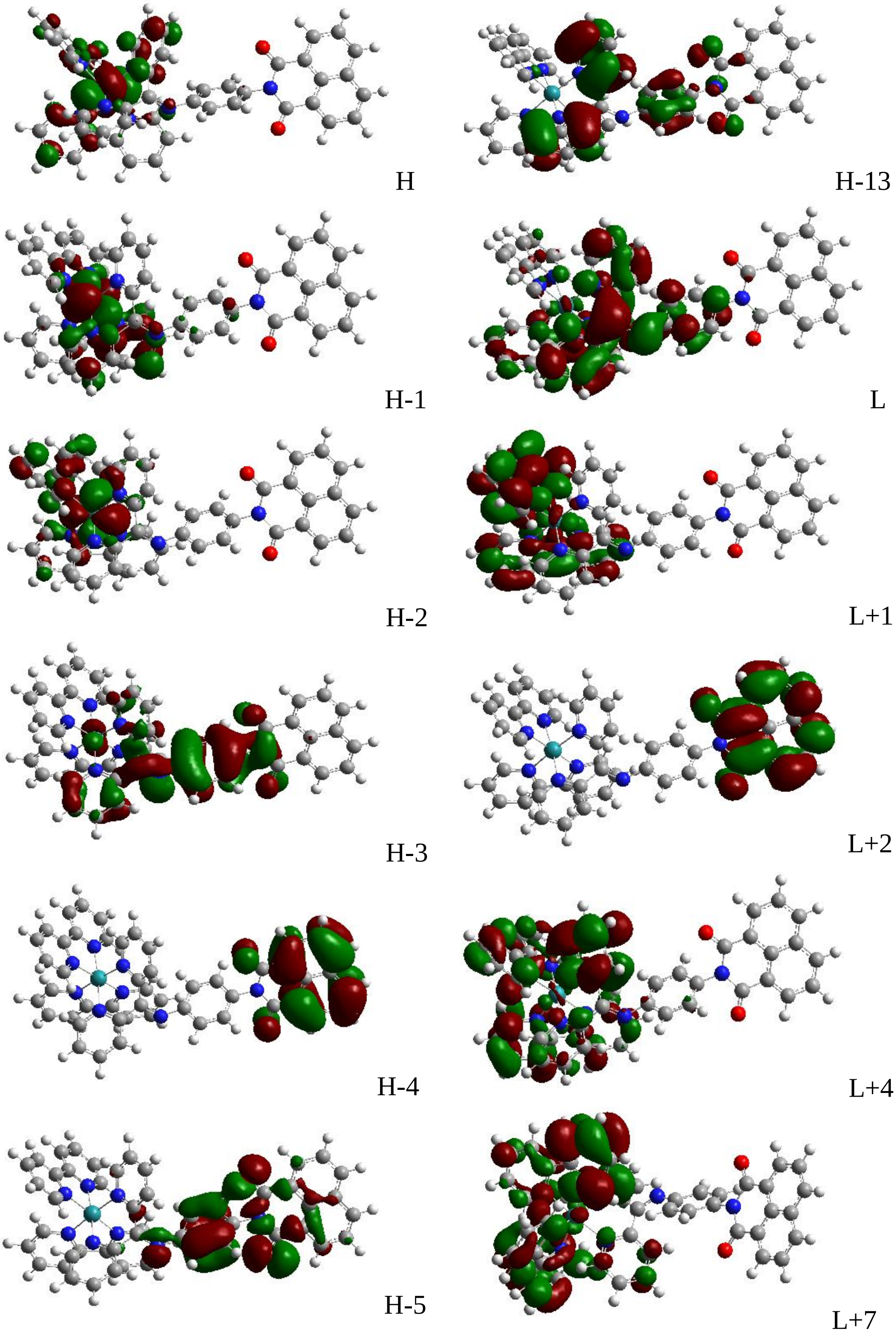

H

H-13

H-1

L

H-2

L+1

H-3

L+2

H-4

L+4

H-5

L+7

Figure S 3. Frontier molecular orbitals of S2* associated with the main transitions and associated spectral peaks in acetonitrile obtained at optimized geometries of S2* in acetonitrile via TDDFT B3LYP/3-21G(d) calculations.

Vacuum

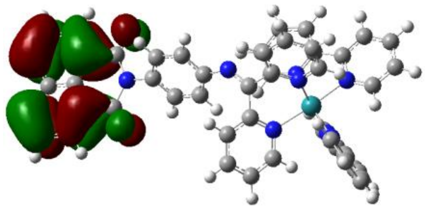
H

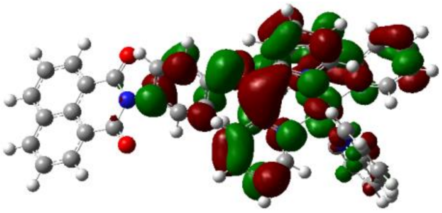
L+2

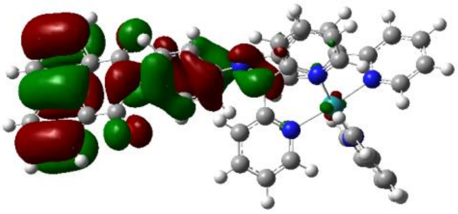
H-1

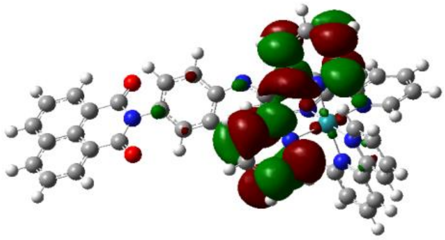
L+9

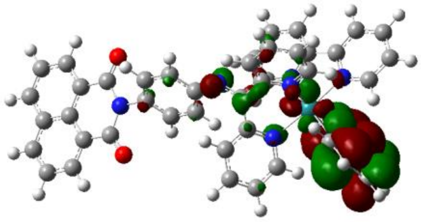
L

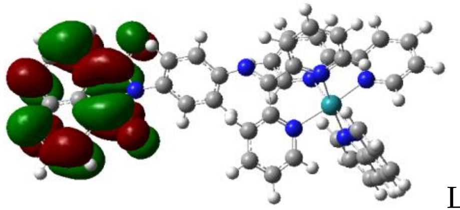
L+10

Hexane

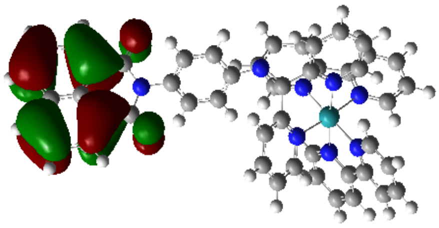
H

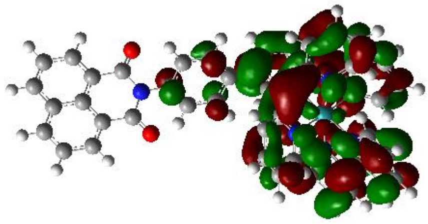
L

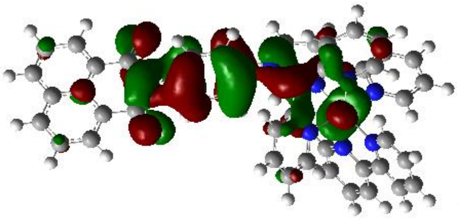
H-1

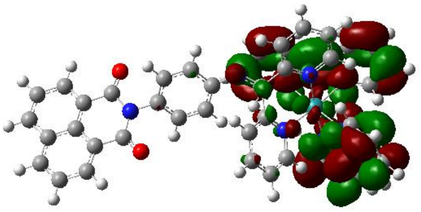
L+1

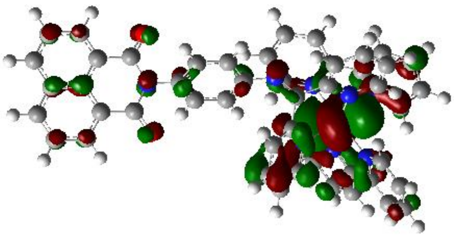
H-2

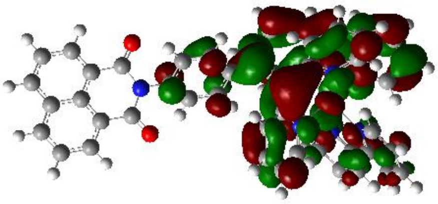
L+2

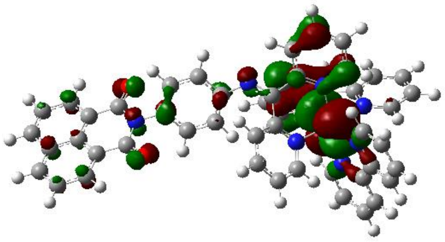

H-4

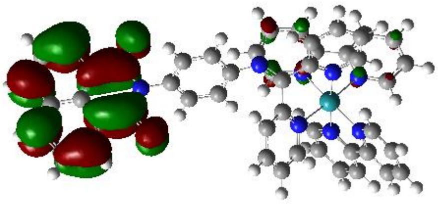

L+7

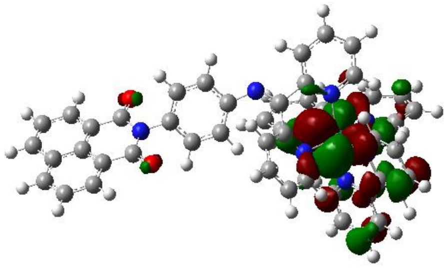

H-5

Tetrahydrofuran

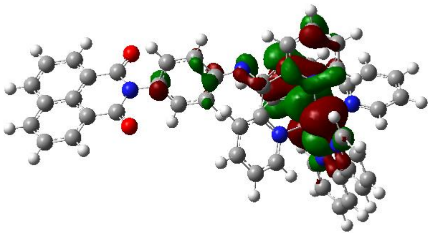

H-1

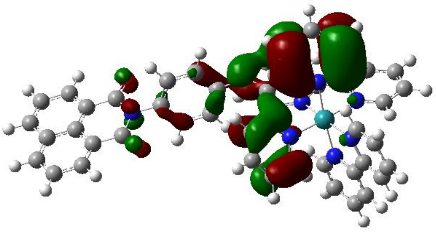

H-13

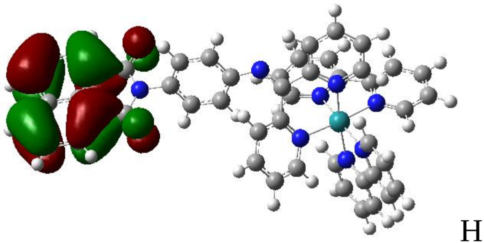

H-2

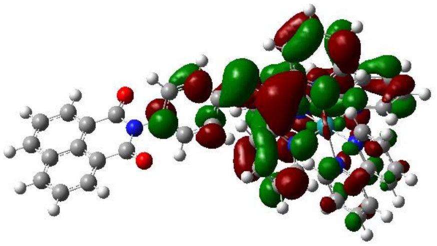

L

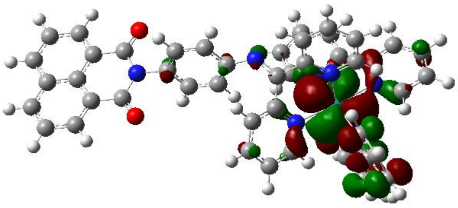

H-3

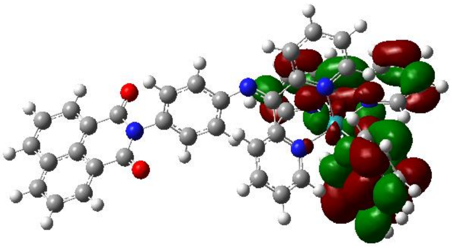

L+1

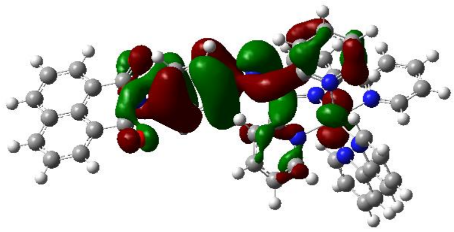

H-4

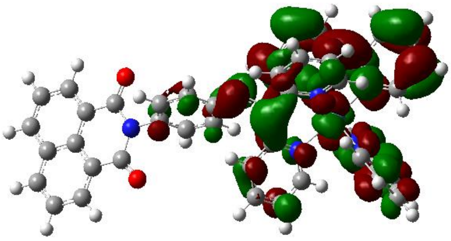

L+2

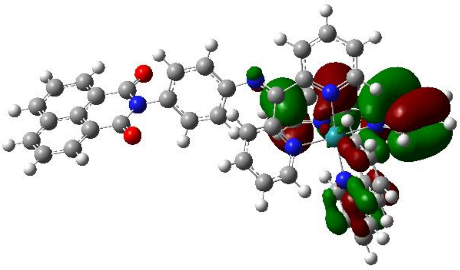

H-8

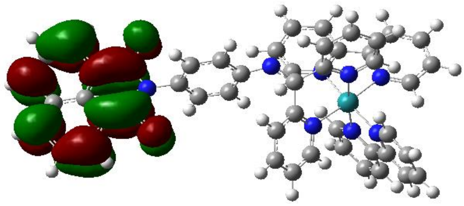

L+3

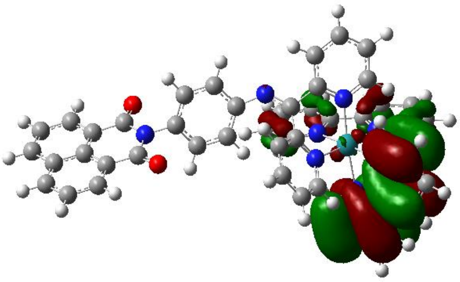

H-9

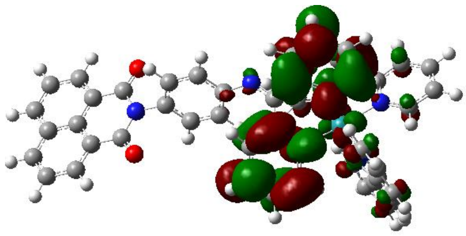

L+5

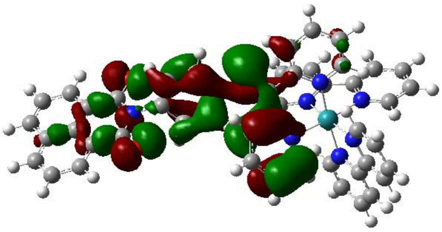

H-12

Methanol

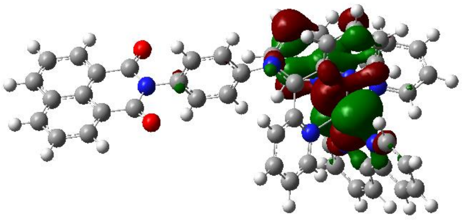

H-1

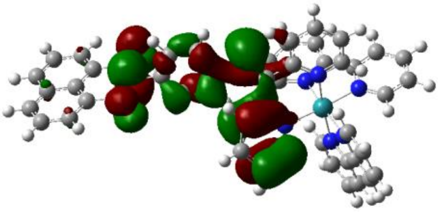

H-11

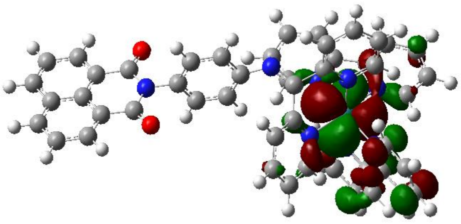

H-2

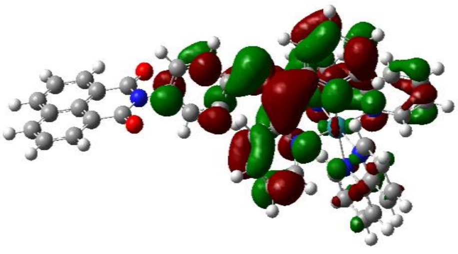

L

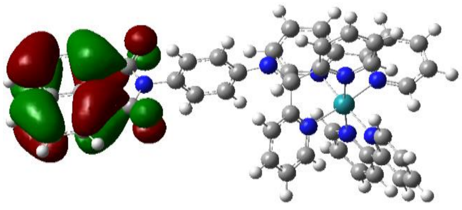

H-3

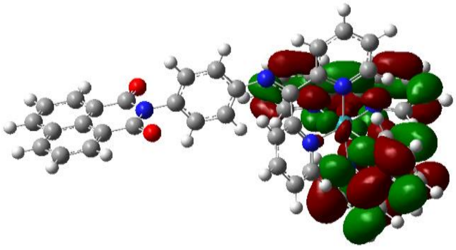

L+1

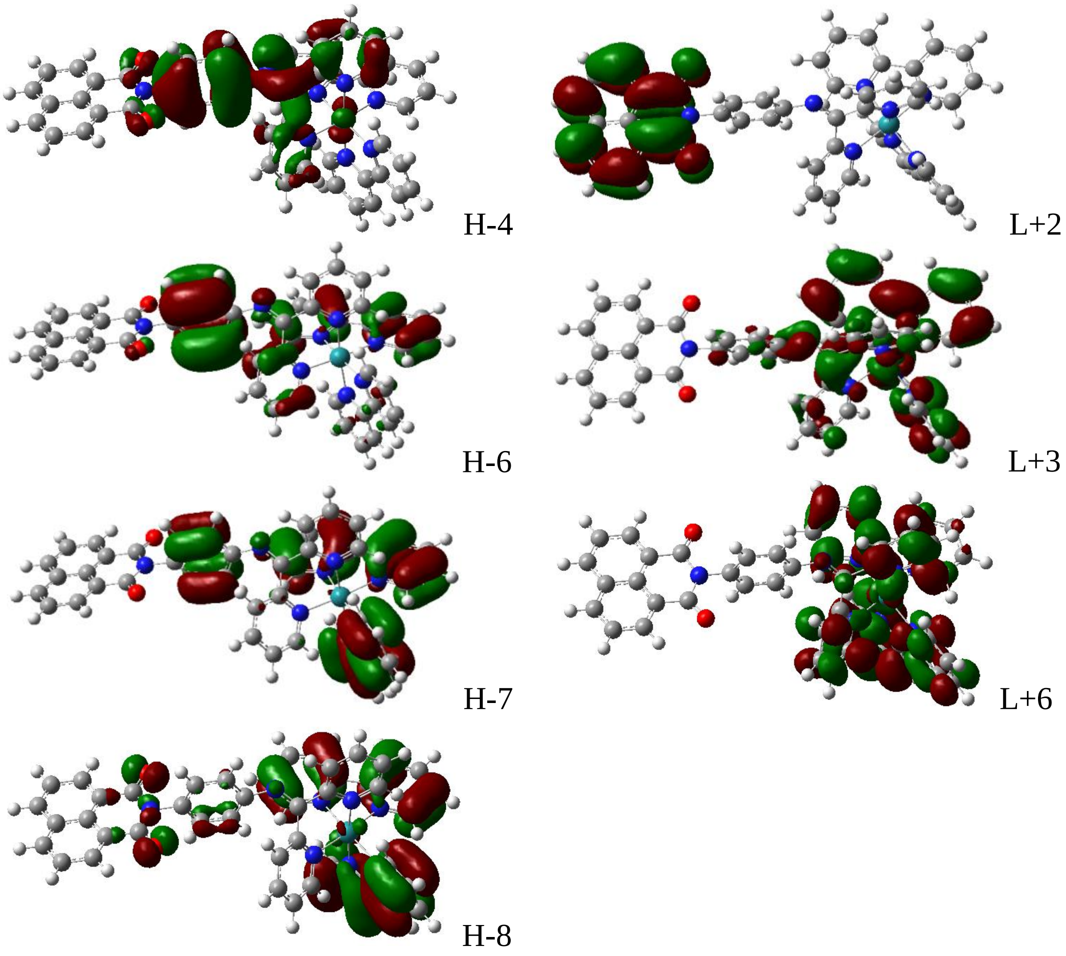

Figure S 4. Frontier molecular orbitals of S2* associated with the main transitions and excitation energies in vacuum, hexane, tetrahydrofuran and methanol obtained at optimized geometries of S2* in the respective solvents via TDDFT B3LYP/6-31G(d,p) calculations.

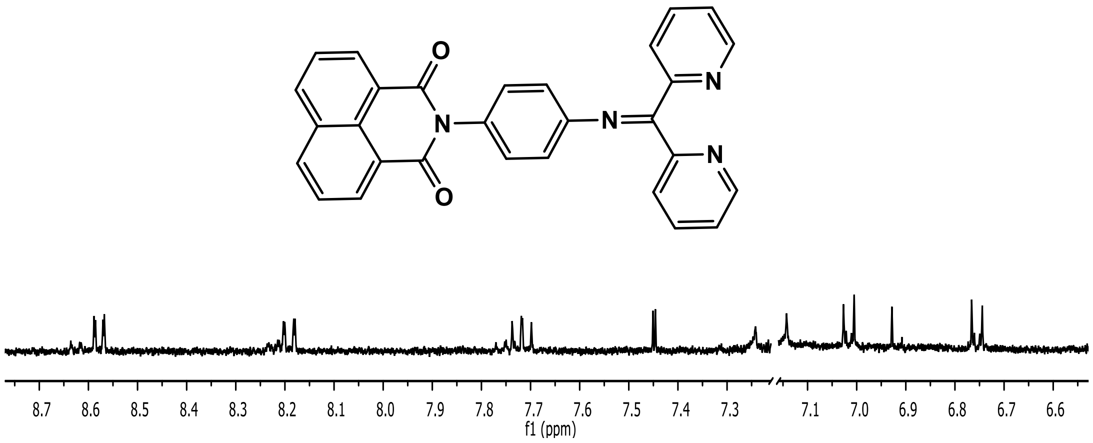

Figure S 5.¹H-NMR spectrum of S2 in $CDCl_3$.

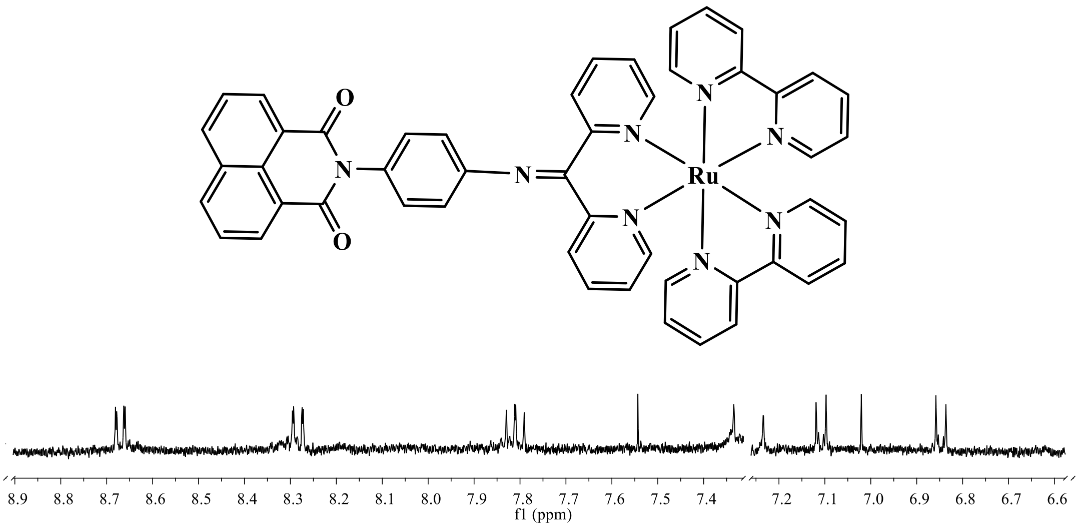

Figure S 6.¹H-NMR spectrum of S2* in $CDCl_3$.

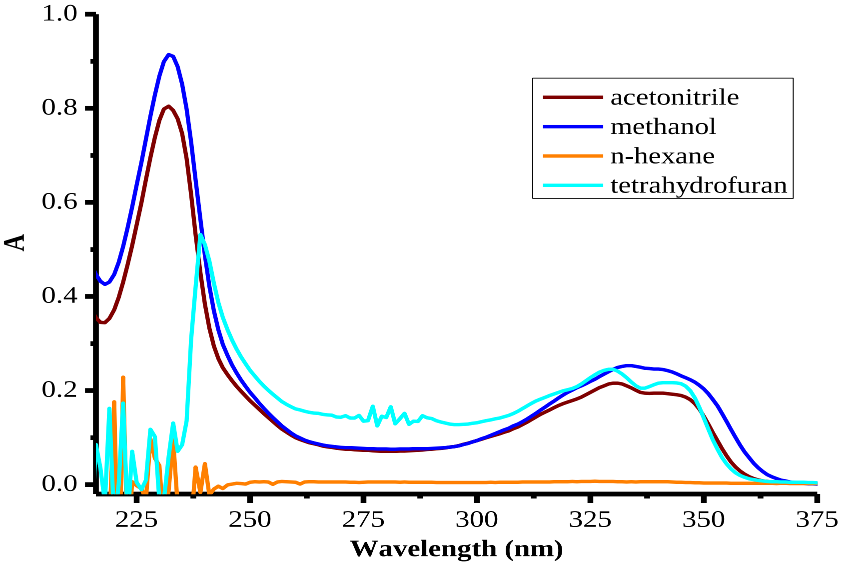

Figure S 7. UV-Vis spectra of S2 in various solvents.

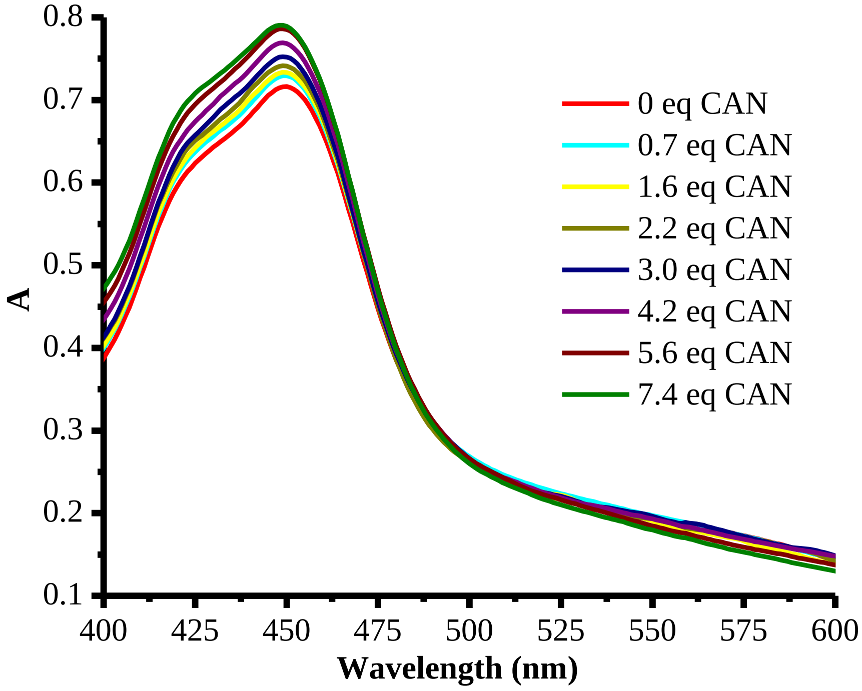

Figure S 8. UV-Vis titration spectra of S4* (methanol, 1x10^{-5} M) with ceric ammonium nitrate (3.0x10^{-2} M).

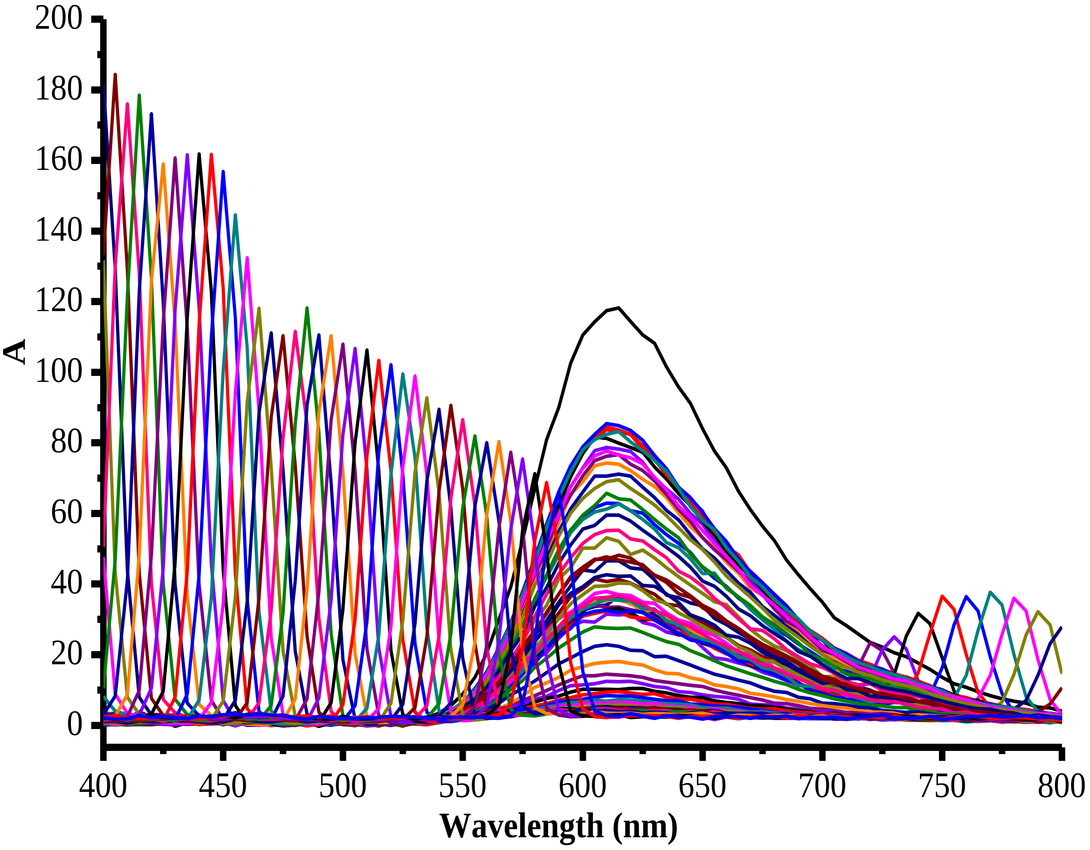

Figure S 9. The emission spectrum of S2* in acetonitrile (1.0 x 10^{-5} M) obtained at different excitation wavelengths ranging from 300 nm to 590 nm at an interval of 5 nm.